

**NOVEL BIOMEDICAL IMAGING SYSTEMS**

by

**YUAN LUO**

**A Dissertation Submitted to the Faculty of the**

**COLLEGE OF OPTICAL SCIENCES**

**In Partial Fulfillment of the Requirements**

**For the Degree of**

**DOCTOR OF PHILOSOPHY**

**In the Graduate College**

**THE UNIVERSITY OF ARIZONA**

**2 0 0 8**

THE UNIVERSITY OF ARIZONA  
GRADUATE COLLEGE

As members of the Dissertation Committee, we certify that we have read the dissertation prepared by Yuan Luo entitled "Novel Biomedical Imaging Systems" and recommend that it be accepted as fulfilling the dissertation requirement for the Degree of Doctor of Philosophy

\_\_\_\_\_ Date: July 18<sup>th</sup>, 2008  
Raymond K. Kostuk

\_\_\_\_\_ Date: July 18<sup>th</sup>, 2008  
Jennifer K. Barton

\_\_\_\_\_ Date: July 18<sup>th</sup>, 2008  
Arthur Gemitro

Final approval and acceptance of this dissertation is contingent upon the candidate's submission of the final copies of the dissertation to the Graduate College.

I hereby certify that I have read this dissertation prepared under my direction and recommend that it be accepted as fulfilling the dissertation requirement.

\_\_\_\_\_ Date: July 18<sup>th</sup>, 2008  
Dissertation Director: Raymond K. Kostuk

**STATEMENT BY AUTHOR**

This dissertation has been submitted in partial fulfillment of requirements for an advanced degree at The University of Arizona and is deposited in the University Library to be made available to borrowers under rules of the Library.

Brief quotations from this dissertation are allowable without special permission, provided that accurate acknowledgment of source is made. Requests for permission for extended quotation from or reproduction of this manuscript in whole or in part may be granted by the head of the major department or the Dean of the Graduate College when in his or her judgment the proposed use of the material is in the interests of scholarship. In all other instances, however, permission must be obtained from the author.

SIGNED: Yuan Luo

## ACKNOWLEDGEMENTS

I would like to thank my advisor, Dr. Raymond Kostuk, for his guidance and encouragement on my research projects. He has provided me in a positive and optimistic manner that helped me to find my own way in the process and carried me through challenges.

I would also like to thank Dr. Jennifer Barton. She was always willing to share her knowledge, help, and advice. I would like to express my gratitude to Dr. George Barbastathis for his kindness and sharing his invaluable time on my second project. Particular thank you goes to Dr. Arthur Gmitro for his effort of being my dissertation committee, Dr. Roy Frieden for his time to keep up a friendly relationship with me, and Ms. Gail Varin for her help on the required procedures of this dissertation.

I must acknowledge my project co-workers: Paul Gelsinger-Austin, Jonathan Watson, Lina Arauz, and Jose Castillo for their technical help, as well as moral support. I would like to extend my gratitude to the past and present members of the PSL, including Jesse Frantz, James Carriere, Miodrag Scepanovic, Wendi Maeda, Chia-Hung Chen, Juan Russo, Jennifer Harwell, Nasrin Ghanbari, Pyung-Suk Choi and Se-Hoon Lim. Additionally, I am greatly thankful to Jose Castro, Amit Ashok, Pawan Baheti, and June Ke of the ECE department and Ravi Pant, Amy Winkler, Garret Bonnema, and Tae-Young Choi of the Optical Sciences for their assistance on my projects.

Finally, I would like to deeply and sincerely thank my family members including my grandparents, my parents, and my wife for their love and support, and to whom I dedicate my work for this milestone.

## TABLE OF CONTENTS

<b>LIST OF ILLUSTRATIONS .....</b>	<b>8</b>
<b>LIST OF TABLES .....</b>	<b>14</b>
<b>ABSTRACT .....</b>	<b>15</b>
<b>Chapter 1. Introduction.....</b>	<b>17</b>
1.1. Background and Previous work .....	17
1.1.1. Optical Coherence Tomography .....	17
1.1.2. Volume Holographic Imaging System (VHIS).....	18
1.2. Goals and Contributions .....	20
1.3. Outline.....	23
<b>Chapter 2. Fiber Array for Parallel Optical Coherence Tomography .....</b>	<b>25</b>
2.1. Introduction.....	25
2.2. Fiber Array Model .....	27
2.3. Simulation Results .....	34
2.4. Fiber Fabrication Technique .....	41
2.4.1. Reduced Diameter Fiber .....	41
2.4.2. Single Mode Fiber Array .....	44
2.4.3. Fiber Cross-Talk Measurements .....	47
2.4.4. Coherent Depth Measurement with Reduced Fiber Diameter Array.....	52
<b>Chapter 3. Parallel Optical Coherence Tomography System.....</b>	<b>56</b>
3.1. Introduction.....	56
3.2. Fiber Array and Probe Assembly.....	56
3.2.1. Single Mode Fiber Array .....	56
3.2.2. Assembled Probe Tip.....	58
3.3. Fiber-Length Equalization .....	61
3.4. Image Acquisition .....	63
<b>Chapter 4. Volume Holographic Imaging System .....</b>	<b>70</b>
4.1. Introductions .....	70
4.2. Principle of Operation.....	70
4.3. Holographic Construction Setup.....	74
4.4. Reconstruction Setup & Image Acquisition .....	76
4.4.1. Non-fluorescence Images with a Red LED .....	83
4.4.2. Fluorescence Images with a Fluorescent Dye-- Acridine Orange .....	86
4.4.3. Imaging Experiment with 0.5% Intralipid Solution.....	91

<b>Chapter 5. Modeling for Curved Holographic Gratings .....</b>	<b>94</b>
5.1. Introduction.....	94
5.2. Rigorous Coupled Wave Analysis .....	95
5.3. Simulation Procedure for a Single Curved Grating .....	99
5.4. Simulation Procedure for Multiplexed Curved Grating.....	101
5.5. Experimental Measurements.....	103
5.5.1. Experimental Setup .....	103
5.5.2. Selectivity and Depth Separation Measurements .....	104
5.6. Simulation Results .....	109
<b>Chapter 6. PQ-doped PMMA for Holographic Recording .....</b>	<b>114</b>
6.1. Introduction.....	114
6.2. History.....	114
6.3. Fabrication Process .....	115
6.4. Grating Formation in PQ-doped PMMA .....	119
6.5. Optimization Method for a Single Grating .....	120
6.6. Optimization of Multiplexed Gratings.....	122
6.7. Dark Delay Time and Pre-illumination Exposure .....	123
<b>Chapter 7. Imaging Quality Improvements.....</b>	<b>130</b>
7.1. Background Subtraction.....	130
7.2. Non-overlapping Fluorescence Images with Larger Angular Separation.....	136
<b>Chapter 8. Conclusion .....</b>	<b>141</b>
8.1. POCT .....	141
8.2. VHIS .....	142
<b>APPENDIX A .....</b>	<b>146</b>
<b>APPENDIX B .....</b>	<b>164</b>
<b>APPENDIX C .....</b>	<b>166</b>
<b>REFERENCES.....</b>	<b>181</b>

## LIST OF ILLUSTRATIONS

Figure 1.1 Basic Optical Coherence tomography Schematic [1].....	17
Figure 1.2 Holographic imaging setup. L1 is the objective lens, and L2 is the collector lens. ....	19
Figure 2.1. Fiber array geometry used for analysis and the experimental design. $D_T$ reduced fiber diameter; $d_s$ fiber center separation; $d_{co}$ fiber core diameter; $D_o$ standard fiber diameter; $L$ interaction length of reduced diameter fiber.....	27
Figure 2.2. Description of a) parallel beam propagation in multiple fibers; b) light transmitted into a tissue sample and scattered; c) backscattered photons collected within the acceptance angle of the fiber; and d) return signals propagating in multiple fibers. ...	29
Figure 2.3. Rayleigh range from a fiber a) with (2LR) and b) without a lens (LR). $2w$ is the mode field diameter of the fiber.....	30
Figure 2.4. Coupling between fibers as a function of interaction length ( $L$ ). MMF A: $9.0\mu\text{m}$ core diameter, 0.55 numerical aperture (NA), $12\mu\text{m}$ fiber separation. SMF A: $8.2\mu\text{m}$ core diameter, 0.12 numerical aperture (NA), $15\mu\text{m}$ fiber separation. SMF B: $6.0\mu\text{m}$ core diameter, 0.16 numerical aperture (NA), $15\mu\text{m}$ fiber separation. MMF B: $8.0\mu\text{m}$ core diameter, 0.25 numerical aperture (NA), $12\mu\text{m}$ fiber separation. ....	36
Figure 2.5. Coupling (dB) as a function of fiber separation distance ( $\mu\text{m}$ ) for SMF A and SMF B fibers described in Figure 4 with fixed interaction lengths of 2 and 5 mm.....	38
Figure 2.6. Monte Carlo simulation of backscattered light from an Intralipid 10% tissue phantom solution as a function of distance from the launch fiber. $\circ$ $9.0\mu\text{m}$ core diameter, 0.55 numerical aperture (NA), $12\mu\text{m}$ fiber separation; $+$ $8.2\mu\text{m}$ core diameter, 0.12 numerical aperture (NA), $14\mu\text{m}$ fiber separation; $*$ $6.0\mu\text{m}$ core diameter, 0.16 numerical aperture (NA), $14\mu\text{m}$ fiber separation $\Delta$ $8.0\mu\text{m}$ core diameter, 0.25 numerical aperture (NA), $14\mu\text{m}$ fiber separation; $\times$ $8.2\mu\text{m}$ core diameter, 0.16 numerical aperture (NA), $14\mu\text{m}$ fiber separation. ....	39
Figure 2.7. Ratio of backscattered signal ( $P_o$ ) to backscattered cross-talk ( $P_x$ ) as a function of different fiber type (NA/dc). ....	41
Figure 2.8. Resulting fiber side view after etching process. The length of the $15\mu\text{m}$ diameter section is less than 3mm and the tapered section is $\sim 3\text{-}4\text{mm}$ [34].....	43

Figure 2.9. Picture of the etched fiber section next to a mask with 25 $\mu$ m squares [34]...	43
Figure 2.10. Array assembly procedure with V-groove [34].....	44
Figure 2.11. Schematic of linear fiber array with 15 channels and silicon trench groove.	46
Figure 2.12. (a) Schematic of linear fiber array with 8 channels and silicon trench. (b) Zoomed in on the fiber array. ....	47
Figure 2.13. Experimental system for measuring the backscattered signal to a fiber of interest and cross-talk to adjacent fibers in an array. The source is a super luminescent diode with a center wavelength of 1310 nm and Det 1, Det 2, and Det 3 are detectors...	49
Figure 2.14. Experimental data (circular dots) for crosstalk measure from an Intralipid 10% solution with a fiber array consisting of fibers with 8.2 $\mu$ m core diameters, 0.12 NA, and 15 $\mu$ m fiber separation. ....	50
Figure 2.15. Experimental coherent fiber system for measuring distances with the experimental fiber array. DAQ is a data acquisition card; M1 is the mirrored translated from the fiber array; L1 is a lens focusing light onto a moving mirror M2.....	52
Figure 2.16.(a) Interference fringes formed within the coherence length of the source with the mirror M1 located 50 $\mu$ m from the edge of the fiber array.....	54
Figure 2.17.(b) Interference fringes formed within the coherence length of the source with the mirror M1 located 150 $\mu$ m from the edge of the fiber array.....	54
Figure 2.18.(c) Interference fringes formed within the coherence length of the source with the mirror M1 located 250 $\mu$ m from the edge of the fiber array.....	55
Figure 3.1 Diagram of the assembled probe end of the POCT system.....	58
Figure 3.2. Diagram of the endoscopic assembled probe with a 0.2mm thick rigid stainless steel tube (a) lateral view (b) front view. ....	60
Figure 3.3. Schematic of the interferometer used to equalize fiber-lengths in the fiber array. Light from a SLD is split between the reference and sample fibers by passing it through a 3dB coupler. The probe end illuminates an IR mirror, and the reference end illuminates a glavo mirror. The return signal from a paired sample and reference arm is coupled into an output fiber that transfers the combined interference signal to an IR detector.....	61

- Figure 3.4. Parallel OCT system setup. Light from a SLD is coupled into a parallel fiber array through an array of 3-dB couplers mounted in a box. The probe end illuminates a target sample, and the reference end illuminates a glavo mirror. The return signal from a sample and reference arm pair is coupled into an output fiber that transfers the combined interference signal to an IR detector. .... 64
- Figure 3.5. The POCT image of the central portion of a contact lens. The resultant depth is  $\sim 300\mu\text{m}$  with  $120\mu\text{m}$  ( $8\times 15\mu\text{m}$ ) wide. .... 67
- Figure 3.6(a). Side view of a silicon ( $50\times 50\mu\text{m}$  inner square) depression with a depth of  $70\mu\text{m}$  was measured by a profilometer. (b) The POCT image of the depression showing a depth of  $75\mu\text{m}$ . The width of the inner layer is  $45\mu\text{m}$ . .... 68
- Figure 3.7. POCT image of tangerine flesh. The tangerine's juice vacuoles are clearly visible. .... 69
- Figure 4.1. (a) Bragg circle diagram for K-vector closure. (b) Geometry for analysis of a holographic grating. .... 73
- Figure 4.2. Construction setup of multiplexed gratings by using spherical and planar waves. M1 is the objective lens translated from a fixed objective lens M2. The angle of the reference beam is changed by  $\Delta\theta$  between each exposure to record a hologram. .... 74
- Figure 4.3. Construction setup for forming multiplexed gratings. Two relay systems (Objective Relay & Collector Relay) are used in the signal and reference arm to maintain constant irradiance at the hologram plane. .... 75
- Figure 4.4. Experimental imaging setup. L1 is the objective lens, and L2 is the collector lens. .... 77
- Figure 4.5. Experimental prototype of VHIS for reconstruction of multiplexed gratings using a red LED. .... 78
- Figure 4.6. Raw image taken using a hologram with two multiplexed gratings, and an Argon laser operated at a wavelength of  $488\text{nm}$ . .... 79
- Figure 4.7. Raw image of an Air Force Resolution Bar Chart taken using a red LED, a Lumenera 6 Mpixel camera and  $2.8\times$  magnification with a single grating. Lateral features as small as  $4.5\mu\text{m}$  are well resolved. .... 82
- Figure 4.8. Raw images of an Air Force Resolution Bar Chart using a red LED, an Andor iXon camera and  $5.6\times$  system magnification. Lateral features as small as  $7.8\mu\text{m}$  are well resolved. .... 83

- Figure 4.9. Onion skin images reconstructed by VHIS using a red LED, an Andor iXon camera and 5.6× magnification. Both images (a) and (b) show two simultaneous sections obtained at two depths within an onion skin and the depth separation between images is 75μm. .... 85
- Figure 4.10. Human ovary images reconstructed by VHIS using a red LED, a Lumenera 6 Mpixel camera and 2.8× magnification. Both images (a) and (b) show two simultaneous sections of human ovary obtained at two depths with the depth separation between images of 75 μm. .... 86
- Figure 4.11. Experimental prototype for reconstruction using a tripled Nd:YAG laser as an excitation source..... 88
- Figure 4.12. Fluorescence images of mouse fat stained with Acridine Orange. The figure was obtained with the VHIS system using a Nd:YAG excitation source, 5.6× magnification, an Andor iXon camera and a two grating hologram with an 1o angle between the reference beams. .... 89
- Figure 4.13. Fluorescence images of mouse ovary stained with Acridine Orange. The figure was obtained with the VHIS system using a Nd:YAG excitation source, 5.6× magnification, an Andor iXon camera and a two grating hologram with an 1o angle between the reference beams. .... 90
- Figure 4.14. Fluorescence images of mouse colon stained with Acridine Orange. The figure was obtained with the VHIS system using a Nd:YAG excitation source, 5.6× magnification, an Andor iXon camera and a two grating hologram with an 1o angle between the reference beams. .... 91
- Figure 4.15. Images of the Air Force Resolution Bar Chart taken with the VHIS system using a red LED ( $\lambda_{\text{central}}=633\text{nm}$ ,  $\Delta\lambda\sim 30\text{nm}$ ), 5.6× magnification, and an Andor iXon camera. Figure (a) shows the Bar Chart image of Group 6 at a depth of 300μm in a 0.5% Intralipid solution. The figure on the right shows the Bar Chart image of Group 6 at a depth of 600μm in the 0.5% solution..... 93
- Figure 5.1. Reconstruction geometry of a single slanted planar grating with a planar wave of propagation vector  $\vec{k}_1$  incident with an arbitrary angle and polarization. .... 96
- Figure 5.2. Construction and reconstruction stages of a curved grating..... 100
- Figure 5.3. Setup of multiplexed curved gratings..... 102
- Figure 5.4. Construction setup of the angle multiplexed holographic filters..... 104

Figure 5.5. Experimental setup for depth separation, diffraction efficiency, and selectivity measurements.....	105
Figure 5.6.(a) Experimental results of the depth selectivity for the hologram of two gratings at 488nm. (b)Experimental results of the depth selectivity for the hologram of two gratings at 633nm.....	107
Figure 5.7. Experimental results of the relationship between $\Delta Z_{con}$ and $\Delta Z_{recon}$ (a) at the same wavelength of 488nm for both construction and reconstruction. (b) at the wavelength of 488nm for construction and 633nm for reconstruction.....	108
Figure 5.8.(a) Numerical and experimental results of the depth selectivity for the hologram of two gratings at 488nm. (b) Numerical and experimental results of the depth selectivity for the hologram of two gratings at 633nm.....	112
Figure 5.9. Experimental results and numerical analysis for the relationship between $\Delta Z_{con}$ and $\Delta Z_{recon}$ (a) at the same wavelength of 488nm for both construction and reconstruction. (b) at the wavelength of 488nm for construction and 633nm for reconstruction.....	113
Figure 6.1. Mold for the sample mixture preparation.....	116
Figure 6.2. Fabrication process and holographic recording flow diagram. ....	118
Figure 6.3. Holographic recording setup. ....	121
Figure 6.4. Construction setup of the multiplexed holographic gratings.....	123
Figure 6.5. Measured multiplexed grating diffraction efficiency with different dark delay times between exposures.....	125
Figure 6.6. Measured multiplexed grating diffraction efficiency of five multiplexed gratings with $t_{dd}=10\text{sec}$ and a pre-illumination of $360\text{mJ/cm}^2$ . ....	129
Figure 7.1. Image enhancement with background subtraction applied simultaneously to five images from different depths within an onion peel sample. Left image is the structure of interest plus the background. Right image is the structure of interest after the background is subtracted.....	132
Figure 7.2. Fluorescence imaging with the volume holographic imaging system of mouse fat. (a) Image of mouse fat with background noise. (b) Filtered image with background subtraction applied simultaneously to the two sections in (a). ....	133

- Figure 7.3. Fluorescence imaging with the volume holographic imaging system of mouse colon (a) Image of mouse colon with background noise and (b) Filtered image with background subtraction applied simultaneously to the two sections in (a). ..... 134
- Figure 7.4. A single column of (a) in-focused, (b) out-of-focused, (c) filtered images obtained for the use of contrast and SNR measurements. .... 135
- Figure 7.5. Reconstruction setup for non-overlapping images on CCD plane. .... 136
- Figure 7.6. Fluorescence images of mouse fat stained with Acridine Orange. The figure was obtained with the VHIS system using a two grating hologram with an  $8^\circ$  angle between the reference beams. Two simultaneous depth-resolved images are projected and the depth separation is  $\sim 65\mu\text{m}$ . .... 138
- Figure 7.7. Image enhancement with background subtraction applied simultaneously to two depth-resolved images in Figure 7.6. .... 139
- Figure 7.8. Fluorescence images of mouse colon stained with Acridine Orange, obtained with the VHIS system. Image enhancement with background subtraction has been applied. Colonic crypts ( $\sim 20\mu\text{m}$  cross-section) can be visualized. .... 140

## LIST OF TABLES

Table 1.1 POCT Prototype System.....	21
Table 1.2 VHIS Prototype System.....	23
Table 2.1. Fiber parameters used in the array and fraction of collected backscatter $P_o$ ...	34
Table 3.1. Channel transmission efficiency .....	57
Table 4.1. CCD Specifications.....	81
Table 5.1. Max. $\eta$ and angular selectivity ( $\Delta\theta_s$ ) of a hologram with two multiplexed gratings.....	106
Table 5.2. Max. $\eta$ and angular selectivity ( $\Delta\theta_s$ ) of a hologram with two multiplexed gratings.....	111
Table 6.1. Single gratings with constant exposure of $610\text{mJ}/\text{cm}^2$ .....	126
Table 6.2. Two multiplexed gratings with constant exposure of $610\text{mJ}/\text{cm}^2$ .....	127
Table 6.3. Five multiplexed gratings with $t_{dd}=10\text{sec}$ and a pre-illumination of $360\text{mJ}/\text{cm}^2$ .....	128

## ABSTRACT

The overall purpose of the dissertation is to design and develop novel optical imaging systems that require minimal or no mechanical scanning to reduce the acquisition time for extracting image data from biological tissue samples. Two imaging modalities have been focused upon: a parallel optical coherence tomography (POCT) system and a volume holographic imaging system (VHIS).

Optical coherence tomography (OCT) is a coherent imaging technique, which shows great promise in biomedical applications. A POCT system is a novel technology that replaces mechanically transverse scanning in the lateral direction with electronic scanning. This will reduce the time required to acquire image data. In this system an array with multiple reduced diameter (15 $\mu$ m) single mode fibers (SMFs) is required to obtain an image in the transverse direction. Each fiber in the array is configured in an interferometer and is used to image one pixel in the transverse direction.

A VHIS is based on volume holographic gratings acting as Bragg filters in conjunction with conventional optical imaging components to form a spatial-spectral imaging system. The high angular selectivity of the VHIS can be used to obtain two-dimensional image information from objects without the need for mechanical scanning. In addition, the high wavelength selectivity of the VHIS can provide spectral information of a specific area of the object that is being observed. Multiple sections of the object are projected using multiplexed holographic gratings in the same volume of the

Phenanthrenequinone- (PQ-) doped Poly (methyl methacrylate) (PMMA) recording material.

## Chapter 1. Introduction

### 1.1. Background and Previous work

#### 1.1.1. Optical Coherence Tomography

Optical coherence tomography (OCT) and holographic imaging tools have been used in biomedical applications. These systems possess high resolution, can image subsurface tissue structures, and have non- or minimally-invasive properties. OCT is suitable for viewing the internal structure of biological tissue by measuring reflected optical signals [1]. The system uses light from a broad spectral band light emitting diode (LED) to enhance the reflected signal from a tissue sample. Light from this short coherence length source is strong enough to provide useful signals from several millimeters below a tissue surface.

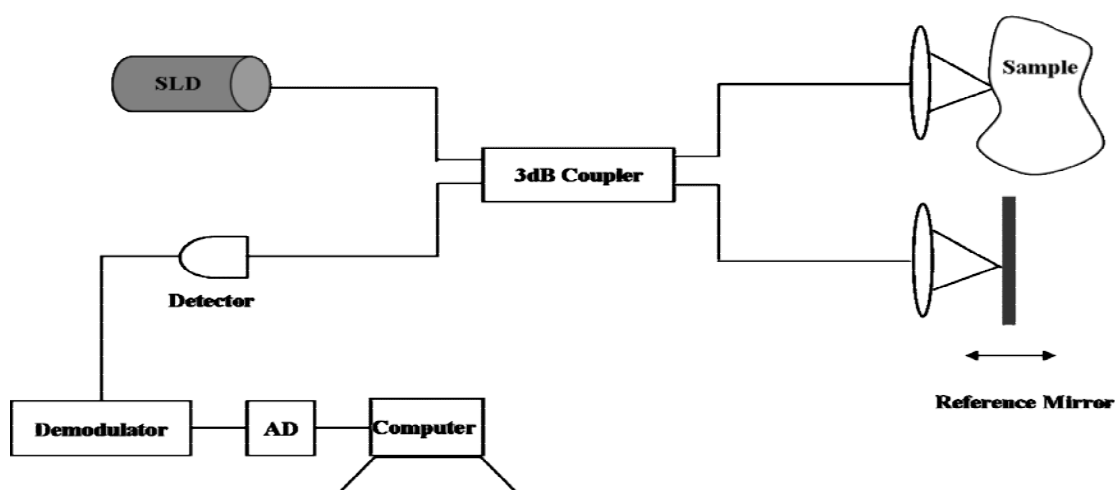


Figure 1.1 Basic Optical Coherence tomography Schematic [1].

Many existing OCT systems use fiber-optic interferometers. These systems currently collect object information through one single mode fiber. Mechanical scanning in the lateral direction increases the time to acquire an image and may limit clinical applications. Steps have been made toward developing a parallel OCT system that reduces the acquisition time by eliminating mechanical scanning in the lateral direction. Full field OCT systems can rapidly acquire images but are not appropriate for endoscopic use [2]. Fiber image guides with fibers that support a few modes have been used in special purpose OCT systems [3]. However, their performance degrades when the fibers are bent, which can limit their use in endoscopic applications.

### **1.1.2. Volume Holographic Imaging System (VHIS)**

Holography has been used for displays and optical elements. It is a wavefront recording technique, interfering two coherent optical fields and then exposing a photosensitive material with this pattern to form a hologram. The wavefronts can be planar, spherical, or any other form that is suitable for different applications. The recording material can be a photopolymer, film, crystal, or high-resolution digital camera.

A variety of optical holographic methods such as spectral decomposition holography have been considered for medical imaging applications [4]-[10]. The drawback of these approaches is that they require scanning and considerable time for reconstructing the image. For example, in spectral decomposition holography, a laser pulse is used to simultaneously form a number of single frequency holograms each spaced  $\Delta\lambda$  in wavelength and separately stored in a computer memory [10]. After recording, a

computer program, using each monochromatic hologram, synthesizes them into an image at a desired depth by recombining those reconstructions with appropriate phase delays between them. This imaging system can see highly scattering objects using a broadband tunable dye laser and a CCD camera located in the image plane. However, this technique requires the recording of an interference pattern on a digital camera and the computational time required to reconstruct an image. These factors reduce the spatial resolution and increase the time required to generate an image.

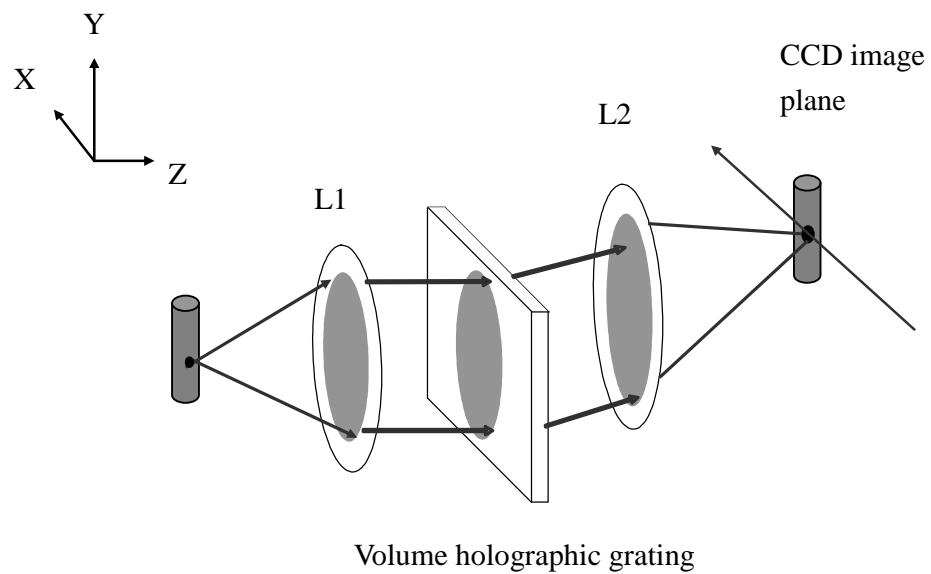


Figure 1.2 Holographic imaging setup. L1 is the objective lens, and L2 is the collector lens.

A different imaging system, using volume holographic filters, was first described by Barbastathis et al in 1999 and shown in Figure 1.2. In that paper, it was observed that a simple volume hologram formed by two plane waves could act as a depth-selective element with background rejection properties. In this system the volume hologram may be thought of as a component similar to a pinhole in a confocal microscope. In this sense, images of many sections may be acquired simultaneously through the use of many gratings superimposed in the recording material [11].

## **1.2. Goals and Contributions**

The main goals of this dissertation are to design and develop two novel imaging systems: POCT and VHIS. In the POCT project, the system incorporates a SMF array with 15 $\mu$ m reduced diameter fibers into a parallel interferometer to obtain images at a faster rate than mechanically scanned OCT systems. Electronic scanning eliminates the need for mechanical scanning in the lateral direction. In the dissertation, a prototype POCT with an 8-channel linear optical fiber array is described. The performance of the 8-channel POCT system is outlined in the following Table. Novel contributions in this research include:

- (1) Optimization of the design and development of a linear SMF array with 15 $\mu$ m reduced diameter fibers in the POCT prototype system.
- (2) Evaluation of the fiber array for potential use in a coherent distance measuring demonstration system without a lens system.

(3) Implementation of a Monte Carlo simulator for a variety of linear fiber arrays to simulate backscattered light from an Intralipid-10% tissue phantom solution.

(4) Successful development, fabrication and operation of the POCT system for obtaining images of both scattering and highly reflective samples.

Table 1.1 POCT Prototype System

Number of Channels	8
Operating Wavelength	1310nm
System Axial Resolution	20 $\mu$ m
System Transverse Resolution	15 $\mu$ m
System Dynamic Range	66dB
Endoscopic Assembled Probe Tip	1.8mm inner/2.0 outer diameter

In the VHIS project, the overall goal is to develop, fabricate, and test a novel optical imaging system that requires no mechanical scanning and can rapidly extract simultaneous spatial-spectral information from biological tissue samples. The VHIS project extends on Liu's system [11] in order to increase the averaged diffraction efficiency of multiplexed gratings and obtain more lateral and depth information from highly scattering objects.

VHIS is based on volume holographic Bragg filters used in conjunction with conventional optical imaging components to form the imaging system. The high angular selectivity of the VHIS can be used to obtain two-dimensional image information from objects without the need for mechanical scanning. The holographic material used can provide high efficiencies, large apertures, and is formed in a low cost polymer material.

In addition, laser induced fluorescence (LIF) has been developed and shows great promise for a variety of clinical applications. With a highly sensitive camera, VHIS is capable of simultaneously obtaining spatial-spectral information of fluoresced tissue samples without scanning. The performance of the VHIS system is outlined in the following Table. Novel contributions in this research include:

- (1) Optimization of development and fabrication of multiplexed holographic gratings in PQ-PMMA for spectral-spatial imaging filters.
- (2) Development and implementation of numerical analytical tools based on rigorous coupled wave theory for spherical wave gratings multiplexed in volume holographic recording materials.
- (3) Successful development, fabrication and operation of the VHIS prototype system for obtaining images of biological samples.
- (4) Evaluation of the multiplexed gratings and VHIS for potential use in LIF imaging of sub-surface tissue structures.

Table 1.2 VHIS Prototype System

Number of Optical Sections	2 ~ 5
Diffraction Efficiency (for 2 Multiplexed gratings)	60% (Max.) & 40% (Min)
Spectral Range	580-680nm
Spectral Resolution	5nm
Spatial Resolution (X, Y, Z)	4 $\mu$ m (X-Y) & 15 $\mu$ m (Z)
Depth of Imaging (2% Intralipid)	200 $\mu$ m
Field of View	1.46 $\times$ 1.46mm

### 1.3. Outline

In Chapter 2, a Monte Carlo simulator and a description of the approach to the design and fabrication of the linear fiber array are performed. In Chapter 3, the design of an endoscopic probe tip for the use of POCT is described. The performance of this system is also discussed in Chapter 3. In Chapter 4, the operation of multiplexed gratings is explained as used of spatial-spectral filters in the VHIS. Theoretical results based on rigorous coupled wave theory and the analyses of experimental performance are compared in Chapter 5. In Chapter 6, the design and experimental procedure of the optimized multiplexed holographic filters formed in PQ-PMMA to enhance the

performance of VHIS are evaluated. Techniques to improve image quality are presented in Chapter 7. In the conclusion, the overall results are given and ideas for future applications of POCT and VHIS are suggested.

## **Chapter 2. Fiber Array for Parallel Optical Coherence Tomography**

### **2.1. Introduction**

Optical fibers have proven to be very useful for minimally invasive optical diagnostic applications in medicine such as fluorescence [12], Raman scattering [13], two-photon microscopy [14], laser Doppler flowmetry [15], and optical coherence tomography [16]-[19]. In many cases fiber arrays can increase the acquisition rate of collected information and make the technique more suitable for clinical applications.

When used for clinical applications it is desirable to be able to bend and twist the fiber or fiber array to allow it to be positioned in various parts of the body. In some applications such as coherent imaging, higher contrast signals are obtained using single mode fibers (SMFs) that do not transfer power between different fiber modes. Single mode fiber arrays are not readily available at longer wavelengths that have a greater penetration depth in highly scattering tissue samples. Therefore it may be necessary to custom fabricate arrays of single mode fibers that operate at near infrared wavelengths (1300-1500 nm).

Many fiber and fiber array systems of interest in medical applications require transmitting light to the sample and then collecting it. A variety of transmission and collection geometries for these configurations have been documented [13][16] [19][20], however the fibers used in these studies typically had large diameters (200-600  $\mu\text{m}$ ) with separate transmit and receive fibers. In imaging applications it is often useful to have

fiber arrays with much smaller center spacing. These requirements have been met in part in recent experiments by mechanically scanning a single beam across the end face of a multimode fiber image guide with 12 mm fiber center spacing [21][22]. In another experiment a two-photon laser scanning fluorescence microscope was successfully demonstrated using a fiber image guide that is single mode at 440 nm with 2.4 mm diameter core fibers separated by 4.0 mm [14]. However, to author's knowledge, single mode propagation in flexible high-density fiber arrays at near infrared wavelengths has not been previously demonstrated.

This Chapter examines the performance of fiber arrays consisting of small diameter ( $<15\ \mu\text{m}$ ) single mode fibers operating in the 1300 nm wavelength range. Single mode fibers can be bent in small radii ( $\sim 1\ \text{cm}$ ) and twisted without transferring power between modes as occurs in multi-mode fibers. This makes them desirable for flexible endoscope applications that require a single mode beam such as in coherent detection processes. Operation at 1300 nm allows greater optical beam penetration into biological tissue samples than can be obtained at shorter wavelengths. The motivation for this paper is to establish practical design limits for arrays with single mode, 1300nm fibers for potential use in coherent optical systems that simultaneously transmit and receive optical signals through each fiber. Coupling between fibers is modeled using beam propagation methods and backscattered light is determined using the Monte Carlo method. An experimental array is fabricated by controlled etching of standard single mode fibers using a buffered oxide etch. The experimental fiber array was used to measure backscattered signals from a tissue phantom consisting of an Intralipid solution and used to verify the simulation

techniques. The experimental fiber array was also used in a coherent detection system to measure the distance of a mirror from the end of the array.

## 2.2. Fiber Array Model

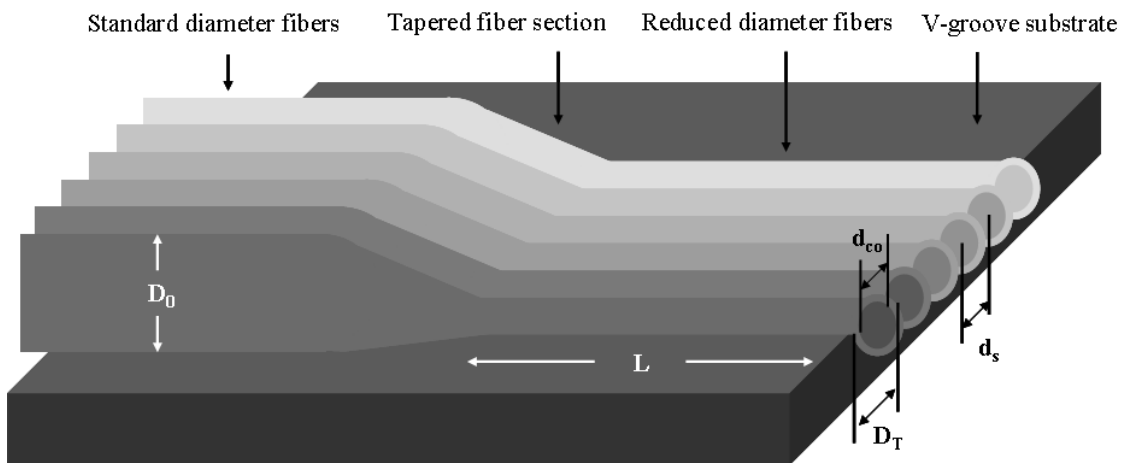


Figure 2.1. Fiber array geometry used for analysis and the experimental design.  $D_T$  reduced fiber diameter;  $d_s$  fiber center separation;  $d_{co}$  fiber core diameter;  $D_0$  standard fiber diameter;  $L$  interaction length of reduced diameter fiber.

Figure 2.1 shows the general configuration for the fiber arrays analyzed in this paper. At the probe tip end of the array the fibers have a reduced diameter of  $d_s$ . This diameter exists for a length of  $L$  and then increases to a larger diameter  $D_0$ . The tapered fiber sections are mounted on a substrate that has a refractive index  $n_b$  and are surrounded by optical cement with refractive index  $n_g$ . The larger diameter fiber section is bundled to

form the cable end of an endoscope that will be connected to an optical source and detection optics. The coupling analysis also considers the effects of the optical cement and the substrate.

Our modeling sequence consists of computing: 1) the power coupled from a fiber of interest into adjacent fibers in the array and vice versa (Figure 2.2a); 2) the power transmitted into the tissue by the fiber of interest or reflected from the fiber-tissue interface (Figure 2.2b); 3) the backscattered light coupled into the fiber of interest (i.e. the signal, Figure 2.2c); 4) the backscattered light coupled into the fiber of interest that originated from adjacent fibers in the fiber array causing photon noise (i.e. cross-talk, Figure 2.2c); and 5) the returning signal light lost by coupling from the fiber of interest into adjacent fibers and vice versa (Figure 2.2d).

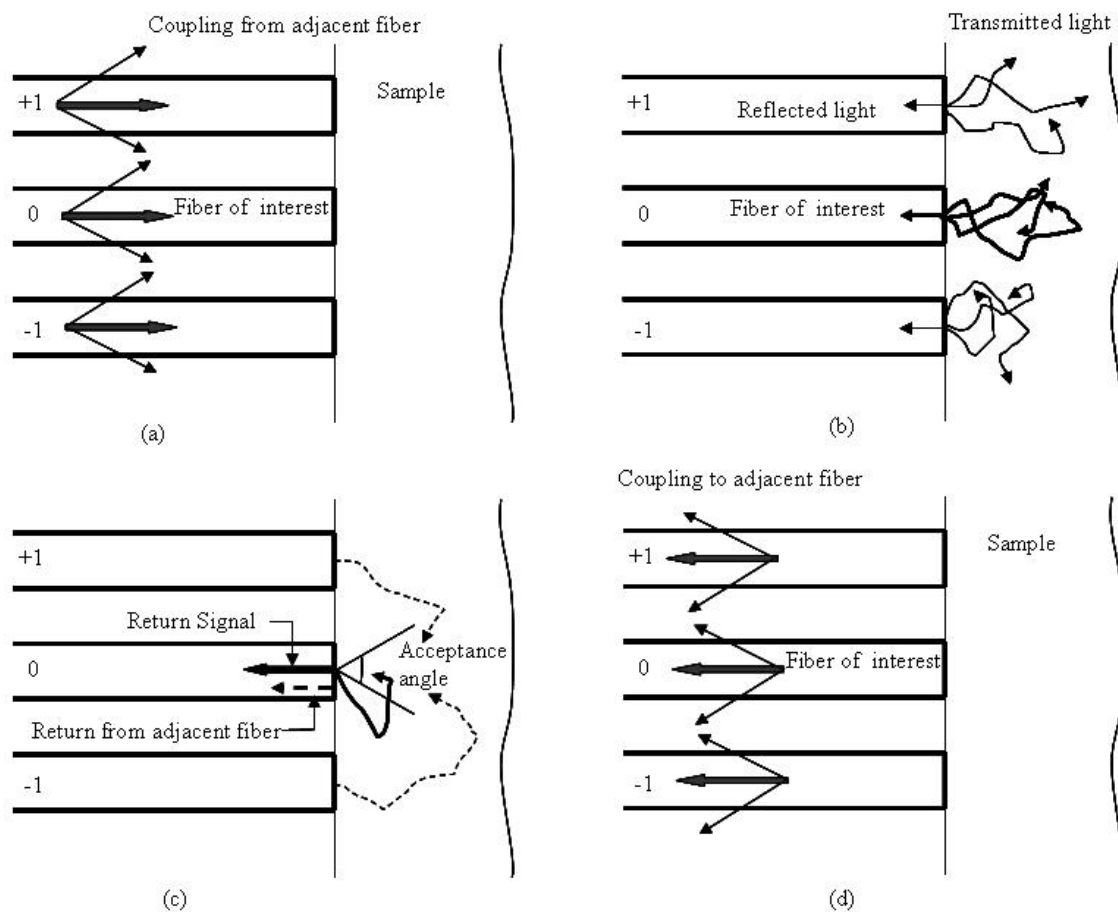


Figure 2.2. Description of a) parallel beam propagation in multiple fibers; b) light transmitted into a tissue sample and scattered; c) backscattered photons collected within the acceptance angle of the fiber; and d) return signals propagating in multiple fibers.

The photon propagation from and collection by the fiber array is analyzed without a lens. The lens was not included so that the degrading effects of inaccurate coupling, mode matching, and lens aberrations do not enter the results and therefore allows us to establish an upper bound on the performance of the fiber array. Without using a lens the depth of focus is equivalent to the Rayleigh range of the Gaussian beam emitted from the fiber

(Figure 2.3). If a lens is used and configured in a 1:1 imaging system, the beam will be focused over a distance that is twice the Rayleigh range of the fiber alone (Figure 2.3b). 1:1 imaging systems have advantages in reducing aberrations over systems with other magnification values and in this system the center spacing between fibers in the array will set the spatial resolution of the system. A fiber array without a lens may be appropriate for applications where the plane of interest is near the tissue surface.

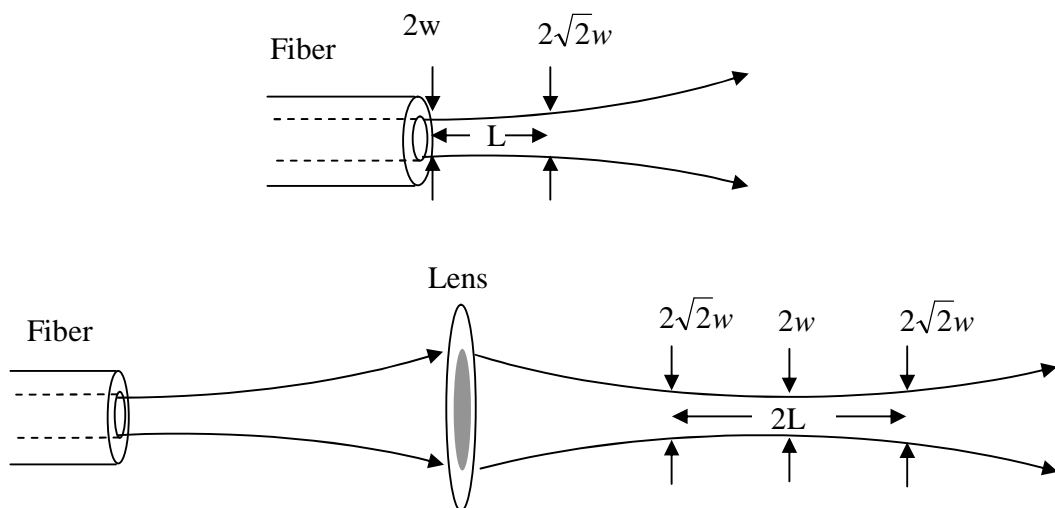


Figure 2.3. Rayleigh range from a fiber a) with ( $2LR$ ) and b) without a lens ( $LR$ ).  $2w$  is the mode field diameter of the fiber.

Field coupling between closely spaced fibers is well understood and can be accurately modeled using established beam propagation methods [23][24][25]. This technique requires the refractive index distribution  $n(x,y,z)$  of the fiber and the input

wave field  $u(x,y,z=0)$  that is launched into the fiber. The refractive index distribution for the fiber array includes the core index, cladding index, substrate index, and the index of the cement that secures the fibers to the substrate. The input field used is a Gaussian profile that matches the mode field diameter (MFD) of the lowest order stable mode in the fiber. The MFD ( $2\omega$ ) is determined by the fiber core diameter, wavelength, and numerical aperture (NA) and can be computed using the relation:

$$2\omega = d_{co} (0.65 + 1.619V^{-3/2} + 2.87V^{-6}), \quad \text{Eq. 2.1}$$

with  $V = \frac{\pi d_{co}}{\lambda} NA$  representing the V# or normalized frequency of the fiber.

Our beam propagation analysis employed a commercial simulator that uses bi-directional field propagation techniques to account for reflection and resonant effects that might arise in the structure [26]. The power in different fibers was computed as a function of the interaction length (L) to determine the compromise between packaging and coupling constraints. It is desired to have the length of the reduced fiber section long enough to securely mount on a probe tip package but short enough to limit beam coupling between fibers. The remaining length of fiber will have a larger separation distance in the endoscope and not suffer from appreciable coupling effects. For our analysis the coupling between a fiber of interest and two fibers on either side are considered with each fiber separated by a distance  $d_s$ .

Light transmitted into the scattering sample from a fiber is treated as photon propagation with a Monte Carlo (MC) model [27] to determine the percentage of light

remitted as a function of location and propagation angle, thus determining recoupling of scattered light into the launch and adjacent fibers. Light emitted from a fiber is assumed to have a Gaussian spatial profile and extends over an angular range of  $\alpha_{\max}$  corresponding to the numerical aperture of the fiber. The numerical aperture also limits the collection angle of the backscattered photons. Since the results from the model will later be compared to experimental data using an Intralipid-10% solution as a tissue phantom, the parameters for this solution were used for the MC analysis. The Intralipid-10% solution has a refractive index of 1.34, an anisotropy coefficient  $g = 0.4$ , a scattering coefficient  $\mu_s = 100\text{cm}^{-1}$ , and an absorption coefficient  $\mu_a = 20\text{cm}^{-1}$  at a wavelength of 1310 nm [28][29].

In the MC analysis each photon is initially assigned a weight of unity. When the photon is launched, there is a refractive-index-mismatch at the interface between the fiber and solution. The reflection loss at the interface reduces the photon weight by a factor of  $1 - r_{\text{sp}}$  where  $r_{\text{sp}}$  is equal to the Fresnel reflection coefficient  $\sim \left(\frac{n_s - n_c}{n_s + n_c}\right)^2$ . The MC simulation uses  $10^7$  launch photons to compute the statistical results.

Since the receiving area of a fiber core is fairly small and the scattering characteristics are radially symmetric, the collection area can be extended by using the area of a ring with the ring width equal to the fiber core diameter and a radius ( $r$ ) equal to the separation between the launch fiber and the receiving fiber of interest. This increases the number of collected backscattered photons to improve accuracy of the analysis with a

manageable computational time [30]. After counting the photons collected within the ring and applying the appropriate weight, the value is scaled by a factor of  $A_{core} / A_{ring}$  to determine the percentage of photons coupled back into a fiber. The number of backscattered photons received by a fiber is in general calculated as a function of  $r$  and  $\alpha$ .  $\alpha$  is the trajectory angle of a photon, relative to the fiber normal, backscattered into a fiber with the value of  $\alpha < \alpha_{Max}$ , with  $\alpha_{Max}$  determined by the NA of the fiber as mentioned earlier. Summing the weights of the photons received by a fiber and dividing by the total number of launched photons ( $10^7$ ) gives the fractional energy and power received by a fiber.

### 2.3. Simulation Results

Table 2.1. Fiber parameters used in the array and fraction of collected backscatter  $P_0$

Fiber Type	NA	dco( $\mu\text{m}$ )	nco	ds( $\mu\text{m}$ )	$P_0$
SMF A	0.12	8.2	1.4517	14	0.00014393
SMF B	0.16	6.0	1.4578	14	0.0001744
MMF A	0.55	9.0	1.5800	12	0.0013212
MMF B	0.25	8.0	1.4680	12	0.0004165
Fiber C	0.16	8.2	1.4517	14	0.00021408

The parameters for five different types of fibers that were used in the simulation are listed in Table 2.1. The multimode fibers MMF A and MMF B have much higher NAs than are normally found in single mode fibers (0.55 for MMF A and 0.25 for MMF B). In addition, the core diameters and NAs for these fibers are typical of those found in commercially available fiber image guides (available from Schott North America Inc.). SMF A is Corning SMF 28 fiber [31] with a  $V\# = 2.36$  and is used to form the experimental fiber array. SMF B is a commercially available single mode fiber (Stocker Yale bif-rc-1310-L2) [32] with a  $V\# = 2.30$  that has a larger NA and smaller core diameter than SMF A. Fiber C is a fiber with a larger NA but the same core diameter as

SMF A to evaluate the effect of larger NA on backscatter performance. This fiber has a  $V\#$  that is just beyond the cut-off for single mode operation. All calculations were performed at a wavelength of 1310nm and the refractive index was assumed to have a step profile. It was also assumed that an optical cement with a refractive index of 1.435 surrounds the circular fiber cladding sections. This cement index is less than the cladding index of all the fibers analyzed and corresponds to a commercially available cement (Angstrom Bond OG 134). The results for the beam propagation analysis to determine coupling to adjacent fibers and throughput as a function of interaction length (L) are shown in Figure 2.4. Coupling power was computed assuming that the fiber of interest was surrounded by two fibers on either side in a linear array. The coupling was calculated as a function of the interaction length (L) for different types of fibers to determine the maximum permissible lengths of reduced diameter fiber sections that can be used in the probe tip of an array package. The results indicate that less than -35 dB of coupling to adjacent fibers result if the interaction length (L) was kept  $< 5\text{mm}$ . The corresponding fiber throughput also remains high ( $> 94\%$ ) when L of the different etched fibers is  $< 5\text{mm}$ . Also of note in this Figure is a dip in the power coupled to the adjacent fibers. The dip for SMF A occurs near 2.7mm and for SMF B near 3.9mm. This dip results from power oscillating between the launch and adjacent fibers. The coupling analysis indicates that higher NA fibers (both single and multimode) have significantly lower coupling than low NA fibers. This results from tighter confinement of the mode field diameter of the guided beam.

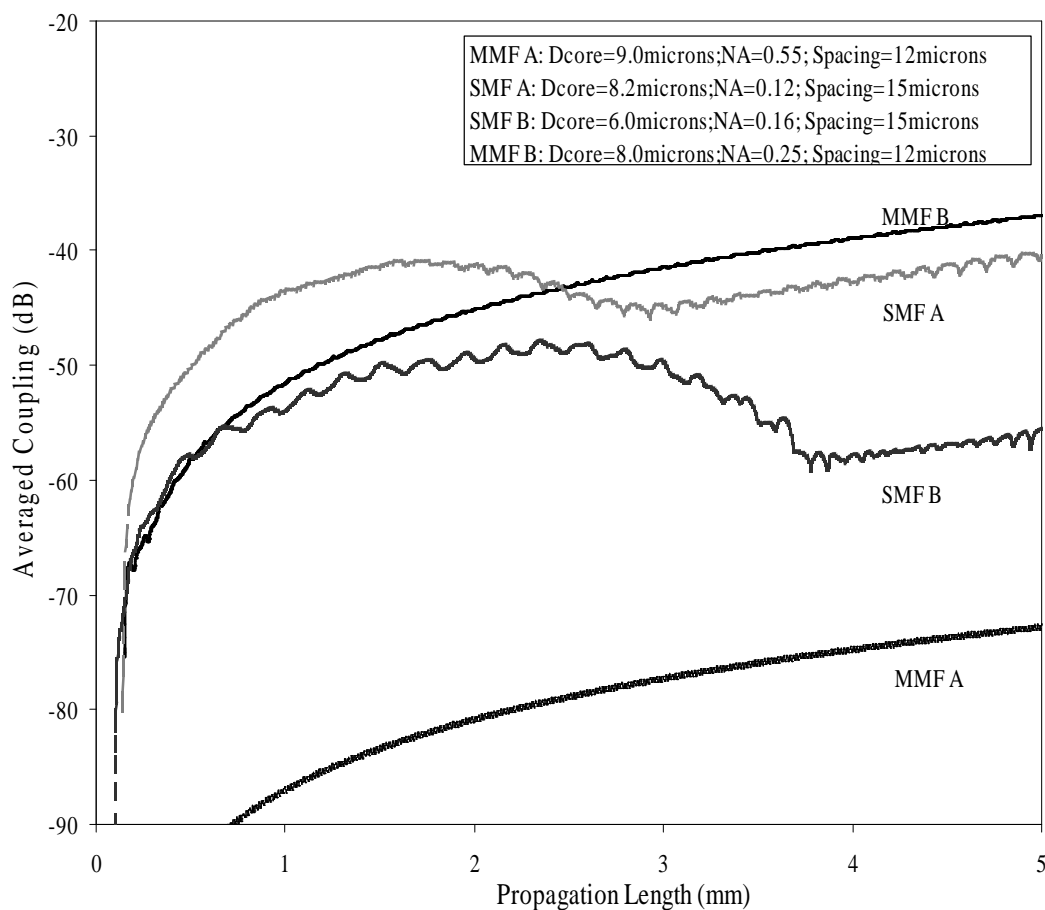


Figure 2.4. Coupling between fibers as a function of interaction length ( $L$ ). MMF A: 9.0 $\mu\text{m}$  core diameter, 0.55 numerical aperture (NA), 12 $\mu\text{m}$  fiber separation. SMF A: 8.2 $\mu\text{m}$  core diameter, 0.12 numerical aperture (NA), 15 $\mu\text{m}$  fiber separation. SMF B: 6.0 $\mu\text{m}$  core diameter, 0.16 numerical aperture (NA), 15 $\mu\text{m}$  fiber separation. MMF B: 8.0 $\mu\text{m}$  core diameter, 0.25 numerical aperture (NA), 12 $\mu\text{m}$  fiber separation.

Beam coupling between fibers is also computed as a function of fiber center spacing with fixed interaction lengths of 2 and 5mm for the two types of single mode fiber. The results are shown in

Figure 2.5. For this analysis when the separation is increased the cladding thickness is also increased so that the fibers remain in contact. If  $-35$  dB is used as a value for the maximum acceptable coupling and a 5mm reduced fiber length is needed for packaging, then a  $12\mu\text{m}$  separation is the minimum separation that can be used for SMF 28 fiber, while a separation  $<11\mu\text{m}$  is acceptable for SMF B.

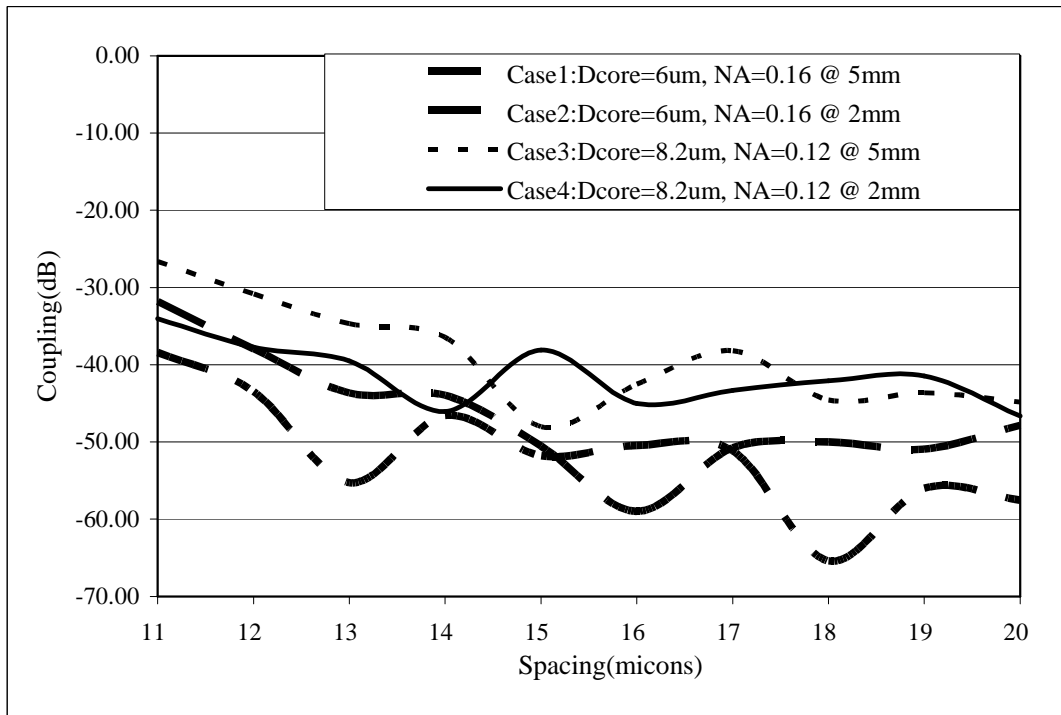


Figure 2.5. Coupling (dB) as a function of fiber separation distance ( $\mu\text{m}$ ) for SMF A and SMF B fibers described in Figure 4 with fixed interaction lengths of 2 and 5 mm.

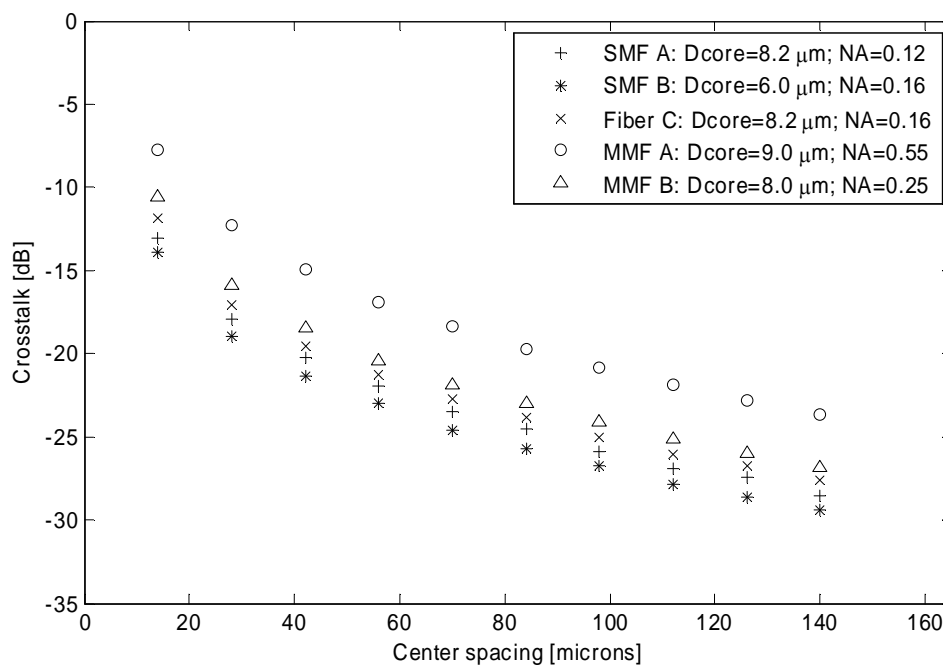


Figure 2.6. Monte Carlo simulation of backscattered light from an Intralipid 10% tissue phantom solution as a function of distance from the launch fiber.  $\circ$  9.0 $\mu\text{m}$  core diameter, 0.55 numerical aperture (NA), 12 $\mu\text{m}$  fiber separation;  $+$  8.2 $\mu\text{m}$  core diameter, 0.12 numerical aperture (NA), 14 $\mu\text{m}$  fiber separation;  $*$  6.0 $\mu\text{m}$  core diameter, 0.16 numerical aperture (NA), 14 $\mu\text{m}$  fiber separation  $\Delta$  8.0 $\mu\text{m}$  core diameter, 0.25 numerical aperture (NA), 14 $\mu\text{m}$  fiber separation;  $\times$  8.2 $\mu\text{m}$  core diameter, 0.16 numerical aperture (NA), 14 $\mu\text{m}$  fiber separation.

Smaller fiber separation distances are possible if the required interaction length is 2 mm. The oscillation of power between the launch and adjacent fibers is very noticeable in this case. The oscillation tends to decrease as the fiber separation increases as expected due to less interaction of the mode field with adjacent fibers.

Monte Carlo simulation of backscattered light collected by different types of fiber as a function of separation from a launch fiber is shown in Figure 2.6. The simulated cross-talk from a fiber of interest to adjacent fibers is computed using the following relation:

$$P_{XT-S} (dB) = 10 \log\left(\frac{P_m}{P_0}\right), \quad \text{and} \quad m = 1, 2, \dots, 10, \quad \text{Eq. 2.2}$$

where  $P_m$  is the fraction of the incident light that is backscattered and collected by an adjacent fiber, and  $P_0$  is the fraction of incident power that is back-scattered and collected by the fiber of interest (the signal). Specific values for  $P_0$  for different types of fibers are given in Table 2.1. The ratio of backscattered signal power  $P_0$  to backscattered crosstalk power  $P_{XT}$  is plotted for each type of fiber in

Figure 2.7. The results indicate that a trade-off exists between NA and core diameter for optimizing  $P_0/P_{XT}$ . Increasing the NA will in general increase both  $P_0$  and  $P_{XT}$ , but decreasing the fiber core diameter reduces  $P_{XT}$  and increases the  $P_0/P_{XT}$  ratio. This suggests that fibers with larger NA and small fiber cores (SMF B) will provide good scattered signal detection in array configurations. This finding indicates that single mode fibers may be suitable since the core diameter can be reduced to keep the  $V \# < 2.405$  for single mode operation and still have good signal collection efficiency.

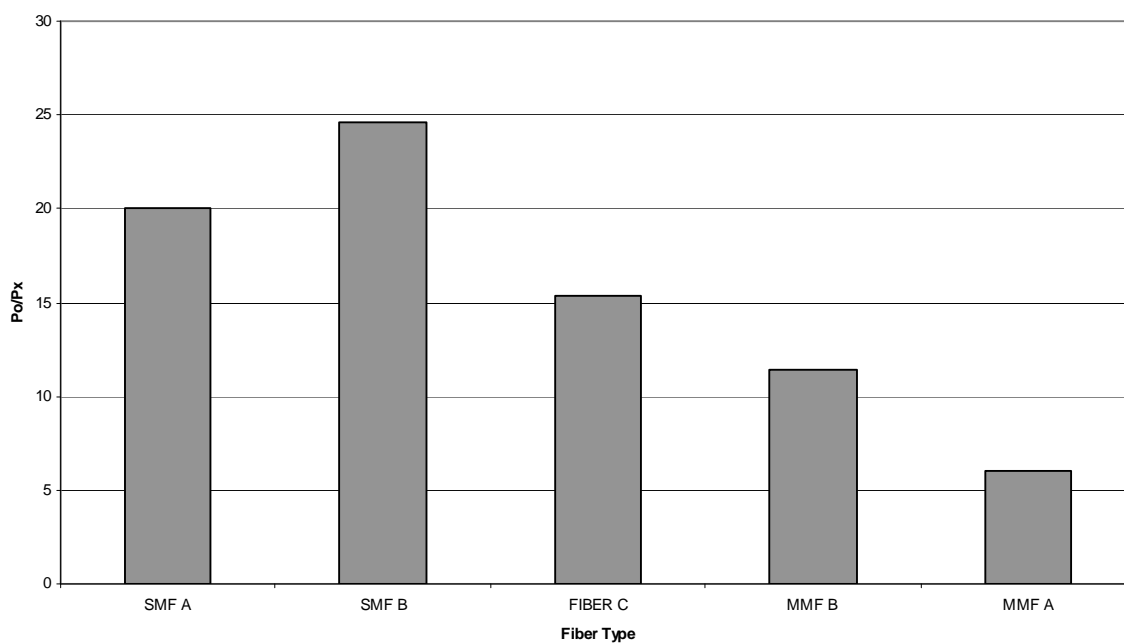


Figure 2.7. Ratio of backscattered signal ( $P_o$ ) to backscattered cross-talk ( $P_x$ ) as a function of different fiber type (NA/dc).

## 2.4. Fiber Fabrication Technique

### 2.4.1. Reduced Diameter Fiber

The desired  $15\mu\text{m}$  diameter single mode fibers are not readily available. Therefore, communication grade  $125\mu\text{m}$  diameter single mode fibers were etched to a  $15\mu\text{m}$

diameter. Only a small section (~2-3mm) of one of the fiber end that will be placed in the array package needs to be etched. The remainder of the fiber section can have a larger diameter. This is an advantage as the small diameter is fragile.

Corning SMF-28 single mode fibers [31] were selected for the array. This fiber is single mode at 1310nm, has a core diameter of 8.2 $\mu$ m, a cladding diameter of 125 $\mu$ m, a core refractive index of 1.4517, and a cladding index of 1.447.

The fibers were etched using a buffered oxide etching (BOE) process described previously [33]. The basic procedure consists of stripping the plastic fiber covering, cleaving the ends, and suspending the fiber tips in a container with BOE solution. The etching process is linearly dependent on the time the fibers are immersed in the solution. The etch time was accurately controlled by attaching the fibers to a motorized stage and slowly withdrawing the fibers from the etching solution. The process was computer controlled and takes about 7.5 hours to complete. The process allows multiple fibers to be etched at the same time and the slow withdrawing process tapers the fiber. The taper improves the strength of the etched fiber sections. Figure 2.8 and Figure 2.9 show the resulting etched fiber sections. The cross section of the etched tapered fiber is shown in Figure 2.8, and Figure 2.9 shows a photograph of an etched fiber end against a calibrated square that is 25 $\mu$ m on a slide.

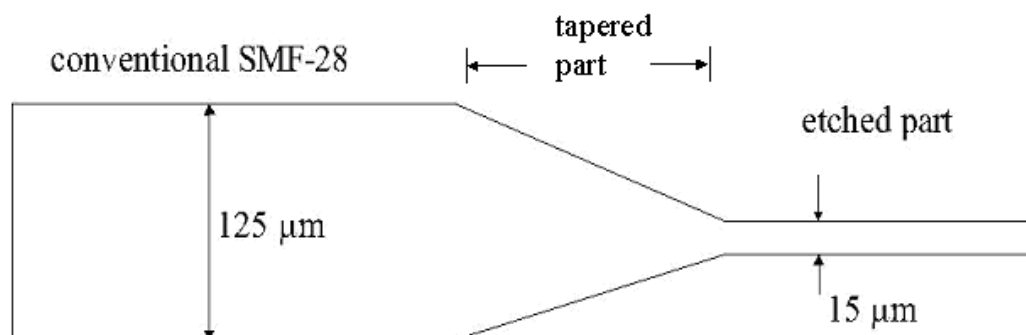


Figure 2.8. Resulting fiber side view after etching process. The length of the  $15\ \mu\text{m}$  diameter section is less than 3mm and the tapered section is  $\sim 3\text{-}4\text{mm}$  [34].

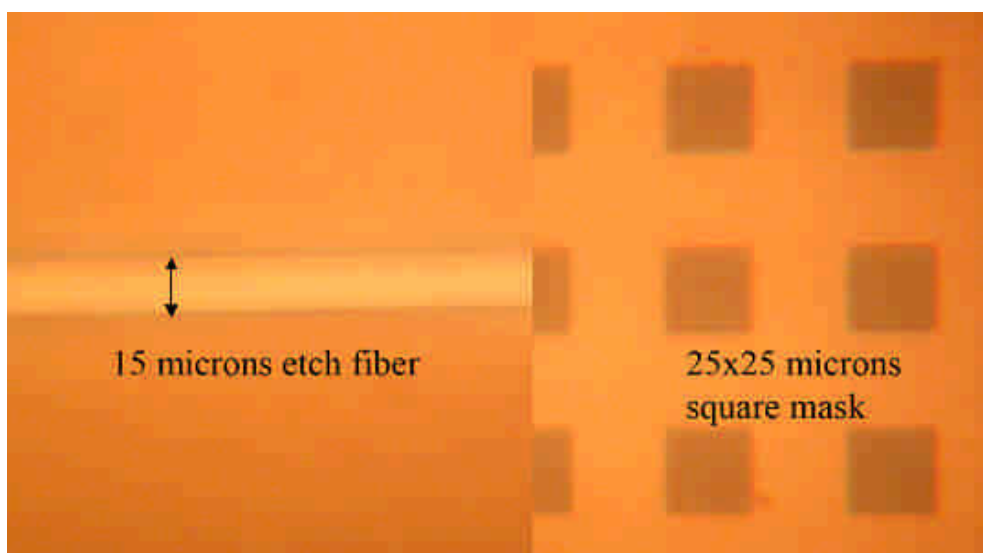


Figure 2.9. Picture of the etched fiber section next to a mask with  $25\ \mu\text{m}$  squares [34].

### 2.4.2. Single Mode Fiber Array

One version of the fiber array consists of SMF 28 fibers that have been etched to  $\sim 15\mu\text{m}$  diameters mounted in a silicon V-groove array with  $15\mu\text{m}$  groove spacing as shown in Figure 2.10. However, mounting fibers in the V-groove was not very repeatable since keeping the  $15\mu\text{m}$  fibers in position while the next fiber was placed in the adjacent groove was very difficult.

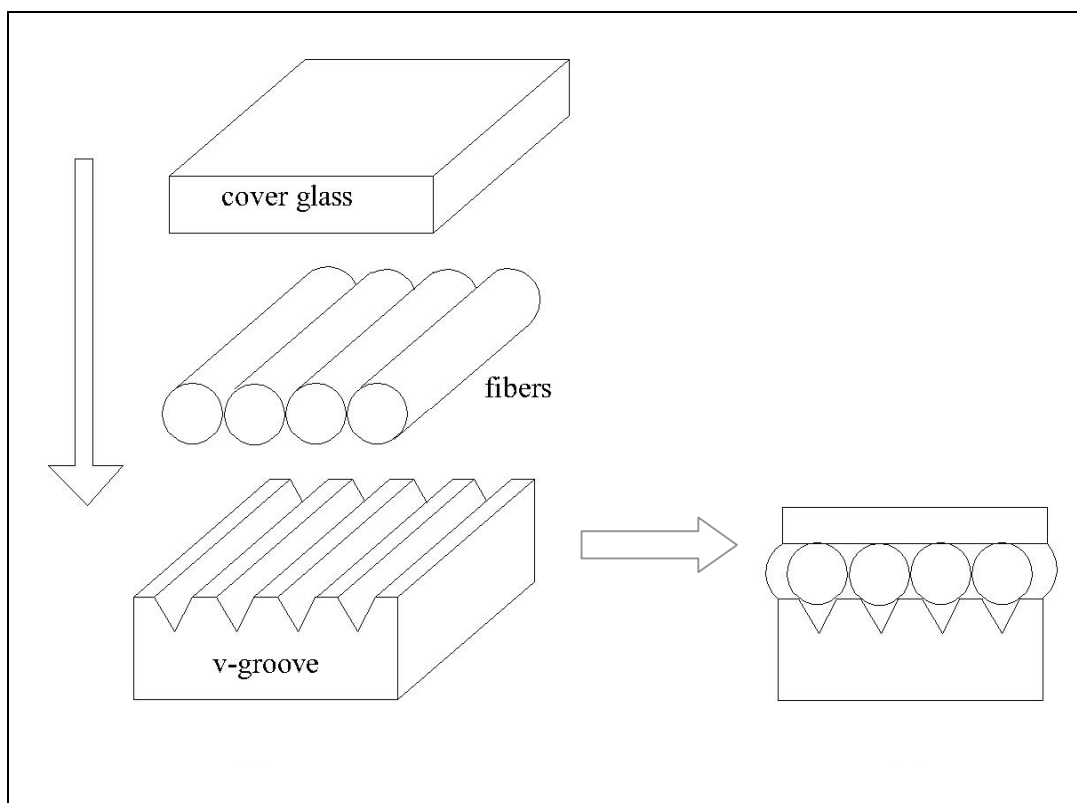


Figure 2.10. Array assembly procedure with V-groove [34].

An alternate approach to mount the fibers was to place the fibers in trench formed in a silicon substrate. Similar to the first approach, the reduced diameter fibers were mounted in a silicon trench with a depth of  $13.5\mu\text{m}$ , as shown in Figure 2.11. The etched fiber tips have a 2mm-long linear tapered section between the etched and standard fiber diameter sections. Pressure was applied to the reduced diameter fiber ends to keep them aligned and adjacent to each other. The fibers were cemented in place with an UV curable epoxy (Angstrom Bond OG134) with a refractive index of 1.435 that is lower than the core index of the fibers (1.4517) to help confine the field mode of the fiber within the the core region. The cured sample was then cut with a dicing saw (780, Kulicke & Soffa.), and polished to provide a good optical surface. An 8-fiber array is shown in Figure 2.12 [35].

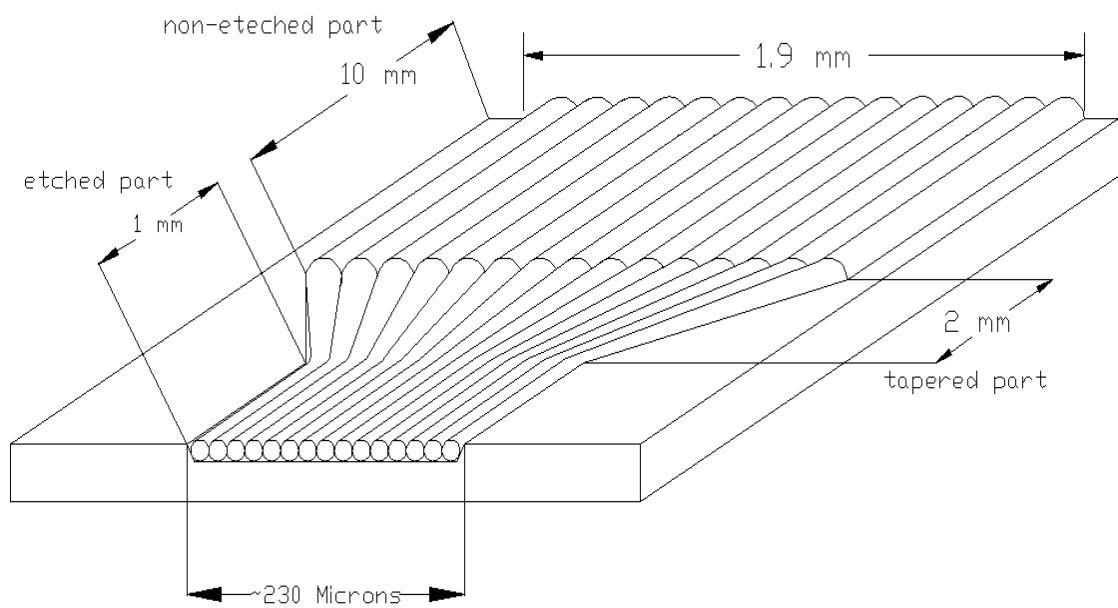
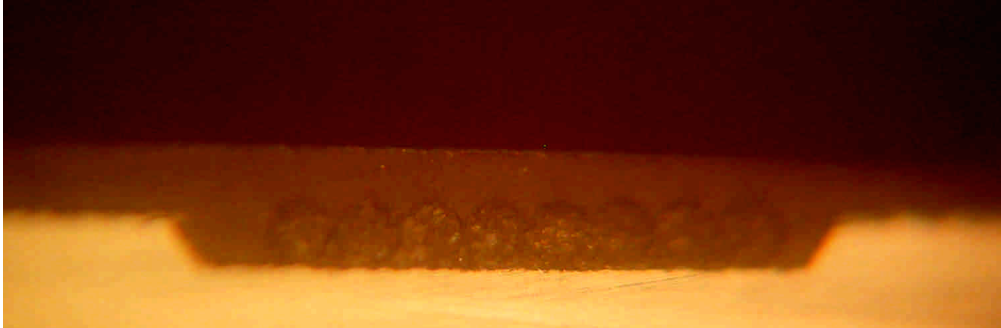
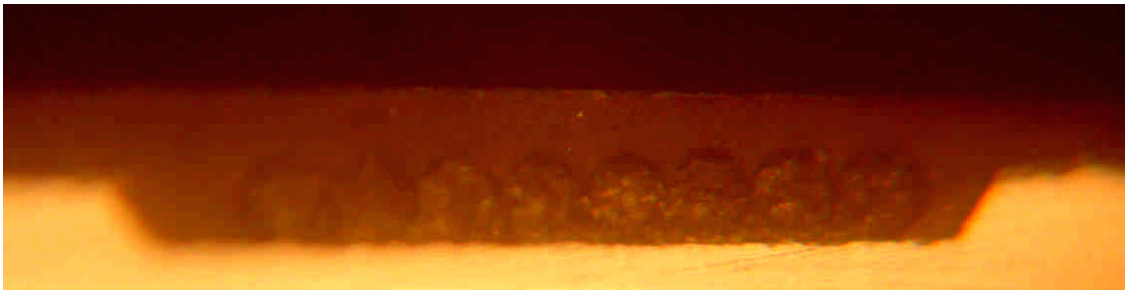


Figure 2.11. Schematic of linear fiber array with 15 channels and silicon trench groove.



(a)



(b)

Figure 2.12. (a) Schematic of linear fiber array with 8 channels and silicon trench. (b) Zoomed in on the fiber array.

### 2.4.3. Fiber Cross-Talk Measurements

The experimental system for measuring light scattered from a tissue phantom solution and coupled back into different fibers in the array is illustrated in Figure 2.13. Light from a 1310 nm super luminescent light emitting diode (SLD) is coupled to an input fiber of a 3 dB fiber coupler and one output fiber from the coupler is connected to a fiber of interest in the array. The other output fiber from the coupler is connected to a

detector 3 to monitor the input power level of the source. The second input fiber to the coupler is used to measure the backscattered signal returning to the fiber of interest, and the backscattered signal can be measured at detector 1. Backscattered light that is coupled to adjacent fibers in the array is measured by successively coupling detector 2 to each of the adjacent fibers. Backscattered signals were measured from an undiluted Intralipid-10% solution and normalized to measurements from a 0.9% saline reference solution to remove contributions from interface reflections and background noise. It was necessary to use a concentrated Intralipid-10% solution to provide measurable cross-talk signals. While Intralipid-10% has a higher reduced scattering coefficient than most tissues, it is useful in obtaining robust signals for comparison with simulation results [36].

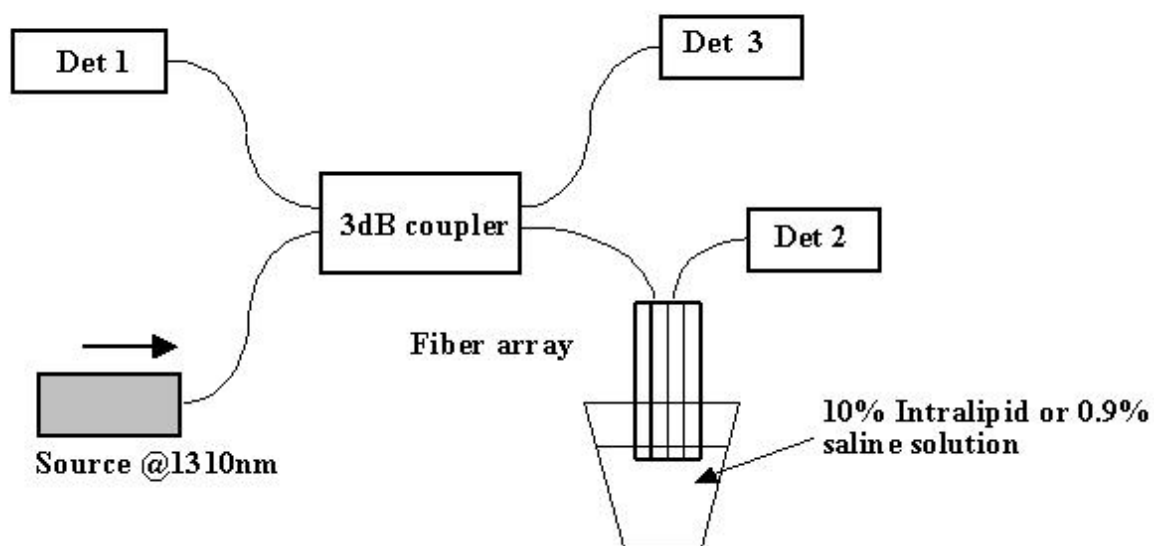


Figure 2.13. Experimental system for measuring the backscattered signal to a fiber of interest and cross-talk to adjacent fibers in an array. The source is a super luminescent diode with a center wavelength of 1310 nm and Det 1, Det 2, and Det 3 are detectors.

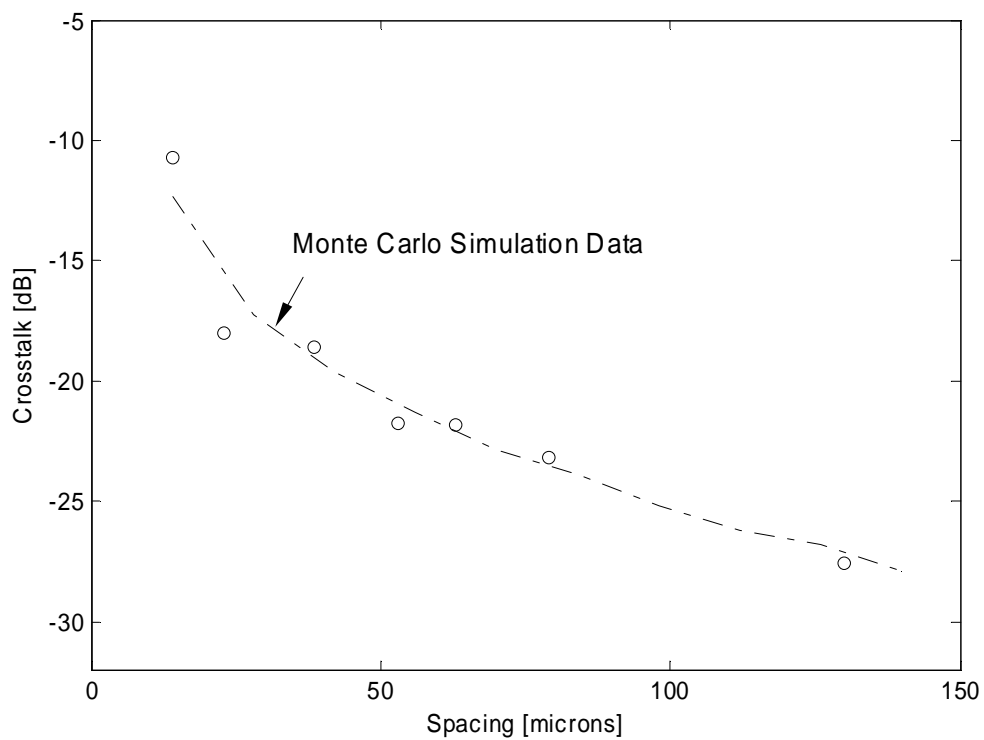


Figure 2.14. Experimental data (circular dots) for crosstalk measure from an Intralipid 10% solution with a fiber array consisting of fibers with  $8.2\mu\text{m}$  core diameters, 0.12 NA, and  $15\mu\text{m}$  fiber separation.

Figure 2.14 [37] shows the experimental backscattered cross-talk values obtained with the fiber array as a function of radial distance from the center of the launch fiber. Data samples were obtained to a radial distance equivalent to 10 fiber diameters (150 $\mu$ m). The cross-talk values (PE-XT) of the scattering experiment are determined using the relation:

$$P_{E-XT} (dB) = 10 \log \left[ \frac{P_{adjacent}}{P_{signal}} \right] = 10 \log \left[ \frac{(B_I - B_S) \left( \frac{1}{T_{adjacent}} \right)}{(A_I - A_S) \left( \frac{1}{T_{launch}} \right) \left( \frac{1}{R_{3dB}} \right)} \right], \quad \text{Eq. 2.3}$$

where  $B_S$  and  $B_I$  are the optical power values measured respectively by detector 2 with the 0.9% saline and Intralipid-10% solutions.  $A_S$  and  $A_I$  are the optical power values measured respectively by detector 1 with the 0.9% saline solution and Intralipid-10% solution. The parameter  $T_{adjacent}$  represents the transmission efficiency ( $I_{out} / I_{in}$ ) of the adjacent fiber in the fiber array,  $T_{launch}$  represents the transmission efficiency of the launch fiber in the fiber array, and  $R_{3dB}$  represents the splitting ratio of the coupler for the returned signal through the fiber connected to the detector 1. These transmission and splitting ratio values were measured prior to the experiment.

#### 2.4.4. Coherent Depth Measurement with Reduced Fiber Diameter Array

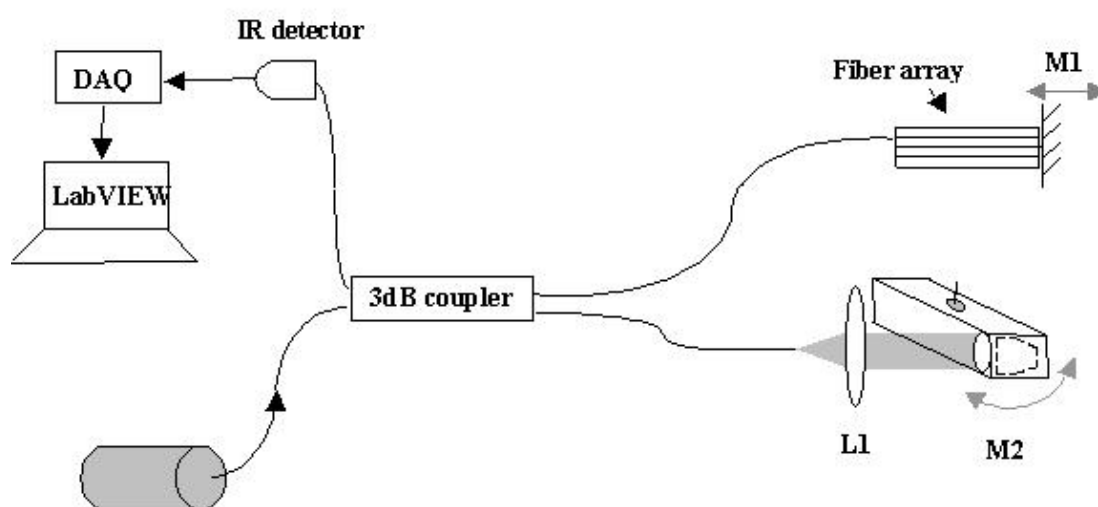


Figure 2.15. Experimental coherent fiber system for measuring distances with the experimental fiber array. DAQ is a data acquisition card; M1 is the mirrored translated from the fiber array; L1 is a lens focusing light onto a moving mirror M2.

The reduced diameter single mode fiber array was used in a coherent distance measurement system. The experimental system is illustrated in Figure 2.15 and consists of a fiber interferometer attached to one of the fibers in the array. The source has a center emission wavelength of 1310 nm and a spectral bandwidth of 40 nm. The free-space coherence length is [16]

$$l_c \approx 0.44 \frac{\lambda_0^2}{\Delta\lambda} = 19 \mu\text{m}, \quad \text{Eq. 2.4}$$

SMF 28 fiber has a  $V\# = 2.36$  and a mode field diameter ( $2w$  from Eq. 4.2) of 9.129  $\mu\text{m}$ . The resulting Rayleigh range is:

$$z_R = \frac{\pi(2w)^2}{4\lambda} = 50 \mu\text{m}, \quad \text{Eq. 2.5}$$

The system uses a mirror (M2) on a galvo system to scan the coherence region over a distance of 1.18 mm at a rate of 0.5 Hz. The output from the signal fiber is reflected from a mirror (M1) that is mounted on a micrometer stage for accurate positioning relative to the tip of the fiber. Figure 2.18 shows the interference patterns acquired using a LabView control program at distances of 50, 150, and 250  $\mu\text{m}$  from the end of the fiber. Although the amplitude of the fringe pattern decreases with distance the signal is sufficient at 250  $\mu\text{m}$  to measure the presence of the surface. This experiment indicates that reduced fiber diameters that are packaged in an array can be used to measure surfaces without a focusing lens that are considerably farther from the fiber tip than the Rayleigh range.

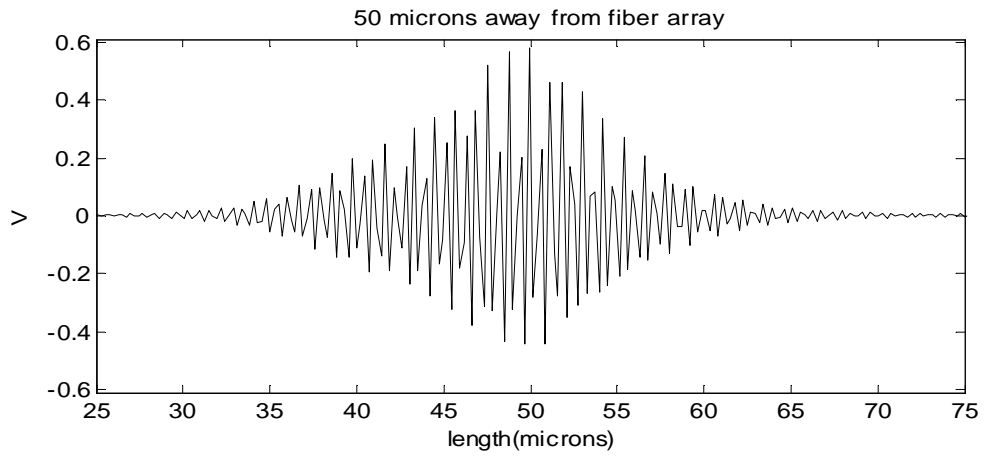


Figure 2.16.(a) Interference fringes formed within the coherence length of the source with the mirror M1 located  $50\mu\text{m}$  from the edge of the fiber array.

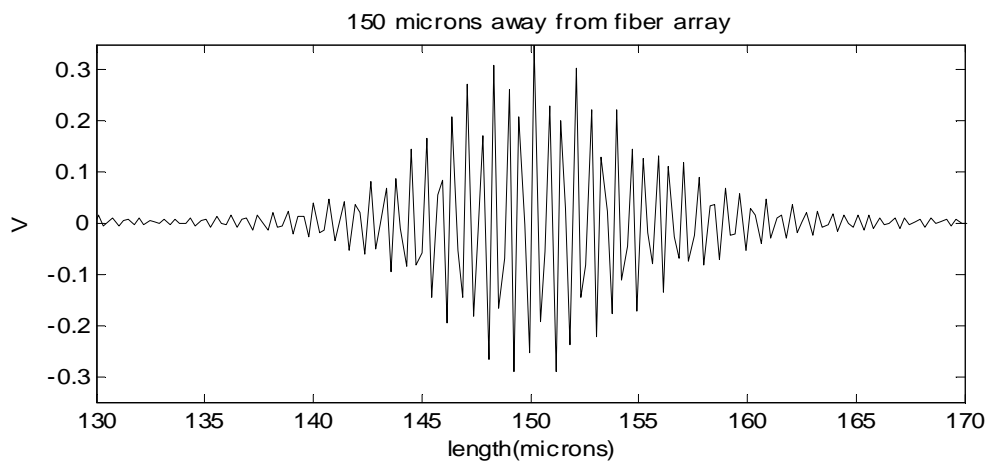


Figure 2.17.(b) Interference fringes formed within the coherence length of the source with the mirror M1 located  $150\mu\text{m}$  from the edge of the fiber array.

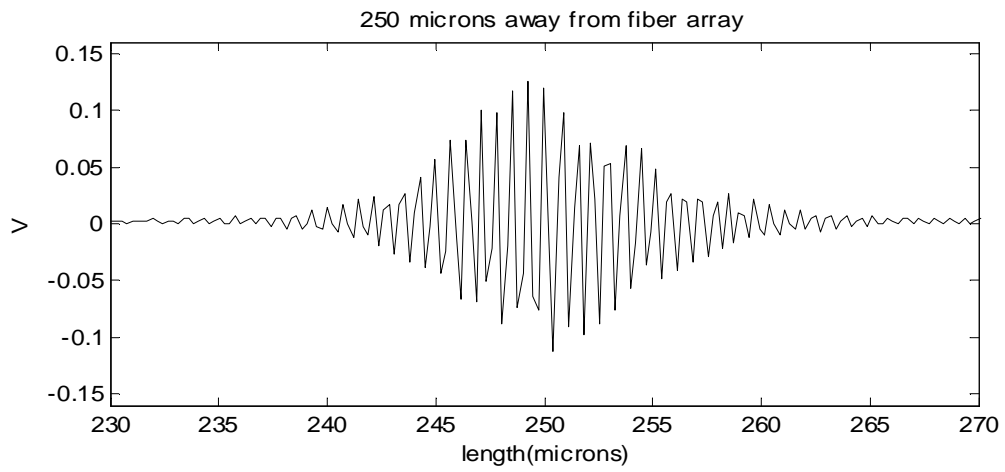


Figure 2.18.(c) Interference fringes formed within the coherence length of the source with the mirror M1 located  $250\mu\text{m}$  from the edge of the fiber array.

## Chapter 3. Parallel Optical Coherence Tomography System

### 3.1. Introduction

A parallel optical coherence tomography (POCT) imaging system can be adapted to an endoscopic format. In this Chapter, the design and procedures for implementing the POCT imaging system will be introduced. The POCT system consists of a single mode fiber (SMF) array with multiple reduced diameter (15 $\mu$ m) SMFs in the sample arm with 15 $\mu$ m center spacing between fibers. The size of the array determines the size of the transverse imaging field. Electronic scanning eliminates the need for mechanically scanning in the lateral direction. Experimental image data obtained with this system show the capability for parallel axial scan acquisition with lateral resolution comparable to mechanically scanned OCT systems.

### 3.2. Fiber Array and Probe Assembly

#### 3.2.1. Single Mode Fiber Array

The system probe tip is formed by a GRIN lens and the fiber array, which has been discussed in Chapter 2. The fiber array used in the demonstration POCT system has 8, 15  $\mu$ m diameter fibers. Arrays with 15 fibers have also been fabricated. Neglecting Fresnel reflections, the measured transmission efficiency ( $\eta = 100 \% \times P_{out} / P_{in}$ ) of each fiber is greater than 90%. Transmission data for the 8 channel array are shown in the Table 3.1.

This result indicates that high optical quality of the reduced fiber section and the fiber end surface can be achieved with the fiber etching and end face preparation technique.

The crosstalk from a signal fiber to the adjacent fibers is defined using the relation of  $P_{xt}(dB) = 10\log(P_{adjacent}/P_{signal})$ , where  $P_{adjacent}$  and  $P_{signal}$  is the output of the fiber immediately adjacent to the signal fiber, and the signal fiber, respectively. The measured crosstalk between the signal and adjacent channels is less than -30 dB.

Table 3.1. Channel transmission efficiency

Channel	$\eta$ (%)
1	92%
2	96%
3	91%
4	93%
5	93%
6	98%
7	91%
8	97%

### 3.2.2. Assembled Probe Tip

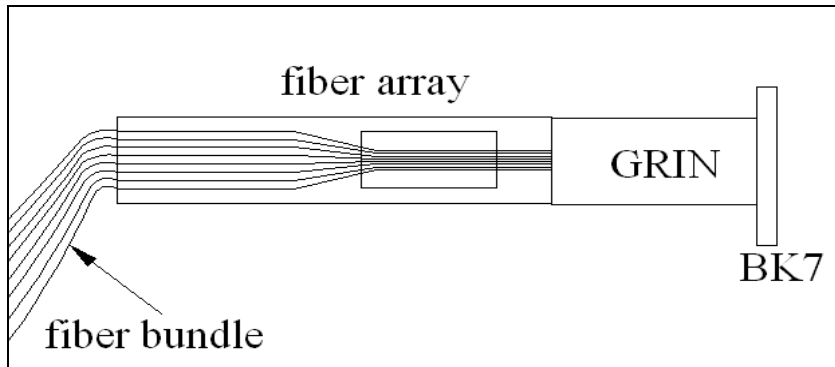


Figure 3.1 Diagram of the assembled probe end of the POCT system.

A GRIN-rod lens provides a compact imaging element that is useful in fiber endoscope systems [22]. A 1:1 imaging configuration was chosen to reduce aberrations and provide good signal collection efficiency with minimal overlap of adjacent beam profiles. A commercially available GRIN rod (Quantum Focus, Corning) with 1.8 mm outside diameter was cut to at fractional pitch (FP) of  $\sim 0.48$  at a wavelength of  $1.31 \mu\text{m}$ . The lens images the fiber core to a distance of  $\sim 250 \mu\text{m}$  beyond the last surface of the endoscope in air. A BK7 glass cover with a thickness of  $0.2 \text{ mm}$  was used to protect and isolate the GRIN lens from the object environment. It was cemented to the GRIN lens with a UV curable epoxy (Norland NOA74) to minimize back-reflections. The epoxy had a coating thickness of  $\sim 20 \mu\text{m}$  and a refractive index of  $\sim 1.54$  at a wavelength  $1.31 \mu\text{m}$ . The optical design for the assembled probe tip is shown in Figure 3.1. A  $0.2 \text{ mm}$  thick

rigid stainless steel tube with 2 mm outer diameter and 1.8mm inner diameter was used to house the assembled probe tip, and the configuration is shown in Figure 3.2.

The GRIN lens has an image plane which is formed at the fiber ends mounted on the probe tip. The location of this plane must be slightly greater than 1:1 because one end of the GRIN lens is glued to a BK7 cover glass. Zemax optical modeling software (Zemax Development Corporation, WA) was used to characterize beam propagation through the GRIN lens and fiber ends. Gaussian beam ray tracing analysis features of Zemax were used to characterize the beam waist properties at the image plane. It was assumed that the tissue had a refraction index of 1.35 at a wavelength of  $1.31\mu\text{m}$  and the beam waist at the input of GRIN lens was  $9.0\mu\text{m}$ , which is the mode field diameter (MFD) of the SMF-28. Simulation results show that the system has a paraxial magnification was  $-1.01$ , with a Strehl ratio of 0.95. The system forms an aberration-free  $9.1\mu\text{m}$ -diameter beam waist and images the fiber core to a distance of  $257\mu\text{m}$  beyond the outer edge of the BK7 cover slip. Analysis of the focal position and beam diameter for the fibers at the center and edge position of the 8 element fiber array indicated that they were nearly equal.

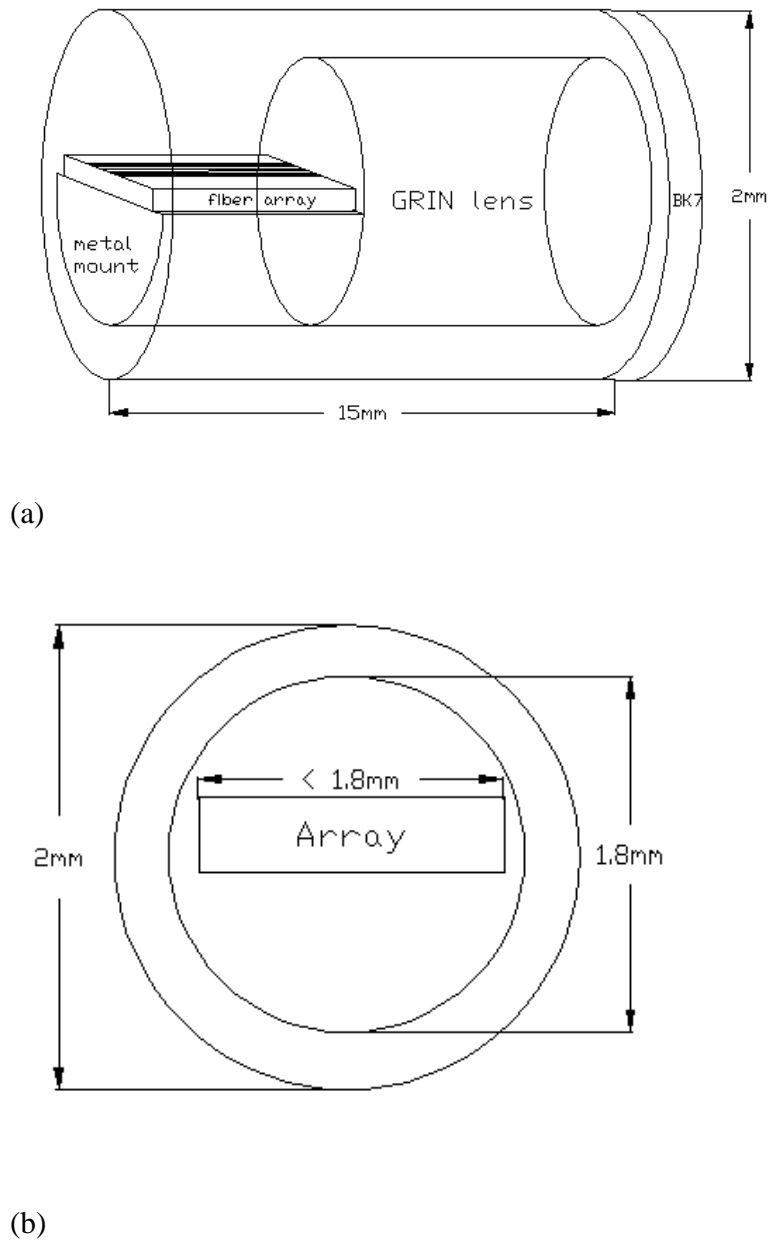


Figure 3.2. Diagram of the endoscopic assembled probe with a 0.2mm thick rigid stainless steel tube (a) lateral view (b) front view.

### 3.3. Fiber-Length Equalization

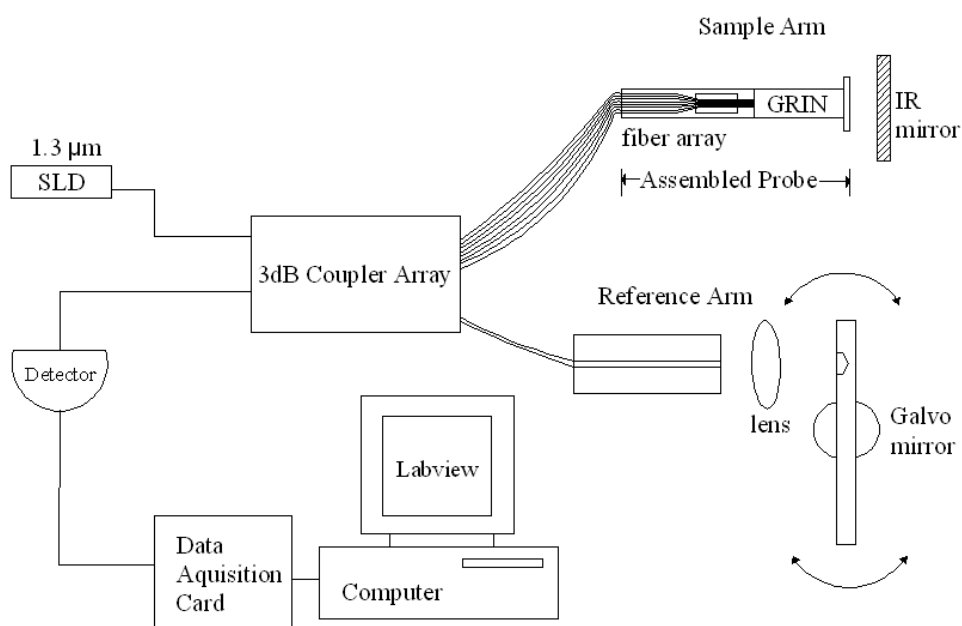


Figure 3.3. Schematic of the interferometer used to equalize fiber-lengths in the fiber array. Light from a SLD is split between the reference and sample fibers by passing it through a 3dB coupler. The probe end illuminates an IR mirror, and the reference end illuminates a galvo mirror. The return signal from a paired sample and reference arm is coupled into an output fiber that transfers the combined interference signal to an IR detector.

To obtain an interference pattern with the interferometer system, the path length difference between the reference and sample arm must be less than the coherence length of the source. Since the time-domain POCT system described in this study consists of multiple fiber interferometers, each paired reference and sample fiber length was equalized to within the scanning range of the galvanometer to provide overlap of the coherence region. For our system, the scanning range was 2mm in air. The fiber lengths of each pair of fibers in the array were equalized using the fiber interferometer shown in Figure 3.3 to within 19 $\mu$ m.

Light from a superluminescent light emitting diode (SLD) with a center wavelength of 1.31 $\mu$ m and a spectral bandwidth of 40nm was split between the reference and sample fibers by passing it through a 3dB coupler (SMC-11350229U, FIS, Inc.). An array of 3dB couplers was assembled into a junction box with standard FC-APC connectors so that each fiber could be quickly tested. Each fiber in the assembled endoscope was fusion spliced to a connectorized fiber end, forming an overall sample arm fiber length of ~1meter. In the reference arm, the light was collimated and reflected from a galvanometer-mounted retroreflector. Focused light reflected from a stationary infrared mirror in the sample arm recombined with the reference arm light on the surface of the infrared detector. A translation stage in the reference arm allowed for adjustment of the path-length difference for distances greater than the 2 mm modulation of the galvanometer-mounted reference mirror. The interference pattern of each paired sample and reference fiber was observed. To accomplish length equalization, a fiber in the reference arm with the shortest path length difference was picked as the reference position for the other

fibers. A LabView program controlled the measurement process of the path length difference. The amplitude of the interference pattern was recorded as a function of the position of the reference mirror and computed the difference in path lengths of the arms of the interferometer. The fibers in the reference arms were cleaved precisely so that the difference among the fringe positions was no more than the scanning range of galvanometer. The remaining position difference was calibrated and compensated by software. This equalization technique was first proposed in [33][37]. The path length difference achieved between all paired channels was less than 1.3mm in air.

### 3.4. Image Acquisition

Figure 3.4 shows the schematic for the parallel OCT system. The sample arm of the POCT consists of the assembled fiber array-GRIN lens-cover glass endoscope. The transverse sampling of the system is determined by the fiber-to-fiber spacing (15  $\mu\text{m}$  in this configuration). Since the assembled probe is in a  $\sim 1:1$  imaging system, the transverse resolution of the system is also  $\sim 9.1\mu\text{m}$ . The axial resolution of the system was calculated to be  $\sim 19\mu\text{m}$  assuming a Gaussian spectral distribution and using the formula [16]:

$$\Delta z_{FWHM} = 2 \frac{\ln 2}{\pi} \cdot \frac{\bar{\lambda}^2}{\Delta \lambda} \approx 0.44 \frac{\bar{\lambda}^2}{\Delta \lambda}, \quad \text{Eq. 3.1}$$

where  $\Delta \lambda$  is the full width at half maximum (FWHM) of the source measured in wavelength units and  $\lambda$  is the center wavelength of the source. The measured axial resolution was  $21\mu\text{m}$ .

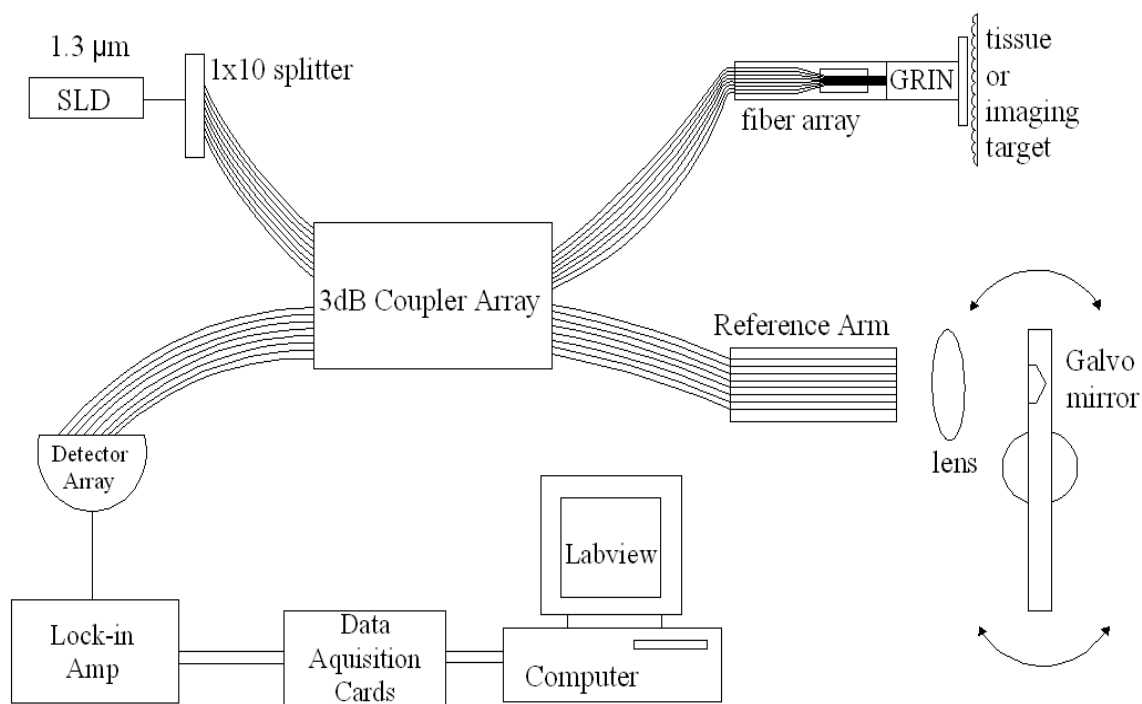


Figure 3.4. Parallel OCT system setup. Light from a SLD is coupled into a parallel fiber array through an array of 3-dB couplers mounted in a box. The probe end illuminates a target sample, and the reference end illuminates a galvo mirror. The return signal from a sample and reference arm pair is coupled into an output fiber that transfers the combined interference signal to an IR detector.

The equalized reference arm fibers were placed in a commercially available silicon based 16-fiber V-groove substrate (VGC-16-250, OZ Optics Ltd.) with center-to-center spacing of  $250\mu\text{m}$ . The optical elements in the reference arm were designed to minimize sensitivity to the lateral fiber position and maximize the power coupled back into the fiber from the galvo mirror. In addition, the fiber lengths between the  $1\times 10$  splitter and 3dB coupler array had different lengths ( $\Delta\ell$ ) to avoid coherent interference effects between channels. The variations were made greater than the coherence length of the source to prevent interference. For practical considerations the variation in fiber length between channels in our system was 1 cm (much larger than required). However, each reference and signal fiber length was matched within the scanning range of the galvanometer. The actual variation between fiber channels in our system was 1cm and the difference between the shortest and longest channel was  $\sim 8\text{cm}$ .

The detector array consisted of eight IR detectors. The interference signal of each paired sample and reference fiber was detected by its corresponding IR detector. After amplification and filtering, each detector signal was demodulated using a lock-in amplifier (SR810, Stanford Research Systems, Sunnyvale, Cal.). Because of the limited availability of lock-in amplifiers, signal data was acquired from successive elements with one lock-in amplifier and then assembled to form an image. LabView software was used for data acquisition and controlling the galvanometer. An image processing algorithm was used to reconstruct the image from the measured data. This proof-of-principle process can be used for stationary objects. In the subsequent images, the dynamic range

of the POCT signal has been compressed with a logarithmic operation and the depth was scaled by the average refractive index of the sample. All images are  $120\ \mu\text{m}$  (8 fibers  $\times 15\ \mu\text{m}$  fiber separation) in width. Images were acquired at a reference arm scan rate of 14 Hz. According to the method of Tumlinson et al [38], system dynamic range was measured to be 66 dB.

Figure 3.5 shows the POCT image of the central portion of a contact lens. Two bright boundaries correspond to the air-lens and lens-air interfaces of the contact lens. The scan depth was 1mm deep, and 1000 points per depth scan were obtained. Since the index of refraction of the contact lens was unknown, the figure has not been scaled by its index. The resultant depth in Figure 3.5 gives the optical depth of the contact lens was measured approximately  $300\ \mu\text{m}$ .

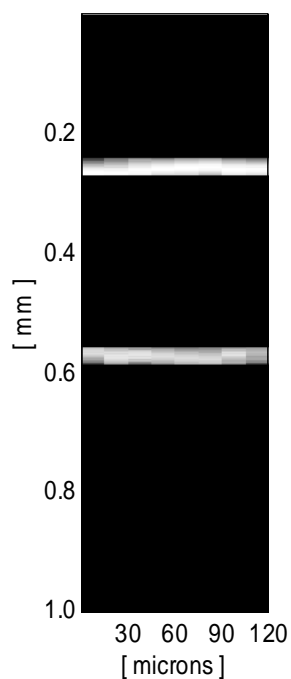


Figure 3.5. The POCT image of the central portion of a contact lens. The resultant depth is  $\sim 300\mu\text{m}$  with  $120\mu\text{m}$  ( $8 \times 15\mu\text{m}$ ) wide.

Figure 3.6(a) shows a cross section diagram of a silicon wafer with a small depression, which was measured  $\sim 50\mu\text{m}$  wide and  $\sim 70\mu\text{m}$  deep by a profilometer. Figure 3.6(b) is the POCT image of the depression in the wafer. 750 points were acquired with each point corresponding to a depth of  $1\mu\text{m}$ . Channels 3, 6 and 7 appear dim because of the angled nature of the target in that region. Some or all of the specular reflection from these sloped regions fell outside the range of the numerical aperture (NA) of the endoscope optics so only the small amount of diffuse light is measured. The depth of the

depression was measured to be  $\sim 75 \mu\text{m}$  and the width  $\sim 45 \mu\text{m}$  in agreement with the independently measured trench parameters.

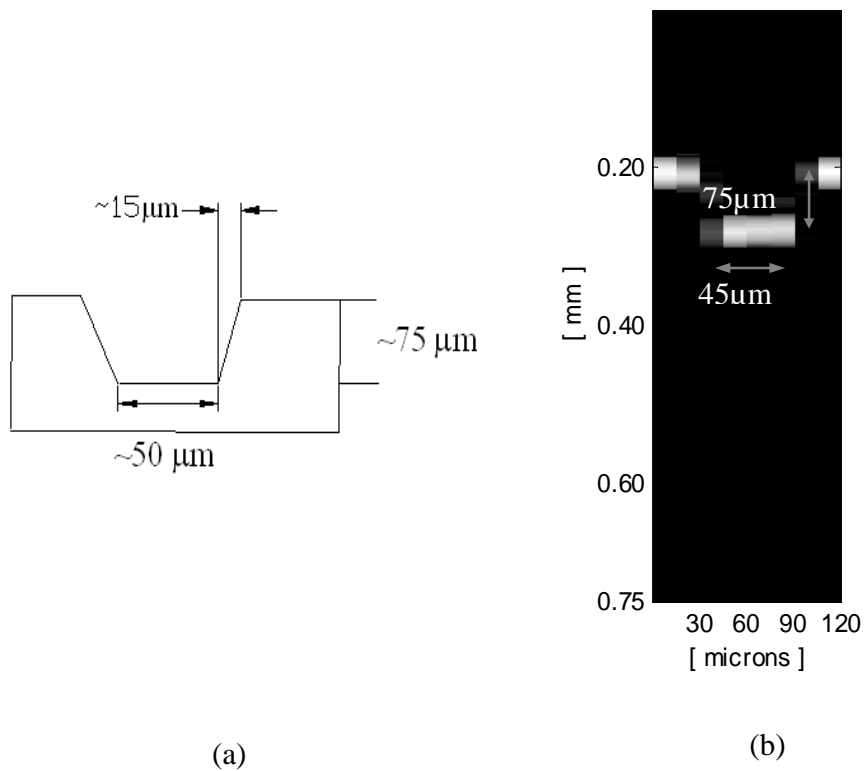


Figure 3.6(a). Side view of a silicon ( $50 \times 50 \mu\text{m}$  inner square) depression with a depth of  $70 \mu\text{m}$  was measured by a profilometer. (b) The POCT image of the depression showing a depth of  $75 \mu\text{m}$ . The width of the inner layer is  $45 \mu\text{m}$ .

Figure 3.7 is an image of tangerine (*Citrus reticulata*) flesh. The scan depth was 2mm, and 1000 points per depth scan were obtained. The figure has been scaled assuming an average index of refraction of 1.34. The juice vacuole is surrounded by a thin membrane. The membrane outline is seen as high reflectivity structures in the POCT images. Approximately 80 to 200  $\mu\text{m}$  diameter vacuoles are visible and appear as dark regions in the POCT image. Figures 6, 7 and 8 demonstrate the capability of the POCT system to image the depth, width, and/or thickness of targets without lateral scanning of the sample arm.

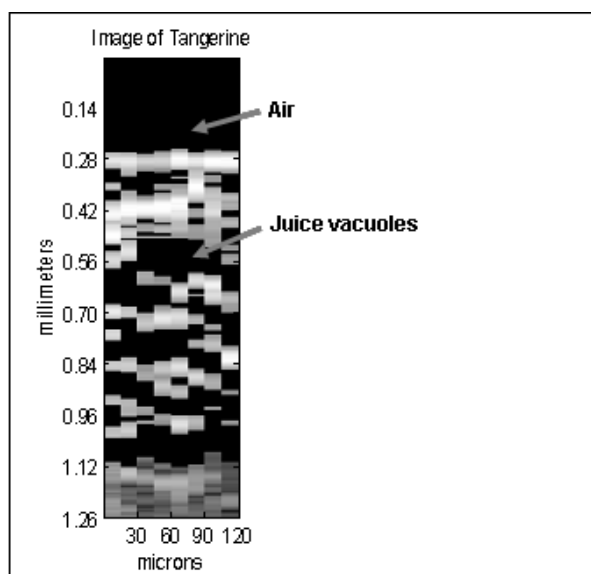


Figure 3.7. POCT image of tangerine flesh. The tangerine's juice vacuoles are clearly visible.

## Chapter 4. Volume Holographic Imaging System

### 4.1. Introductions

VHIS is based on volume holography, specifically the use of multiplexed holographic Bragg filters in optical imaging systems in combination with readout using a digital camera. This system has significant advantages over conventional optical imaging and holographic systems since it does not require scanning and can obtain both spatial and spectral information on the tissue sample.

This Chapter focuses on the imaging modality using volume holographic gratings to simultaneously obtain spatial and spectral information of biological samples without scanning.

### 4.2. Principle of Operation

A hologram is formed by superimposing a reference and an object beam, exposing a photosensitive recording material to the resultant interference pattern, and then processing the recording material. When the material is 'thick' relative to the wavelength and grating period it can be considered a volume or Bragg hologram. The diffraction efficiency  $\eta(\%)$  of a hologram is the ratio of the diffracted light relative to the incident beam intensity,

$$\eta(\%) = \frac{I_{diffraction}}{I_{incident} - I_{reflection}} \times 100\%. \quad \text{Eq. 4.1}$$

One of the characteristics of a volume hologram is that light is diffracted into one diffraction order. For a volume hologram with a phase grating the diffraction efficiency can be 100% .This makes them very useful as components in optical systems.

According to Kogelnik's coupled mode theory [39] a grating formed at one wavelength can be Bragg matched at another wavelength using a different reconstruction angle. The propagation vectors of the incident ( $\vec{k}_i$ ) and diffracted ( $\vec{k}_d$ ) beams at the Bragg condition are related by the K-vector closure relation (Eq. 4.2) and illustrated in Figure 4.1(a):

$$\vec{k}_{i,1} - \vec{k}_{d,1} = \vec{k}_{i,2} - \vec{k}_{d,2} = \vec{K}, \quad \text{Eq. 4.2}$$

where  $|\vec{k}_{i,1}| = |\vec{k}_{d,1}| = \frac{2\pi n}{\lambda}$ ,  $|\vec{k}_{i,2}| = |\vec{k}_{d,2}| = \frac{2\pi n}{\lambda + d\lambda}$ ,  $\vec{K}$  is the grating vector,  $n$  is the refractive index of the recording material, and  $\lambda$  is wavelength in free space. The relationship between the mismatch in the illumination angle ( $d\theta$ ) and wavelength ( $d\lambda$ ) is given as

$$\frac{d\theta}{d\lambda} = \frac{K}{4\pi n \sin(\alpha - \theta)}, \quad \text{Eq. 4.3}$$

where  $\alpha$  is the angle of the grating vector with respect to the normal to the recording material surface, and  $\theta$  is the reconstruction beam angle, as shown in Figure 4.1(b). The relationship in Eq. 4.3 shows that incident beams with different wavelengths can be reconstructed using their respective incident beam angles.

Volume holograms can be made to have narrowband spectral and spatial filtering properties to select very narrow angle and wavelength information from an object. The angular and wavelength selectivity are found to depend on the grating period ( $\Lambda$ ) and the thickness ( $d$ ) of the material [39]:

$$\Delta\theta \propto \frac{\Lambda}{d} \quad \text{and} \quad \Delta\lambda \propto \frac{\Lambda^2}{d}. \quad \text{Eq. 4.4}$$

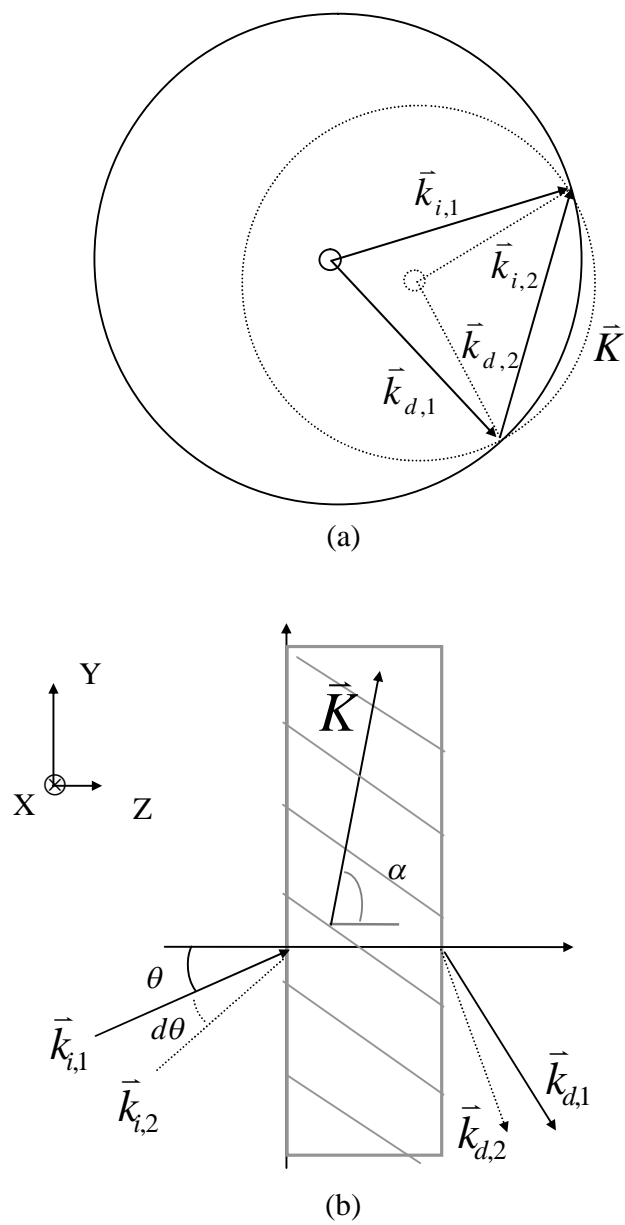


Figure 4.1. (a) Bragg circle diagram for K-vector closure. (b) Geometry for analysis of a holographic grating.

### 4.3. Holographic Construction Setup

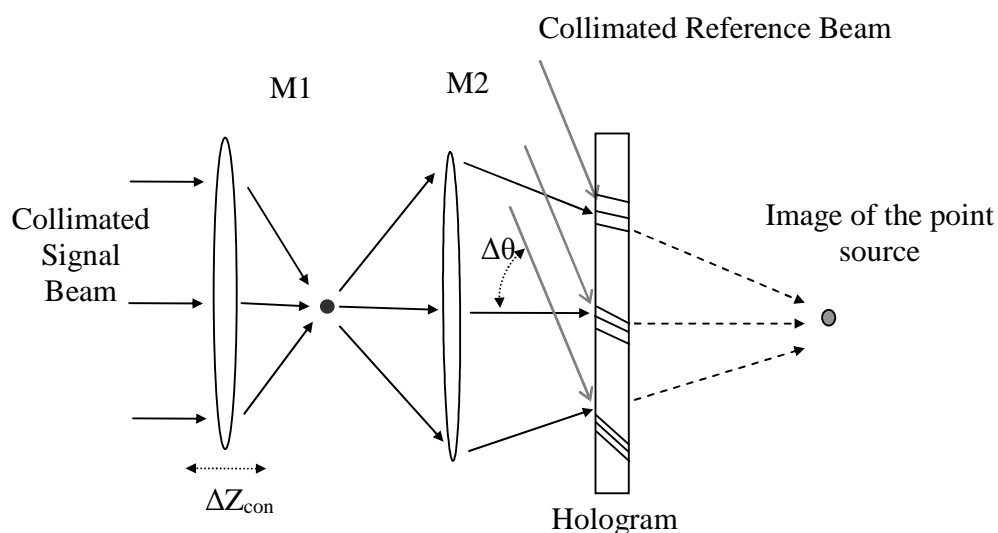


Figure 4.2. Construction setup of multiplexed gratings by using spherical and planar waves. M1 is the objective lens translated from a fixed objective lens M2. The angle of the reference beam is changed by  $\Delta\theta$  between each exposure to record a hologram.

The holographic gratings are formed as shown in Figure 4.2. A collimated laser beam is split into a reference and signal arm. Two microscope objectives are used in the signal arm to form a point source and then to adjust its position relative to the recording material. The position of the point source is controlled by moving the first microscope objective lens (M1) while holding the second microscope objective lens (M2) fixed. The angle of the reference beam is changed by  $\Delta\theta$  between each exposure to record a

hologram with a different reference beam angle for each point source location. The position of the point source is moved by  $\Delta Z_{\text{con}}$  with each exposure. The hologram exposures can be varied to increase the efficiency of gratings that select positions deeper within the tissue sample. Two relay systems shown in Figure 4.3 are used in the signal and reference arm to maintain constant irradiance at the hologram plane.

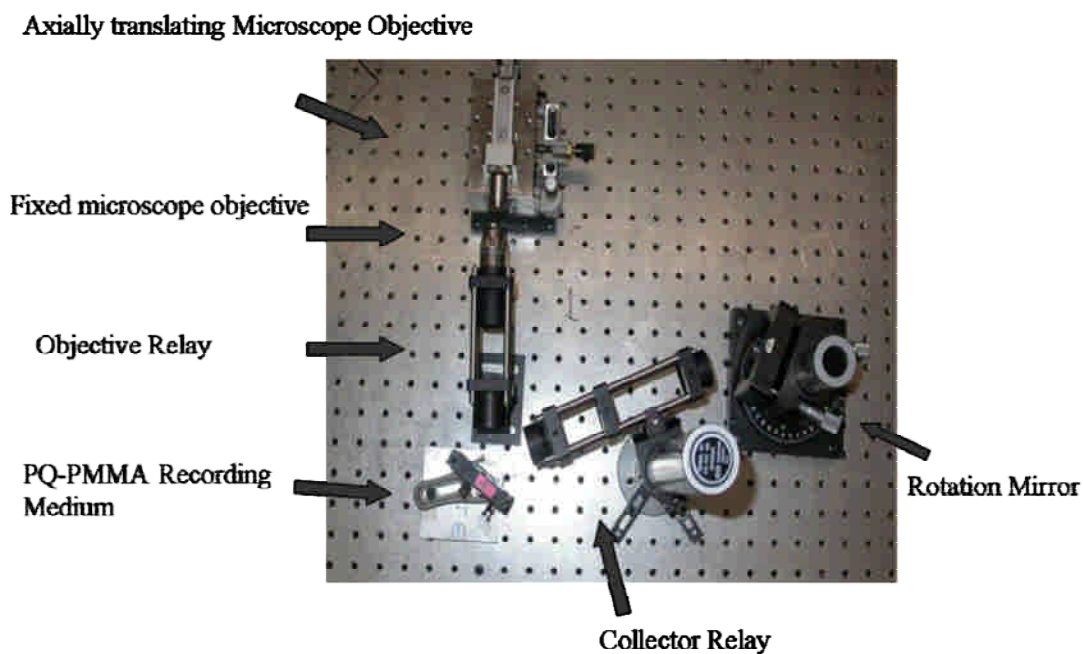


Figure 4.3. Construction setup for forming multiplexed gratings. Two relay systems (Objective Relay & Collector Relay) are used in the signal and reference arm to maintain constant irradiance at the hologram plane.

For our experiments, the recording material is approximately 1.6mm thick and is recorded using an Argon ion laser operating at a wavelength of 488nm. With fabrication as described in Chapter 6, the gratings can operate at wavelengths much longer than the recording wavelength, allowing greater imaging depths within biological tissue samples.

#### **4.4. Reconstruction Setup & Image Acquisition**

Figure 4.4 and Figure 4.5 show the experimental setup of the imaging system using a hologram with two multiplexed holographic gratings. Each multiplexed grating within the hologram is Bragg matched [40] to a different depth within the object and diffracts at a different angle. After the diffracted beams pass through the collector lens, each beam angle is projected to a different location on the camera. The Bragg selectivity of the grating operates like a confocal microscope with a slit instead of a circular pinhole [41]. The hologram is degenerate in Y, but selects only a narrow width in X when the sample is illuminated with monochromatic light. In this case, it only selects one column of the object and images it on the camera. Demonstration in Figure 4.6 shows two columns taken using an Argon laser operated at a wavelength of 488nm and a hologram with two multiplexed gratings.

Lateral (X) information about the object can be obtained when it is illuminated with a broadband source. If the gratings are nearly planar, it is possible to reconstruct the hologram with longer wavelength light than that used during construction without

significant loss in image quality. Longer wavelength light is useful since it can penetrate deeper within biological tissue samples.

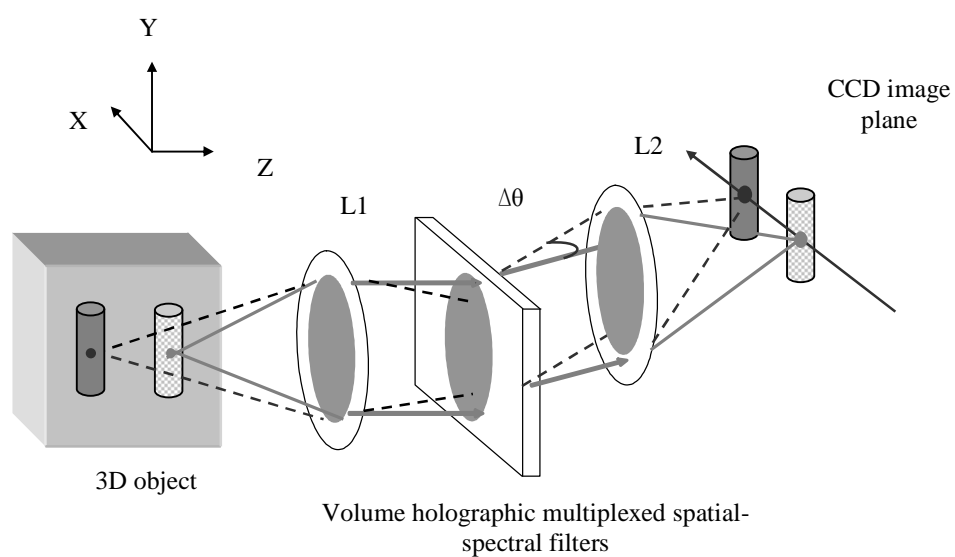


Figure 4.4. Experimental imaging setup. L1 is the objective lens, and L2 is the collector lens.

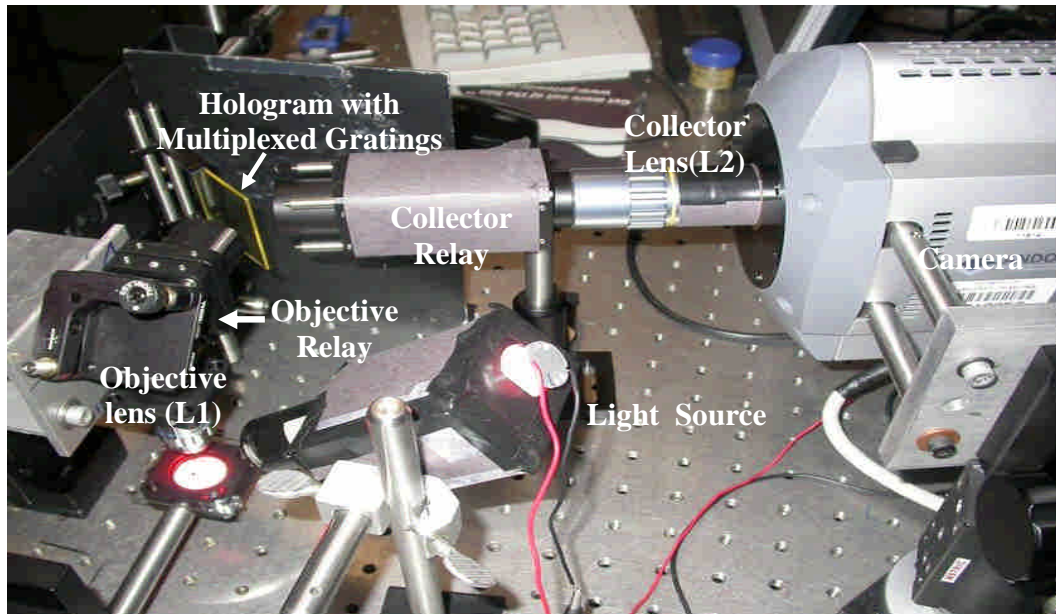


Figure 4.5. Experimental prototype of VHIS for reconstruction of multiplexed gratings using a red LED.



Figure 4.6. Raw image taken using a hologram with two multiplexed gratings, and an Argon laser operated at a wavelength of 488nm.

The system resolution along the lateral and the axial dimensions is primarily determined by the numerical aperture of the objective lens and the thickness of the holographic grating, respectively. In the experiment, the objective L1 has a numerical aperture (NA) of 0.55 ( $f_o = 3.6$  mm) when used with a grating with a thickness of 1.8 mm. The axial resolution is 12  $\mu\text{m}$  and lateral resolution of 4.5  $\mu\text{m}$  at a wavelength of 633 nm.

Increasing the objective NA or hologram thickness can further improve the resolution further [40][42].

According to the focal length of the objective lens ( $f_{objective}$ ) and the desired lateral magnification ( $M_l$ ) of the system [43][44], the collector focal length ( $f_{collector}$ ) is chosen by  $f_{collector} = f_{objective} \times M_l$ .

A Lumenera 6 Mpixel CCD array with a pixel pitch of 3.5 $\mu$ m is used for imaging in reflectance mode with a broadband source, and a highly sensitive Andor iXon array with a pixel pitch of 16  $\mu$ m is used for fluorescence mode imaging. More detailed specifications of the two CCD arrays are shown in Table 4.1. In combination with these cameras, collector focal lengths of 10mm for the Lumenera camera and 20mm for the Andor are used to resolve lateral features smaller than 15  $\mu$ m.

Both objective and collector lenses are achromatic since the system functions over a 100 nm band in the visible wavelength range of 486 - 656 nm [44]. The lenses used are commercially available microscope objectives with long working distances. The objective lens is an Olympus ULWDMSPan50X (NA = 0.55,  $f$  = 3.6 mm), and the collector lenses are Mitutuyo M Plan APO20X (NA = 0.42,  $f$  = 10.0 mm) and M Plan APO10X (NA = 0.28,  $f$  = 20.0 mm). Two telecentric objective and collector relay systems are used to increase the system's field of view, and more details of the design of the relay systems for the prototype VHIS can be found in Ref. [44].

Figure 4.7 is a raw image of an Air Force Resolution Bar Chart using a Lumenera 6 Mpixel camera and 2.8× magnification in the prototype system, and shows that lateral features as small as 4.5  $\mu\text{m}$  are well resolved. Figure 4.8 is a raw image of the bar chart using the Andor iXon camera and 5.6× magnification in the prototype system and 7.8 $\mu\text{m}$  features are well resolved. The resolution along the x axis is slightly worse than that along the y axis due to dispersion in the hologram.

Table 4.1. CCD Specifications

Vendor	Pitch Size ( $\mu\text{m}$ )	Effective Pixels	Sys. Magnification
Andor Tech.	16	512 × 512	5.6×
Lumenera Corp.	3.5	3000 × 2208	2.8×

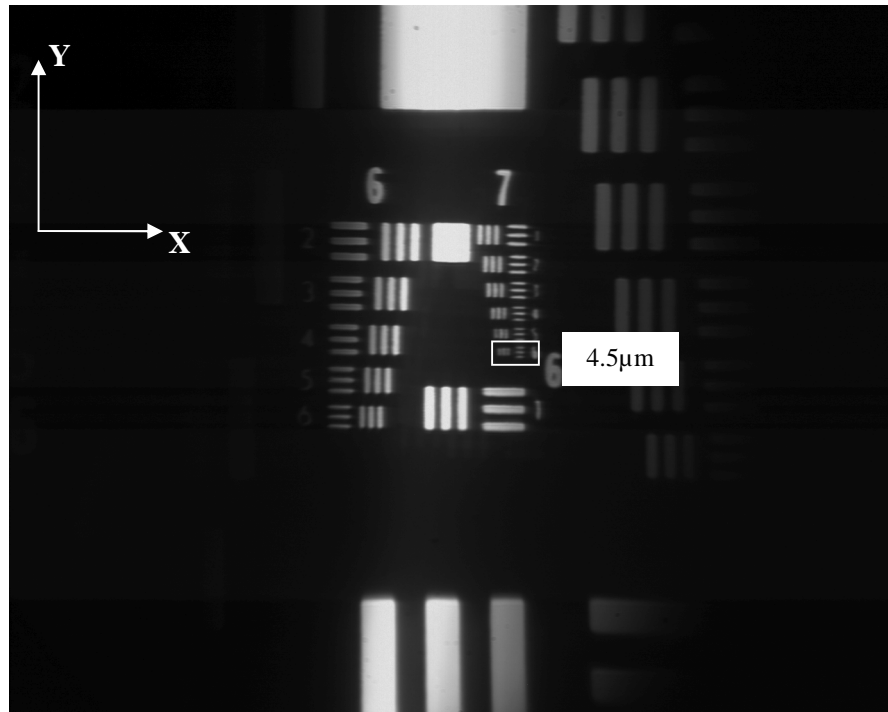


Figure 4.7. Raw image of an Air Force Resolution Bar Chart taken using a red LED, a Lumenera 6 Mpixel camera and  $2.8\times$  magnification with a single grating. Lateral features as small as  $4.5\ \mu\text{m}$  are well resolved.

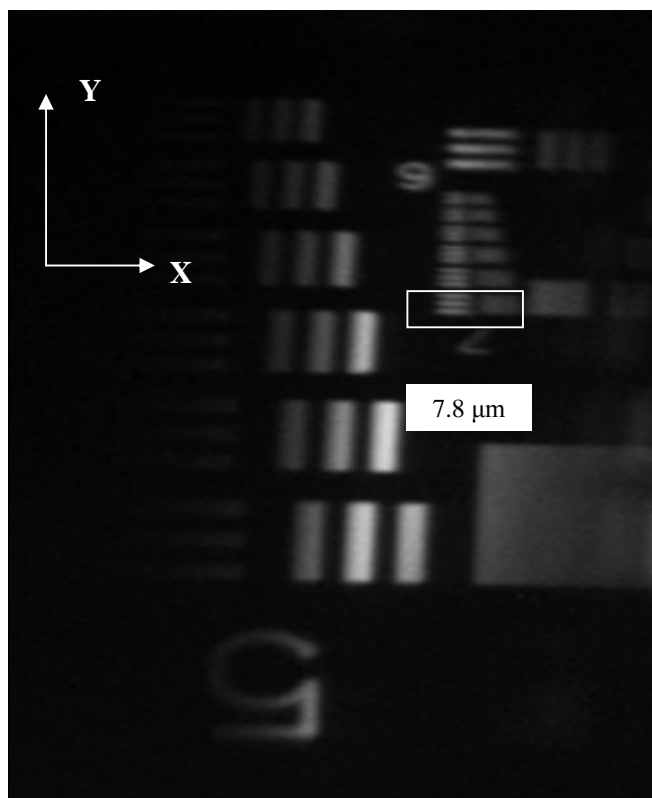


Figure 4.8. Raw images of an Air Force Resolution Bar Chart using a red LED, an Andor iXon camera and 5.6× system magnification. Lateral features as small as 7.8  $\mu\text{m}$  are well resolved.

#### 4.4.1. Non-fluorescence Images with a Red LED

The LED used was a Cree XLamp XR7090RED. The average integration time is 0.05 seconds for LED illuminated images. The beam is brought in at a glancing angle to the sample in order to prevent scattered light from being captured by the optical system. Figure 4.9 shows multiple images simultaneously displayed by using this system. The

image of an onion (*Allium Cepa*) skin was reconstructed using an Andor iXon Camera and a hologram with two multiplexed gratings with diffraction efficiencies of 49% and 42%. The onion skin was illuminated using a red LED with a peak wavelength of ~630nm and a spectral bandwidth of ~30nm. Two simultaneous depth sections of a volume sample are separated by ~75 $\mu$ m.

The image in Figure 4.10, taken using human ovary samples, shows two depth sections captured simultaneously. The left-hand section was taken just below the surface of the ovary, and the right-hand section was approximately 75  $\mu$ m deeper in the tissue. The CCD array used to obtain this image data is a Lumenera 6 Mpixel camera.

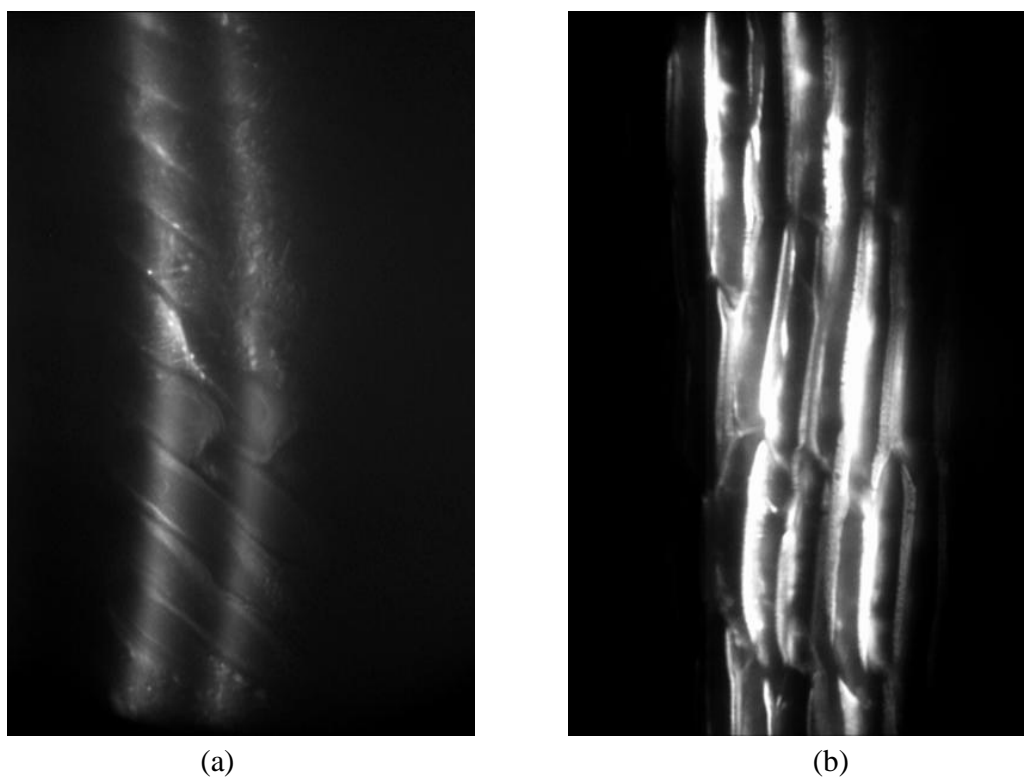


Figure 4.9. Onion skin images reconstructed by VHIS using a red LED, an Andor iXon camera and  $5.6\times$  magnification. Both images (a) and (b) show two simultaneous sections obtained at two depths within an onion skin and the depth separation between images is  $75\mu\text{m}$ .

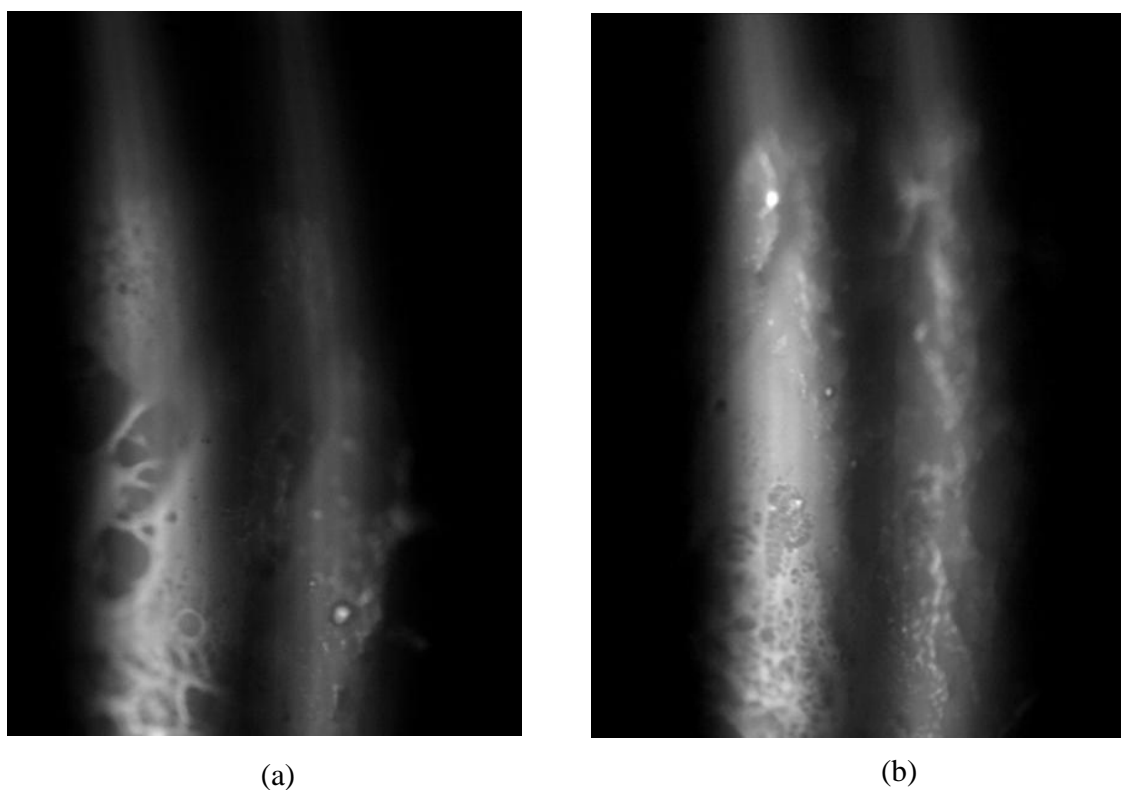


Figure 4.10. Human ovary images reconstructed by VHIS using a red LED, a Lumenera 6 Mpixel camera and  $2.8\times$  magnification. Both images (a) and (b) show two simultaneous sections of human ovary obtained at two depths with the depth separation between images of  $75\ \mu\text{m}$ .

#### 4.4.2. Fluorescence Images with a Fluorescent Dye-- Acridine Orange

This section describes the volume holographic imaging system operated in fluorescence mode. The laser induced fluorescence scheme utilizes a tripled Nd:YAG

laser source operated at 355nm with an output power of 20mW. The reconstruction setup is shown in Figure 4.11.

Figure 4.12, Figure 4.13, and Figure 4.14 show the images of mouse fat and colon tissue that had been stained with a fluorescent dye (Acridine Orange). The staining dye has a nominal central emission wavelength of 550 nm and a bandwidth of ~100 nm. The samples were illuminated using a tripled Nd:YAG laser with the wavelength of 355nm as an excitation source of the Acridine Orange, which was added to previously stained mouse tissue samples. Figure 4.12 — Figure 4.14 are the images with a field of view of ~1.46mm×1.46mm. The CCD array used to obtain this image data is an Andor iXon cooled array.

In these images the bandwidth of the fluorophore emission spectra is very wide (~100nm) and causes overlap between projections from different depths. However this condition can be corrected by designing the holograms to have larger angular separation between each reference beam. A narrow-band spectral filter could also be used to reduce the fluorescence spectrum and thus the lateral extent (X) of the sections, so that more sections could be projected in the limited space of the CCD camera.

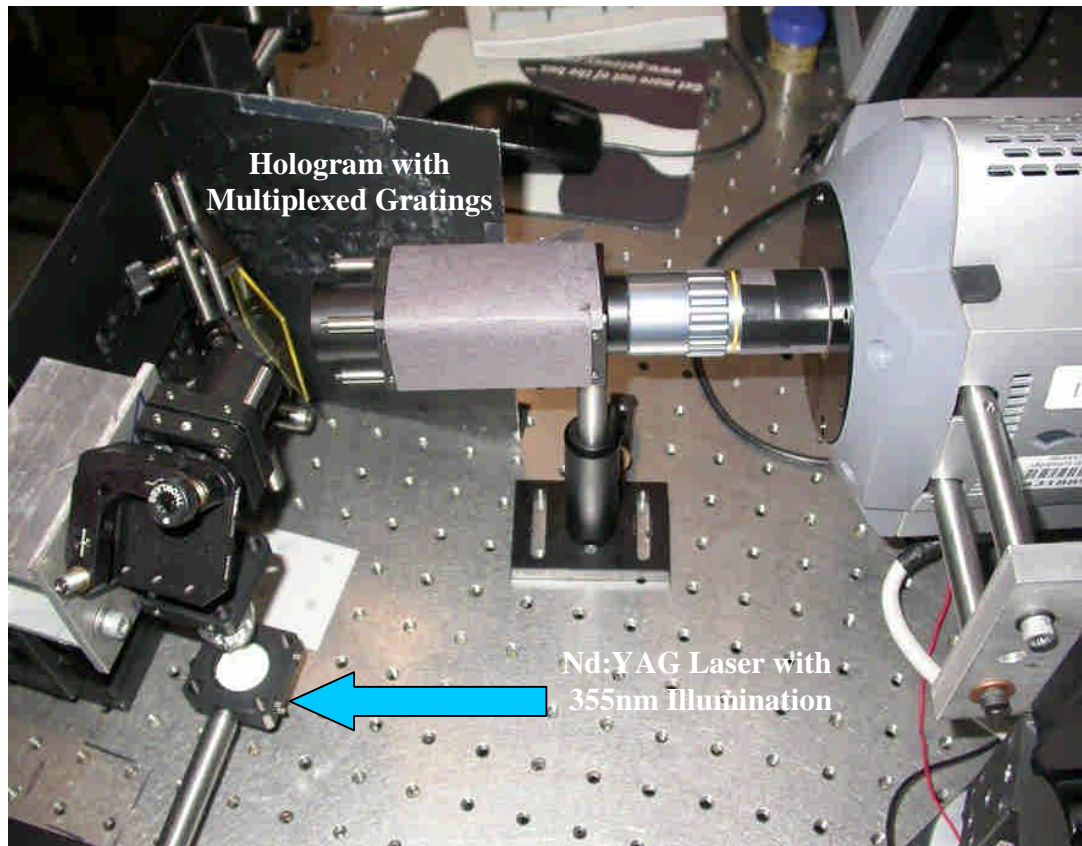


Figure 4.11. Experimental prototype for reconstruction using a tripled Nd:YAG laser as an excitation source.

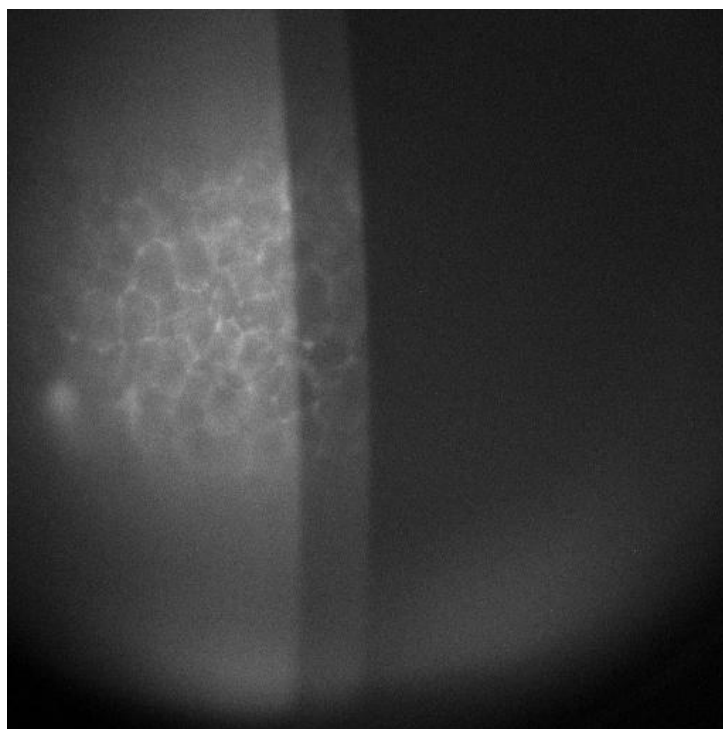


Figure 4.12. Fluorescence images of mouse fat stained with Acridine Orange. The figure was obtained with the VHIS system using a Nd:YAG excitation source, 5.6× magnification, an Andor iXon camera and a two grating hologram with an 10 angle between the reference beams.

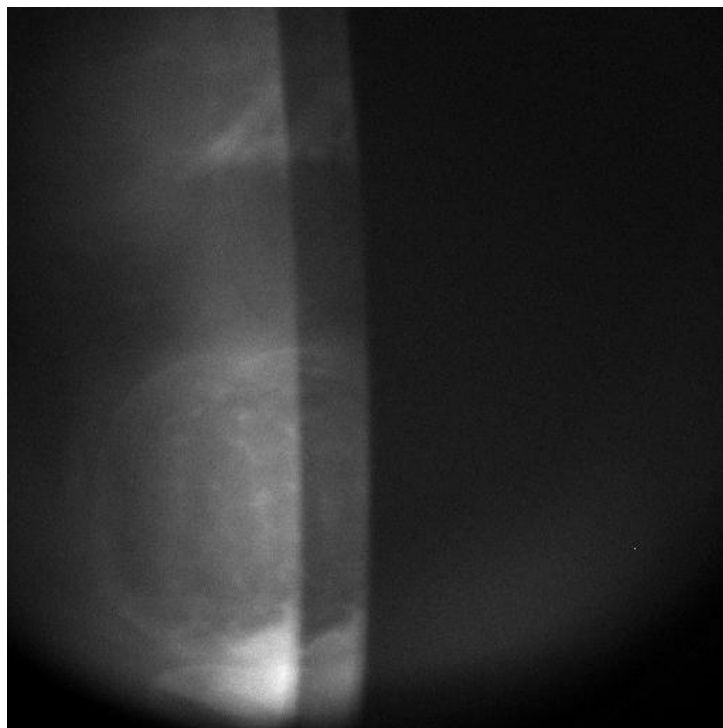


Figure 4.13. Fluorescence images of mouse ovary stained with Acridine Orange. The figure was obtained with the VHIS system using a Nd:YAG excitation source, 5.6 $\times$  magnification, an Andor iXon camera and a two grating hologram with an 10 angle between the reference beams.

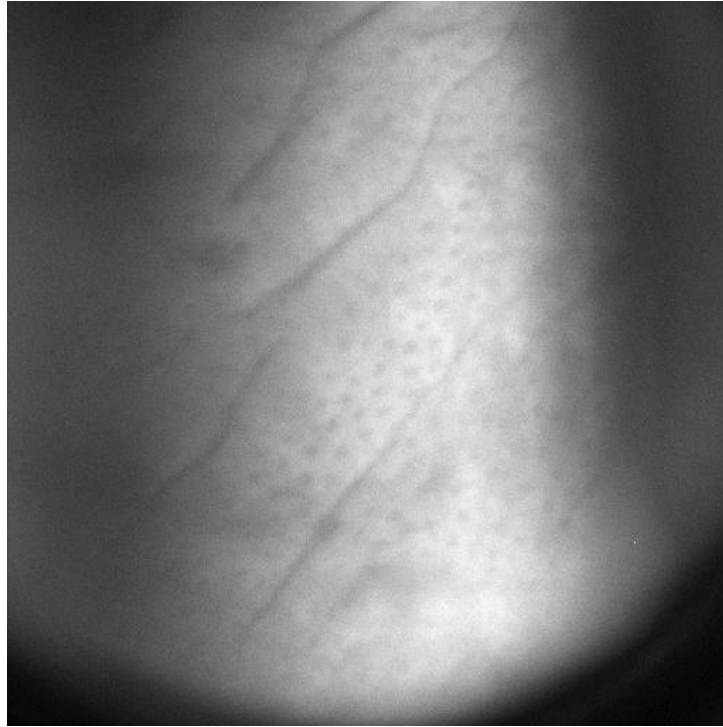


Figure 4.14. Fluorescence images of mouse colon stained with Acridine Orange. The figure was obtained with the VHIS system using a Nd:YAG excitation source, 5.6 $\times$  magnification, an Andor iXon camera and a two grating hologram with an 1 $\circ$  angle between the reference beams.

#### **4.4.3. Imaging Experiment with 0.5% Intralipid Solution**

The Air Force Resolution Bar Chart was immersed in a tank of a diluted Intralipid solution. The depth to which the target can be translated from the tissue surface position and still be visible will be considered the imaging depth.

Most types of tissue can be modeled using a 2% Intralipid solution since the scattering and absorption properties of the Intralipid are similar to natural tissue [44][45][46]. However, since a 2 % solution is very highly scattering, it is difficult to have the bar chart even with the surface of the solution without problems caused by surface tension. Therefore, the solution must be diluted to a concentration of 0.5 % in order to allow the target to be viewed a few hundred microns below the surface and to avoid surface tension problem. The measured depth in the 0.5% solution can be calculated using Beer's law:

$$I(d) = I_{inc} \exp[-(\mu'_{scattering} + \mu_{absorption})d], \quad \text{Eq. 4.5}$$

where  $d$  is the depth of a point source inside the media, and  $\mu'_{scattering}$  and  $\mu_{absorption}$  are the reduced scattering coefficient and absorption coefficient, respectively. Since absorption can be ignored [44][45], the relationship between  $d_{0.5\%}$  and  $d_{2\%}$  is shown by:

$$d_{2\%} = d_{0.5\%} \times \left( \frac{\mu'_{scattering,0.5\%}}{\mu'_{scattering,2\%}} \right), \quad \text{Eq. 4.6}$$

$$\mu'_{scattering,0.5\%} \cong \frac{\mu'_{scattering,2\%}}{4} \Rightarrow d_{2\%} \cong 4 \times d_{0.5\%}. \quad \text{Eq. 4.7}$$

Figure 4.15 shows the images obtained by the VHIS with a single grating at the depths of 300 and 600 $\mu\text{m}$  in the 0.5% Intralipid solution. In our experiment, we are able to obtain a depth of 800 $\mu\text{m}$  in the 0.5% solution using Element 2 of Group 6 with a feature size of 13.9 $\mu\text{m}$  on the bar chart. According to Eq. (3), a depth of 800 $\mu\text{m}$  in the 0.5% solution is equivalent to 200 $\mu\text{m}$  in the 2% solution.

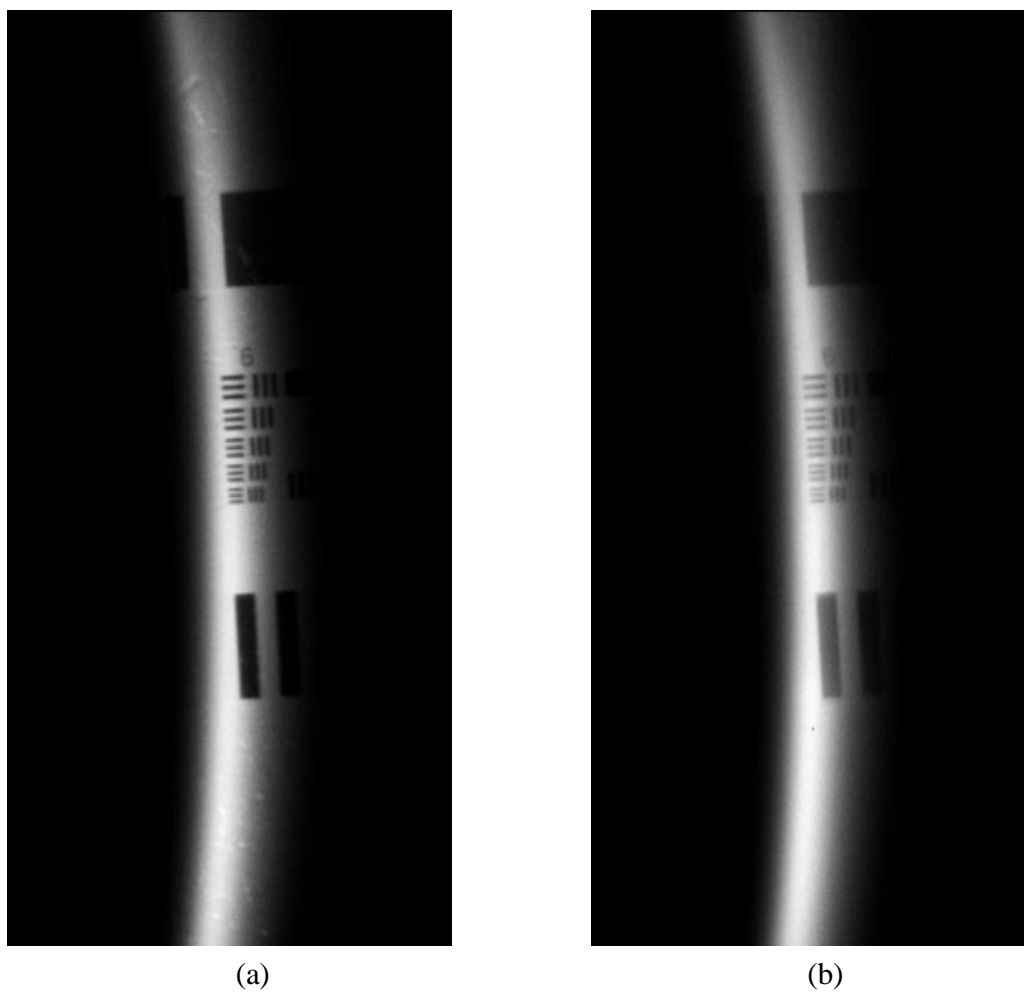


Figure 4.15. Images of the Air Force Resolution Bar Chart taken with the VHIS system using a red LED ( $\lambda_{\text{central}}=633\text{nm}$ ,  $\Delta\lambda\sim 30\text{nm}$ ),  $5.6\times$  magnification, and an Andor iXon camera. Figure (a) shows the Bar Chart image of Group 6 at a depth of  $300\mu\text{m}$  in a 0.5% Intralipid solution. The figure on the right shows the Bar Chart image of Group 6 at a depth of  $600\mu\text{m}$  in the 0.5% solution

## Chapter 5. Modeling for Curved Holographic Gratings

### 5.1. Introduction

Holographic gratings formed with spherical waves are of wide interest owing to their many applications such as in optical information storage technology [40][47] and optical imaging systems [11][42][48][49]. An accurate model of hologram performance is necessary to optimize their design and fabrication with different construction parameters. The coupled wave approach [39] and rigorous coupled wave analysis (RCWA) [50][51] have been used extensively to model diffraction of gratings. However, these two common analyzing methods are restricted to the case of planar gratings and uniform grating vectors across the entire hologram.

Since the formation of spherical wave gratings results in a curved grating, coupled wave analysis of the diffraction efficiency is more complicated than planar gratings. Several attempts have been made to analytically evaluate spherical wave gratings. Syms and Solymar [52] demonstrated treating a grating as localized planar grating sections that vary in orientation across the hologram, but their calculations do not account for the polarization of the reconstruction beam and ignore the effects of higher order. Barbastathis et al [42] obtained analytical solutions for the angular selectivity of spherical wave gratings based on Born's approximation, which depends on a weak index modulation assumption. Their analytical expression is valid only for a small angle between signal and reference arms [43].

In this Chapter, a comprehensive method is developed to model the angular selectivity, depth selectivity, and diffraction efficiency of curved gratings. In this model, a curved grating will be analyzed in RCWA based on Syms' method [52] by considering locally planar gratings. The RCWA technique is used to consider the abrupt grating interface, permitting conical incidence, and arbitrary polarization of the different fields involved in the diffraction process of any thickness hologram.

This model can be extended for multiplexed curved gratings and used to theoretically predict the performance of multiplexed spherical wave gratings on a hologram. The results obtained with this model are compared with measurements of the diffraction efficiency, depth separation, and angular and depth selectivity of multiplexed curved gratings in PQ-doped PMMA photopolymer, and it is demonstrated that the prediction agree well with the experimental results.

## 5.2. Rigorous Coupled Wave Analysis

RCWA possesses many advantages in predicting the performance of a planar grating. The three-dimensional reconstruction geometry for a slanted planar grating is shown in Fig. 1. RCWA can compute diffraction efficiency for any incident beam angle with an arbitrary polarization state. It can model conical diffraction with grating vector  $\vec{K}$ , lying outside the reconstruction plane. It can account for an arbitrary number of transmission and reflection orders for a hologram with thickness of  $d$ . In Figure 5.1, a polarized electromagnetic wave is incident at an angle  $\alpha$ . The polarization of the incident beam is

given by  $\psi$ , which is the angle of the E field component with respect to the TM component. The angles of the rotation of  $\vec{K}$  with respect to the y and z axes are  $\beta$  and  $\Phi$ , respectively.

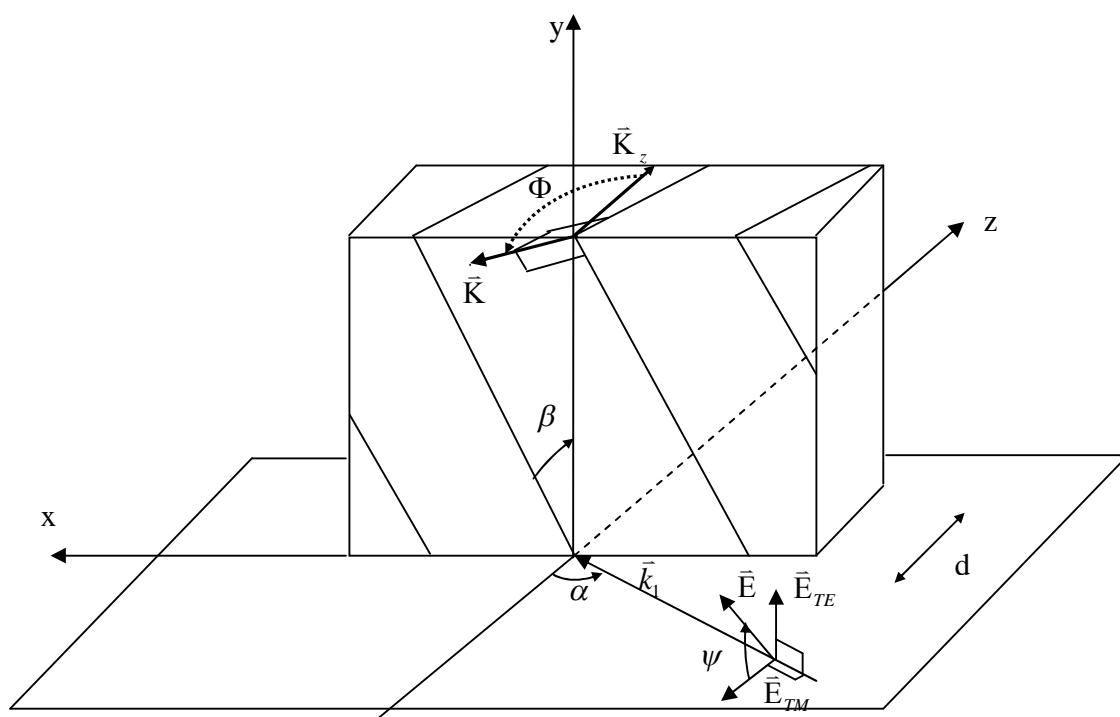


Figure 5.1. Reconstruction geometry of a single slanted planar grating with a planar wave of propagation vector  $\vec{k}_1$  incident with an arbitrary angle and polarization.

We assume the reconstruction beam is in the x-z plane. The grating vector is given by

$$\vec{K} = (K \sin \Phi \cos \beta) \hat{x} - (K \sin \Phi \sin \beta) \hat{y} + (K \cos \Phi) \hat{z}, \quad \text{Eq. 5.1}$$

where  $K = 2\pi/\Lambda$  and  $\Lambda$  is the grating period. There are three defined regions: Region 1 is the incident medium, region 2 is the recording medium where a grating is present, and region 3 is the substrate. The amplitude of the propagation vector in the  $\ell$  th region  $k_\ell$  is equal to  $k\sqrt{\varepsilon_\ell}$ , where  $\varepsilon_\ell$  is the relative permittivity in region  $\ell$ ,  $k = 2\pi/\lambda$ , and  $\lambda$  is the free-space wavelength. In the incident medium, the incident normalized electric-field vector is

$$\vec{E}_{inc} = \hat{u} \exp(-j\vec{k}_1 \cdot \vec{r}), \quad \text{Eq. 5.2}$$

where  $j = \sqrt{-1}$ ,  $\vec{k}_1 = k_1(\sin \alpha) \hat{x} + k_1(\cos \alpha) \hat{y}$ ,  $\vec{r} = x\hat{x} + y\hat{y} + z\hat{z}$ , and  $\hat{u}$  is the polarization unit vector given by

$$\hat{u} = (\cos \psi \cos \alpha) \hat{x} + (\sin \psi) \hat{y} - (\cos \psi \sin \alpha) \hat{z}. \quad \text{Eq. 5.3}$$

The normalized total electric fields in regions 1 and 3 are given by

$$\vec{E}_1 = \vec{E}_{inc} + \sum_n \vec{R}_n \exp(-j\vec{k}_{1n} \cdot \vec{r}), \quad \text{Eq. 5.4}$$

and

$$\vec{E}_3 = \sum_n \vec{T}_n \exp(-j\vec{k}_{3n} \cdot (\vec{r} - d\hat{z})), \quad \text{Eq. 5.5}$$

where  $\bar{R}_n$  is the normalized vector electric fields of the  $n$ th reflected diffracted order in region 1 with propagation vector  $\bar{k}_{1n}$ , and  $\bar{T}_n$  is the normalized vector electric fields of the  $n$ th transmitted diffracted order in region 3 with propagation vector  $\bar{k}_{3n}$ . According to the phase matching condition,  $\bar{k}_{\ell n}$  in region 1 and 3 can be expressed as

$$\begin{aligned}\bar{k}_{\ell n} &= k_{xn}\hat{x} + k_{yn}\hat{y} + k_{z\ell n}\hat{z} \\ &= [(\bar{k}_1 - n\bar{K}) \bullet \hat{x}]\hat{x} + [(\bar{k}_1 - n\bar{K}) \bullet \hat{y}]\hat{y} + k_{z\ell n}\hat{z},\end{aligned}\quad \text{Eq. 5.6}$$

where  $k_{xn} = k_1 \sin \alpha - nK \sin \Phi \cos \beta$ ,  $k_{yn} = nK \sin \Phi \sin \beta$ , and  $k_{z\ell n} = \sqrt{k_\ell^2 - k_{xn}^2 - k_{yn}^2}$ .

The signs of the propagation vector in the  $z$  direction,  $k_{z1n}$  and  $k_{z3n}$ , must be chosen carefully. For the condition of a reflected propagating wave,  $k_{z1n}$  is negative real; for the condition of an evanescent wave,  $k_{z1n}$  is positive imaginary. However, for the condition of a transmitted propagating wave,  $k_{z3n}$  is positive real; for the condition of an evanescent wave,  $k_{z3n}$  is negative imaginary.

The electric and magnetic fields in recording medium region can be expressed as:

$$\bar{E}_2 = \sum_n [S_{xn}(z)\hat{x} + S_{yn}(z)\hat{y} + S_{zn}(z)\hat{z}] \exp(-j\bar{\sigma}_n \bullet \hat{r}), \quad \text{Eq. 5.7}$$

and

$$\bar{H}_2 = (\epsilon_0/\mu_0) \sum_n [U_{xn}(z)\hat{x} + U_{yn}(z)\hat{y} + U_{zn}(z)\hat{z}] \exp(-j\bar{\sigma}_n \bullet \hat{r}), \quad \text{Eq. 5.8}$$

where  $\varepsilon_0$  is the permittivity of free space,  $\mu_0$  is the permeability of free space, and  $\vec{\sigma}_n = k_{xn}\hat{x} + k_{yn}\hat{y} - nK_z\hat{z}$ .  $S_n$  and  $U_n$  are the amplitudes of the  $n$ th space-harmonic of the electric and magnetic fields so that  $E_2$  and  $H_2$  satisfy Maxwell's equations in region 2:

$$\nabla \times \vec{E}_2 = -j\omega\mu_0, \quad \text{Eq. 5.9}$$

and

$$\nabla \times \vec{H}_2 = j\omega\varepsilon_0\varepsilon(x, y, z)\vec{E}_2, \quad \text{Eq. 5.10}$$

where  $\omega$  is the angular frequency of the incident radiation, and  $\varepsilon(x, y, z)$  is the periodic complex relative permittivity in the grating region (region 2). The method of solving  $S_n$  and  $U_n$  is to substitute Eq. 5.7 and Eq. 5.8 into the two Maxwell equations (Eq. 5.9 and Eq. 5.10). The components of  $\vec{E}_2$  and  $\vec{H}_2$  that are not parallel to the boundary are eliminated, and four coupled differential equations are solved. The general solution is obtained using numerical methods, and the amplitudes of diffracted fields are calculated by matching the boundary conditions at each boundary of region 2. Then, the diffraction efficiency of diffracted orders can be calculated. The detail is in Ref.[50].

### 5.3. Simulation Procedure for a Single Curved Grating

A grating formed by spherical waves will be curved and non-uniform within a hologram. However, the curvature can be considered as locally planar uniform sections that vary in orientation across the hologram aperture as shown in Figure 5.2. In the

locally planar section, the grating can be considered formed by two planar waves, and then RCWA can be used to calculate the diffraction efficiency for each planar section.

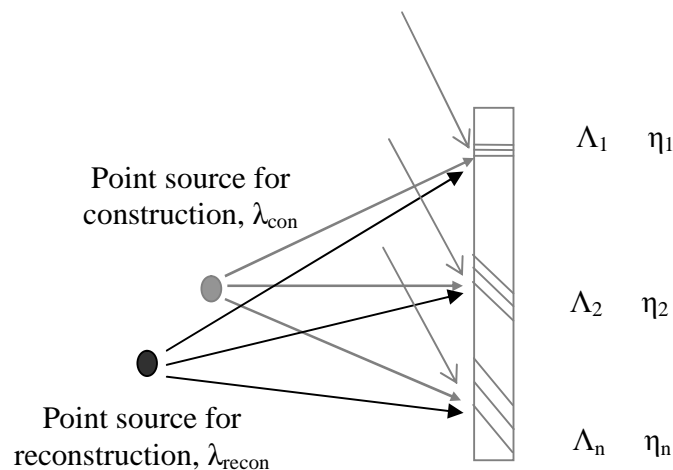


Figure 5.2. Construction and reconstruction stages of a curved grating.

The procedure used to analyze a curved grating may be broken down into five steps:

- 1) The hologram aperture is sampled with a large number of sampling zones,  $N$ , in order to make each zone small comparatively to the aperture size and the thickness of the hologram.
- 2) Within each sampling zone of the hologram, the grating is considered to be formed with two planar waves.
- 3) The resulting grating vector is then computed within each sampling zone.
- 4) The effects of physical changes, such as thickness variation, polarization change, and a different wavelength for reconstruction, on the properties of the grating within each zone are considered.
- 5) RCWA is used locally to calculate the diffraction efficiency ( $\eta_i$ ) of the diffracted beam from each sampling zone. Although

RCWA can be used to model an arbitrary number of diffracted orders, only the first order of the diffracted beam is considered to compare to the experimental results. The total diffraction efficiency of the curved grating across the hologram aperture is then given by

$$\eta_{total} = \left( \sum_i^N \eta_i^2 \right) / N . \text{ Eq. 5.11}$$

#### 5.4. Simulation Procedure for Multiplexed Curved Grating

The procedure can also be extended for multiplexed curved gratings. A schematic diagram of the setup for making a multiplexed curved grating is shown in Figure 5.3. The gratings are multiplexed by moving the construction point source with  $\Delta Z_{con}$  and adjusting the reference beam angle with  $\Delta\theta$  for each exposure. Each multiplexed grating can be considered independent within a hologram if the angular difference ( $\Delta\theta$ ) between reference beams angles is greater than the angular selectivity of each grating. To simplify the calculation, the objective lens in the signal arm is assumed to be a paraxial lens in Figure 5.3, indicating that the lens is aberration-free.

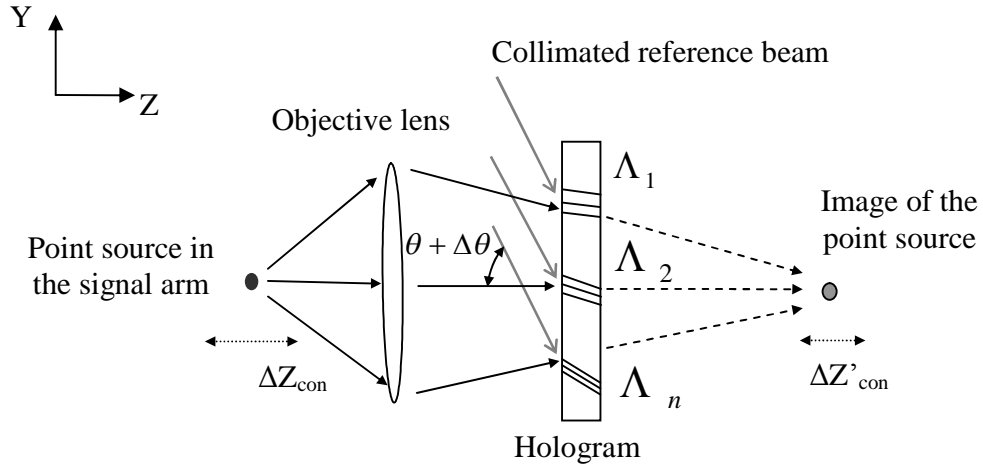


Figure 5.3. Setup of multiplexed curved gratings.

To analyze multiplexed curved gratings within a hologram as in Figure 5.3, the procedure may be broken down into the following steps. 1) The image position of the point source is generated with the paraxial imaging equation,  $\frac{1}{z'} = \frac{1}{z} + \frac{1}{f}$ , where  $z$  and  $z'$  are Gaussian distances and  $f$  is the focal length of the objective lens. 2) The spherical wave in the signal arm is decomposed into planar waves, each of which interferes with the planar reference wave in the individual sampling zone of the hologram, and then the resulting grating vector is computed. 3) The effects of the changes due to different wavelength, thickness variation, and polarization change on the properties of the grating are considered, and the new grating vector is determined. 4) RCWA theory is used locally to determine the performance of the individual grating in each sampling zone. 5) The  $\eta_{total}$  is calculated for a given reconstruction point source by Eq. 5.9. 6) For another multiplexed grating, this procedure is repeated, moving the constructed point source by

$\Delta Z_{\text{con}}$  and the reference beam angle by  $\Delta\theta$ . In our case, since the angular difference ( $\Delta\theta$ ) between reference beams angles is much greater than the full width of half maximum (FWHM) of angular selectivity for each grating, the multiplexed grating can be considered independent within a hologram.

## **5.5. Experimental Measurements**

### **5.5.1. Experimental Setup**

A multiplexed hologram is formed by superimposing interferometric exposures in the same volume on PQ-doped PMMA recording material. The experimental setup shown in Figure 5.4 is the same as in Section 4.3. The material is recorded with the set up using an Argon Ion Laser operating at a wavelength of 488nm. The reference beam is a planar wave and the positions of the point source in the signal arm are controlled by moving the first microscope objective lens (M1) with numerical aperture (NA) of 0.65 along the axial direction. A second microscope objective lens (M2) with 0.55NA remains in a fixed position in the signal arm, forming the point source. The nominal angle between the two arms is  $\sim 68^\circ$  and is changed by  $\Delta\theta$  with each exposure to record a hologram with a different reference beam angle and point source location. The position of the point sources is moved by  $\Delta Z_{\text{con}}$  with each exposure.

A relay system is used in each arm to maintain constant irradiance at the hologram plane with moving the M2 lens in signal arm and rotated mirror in reference arm. The angle settings, point source locations, and exposure time settings are automated using a

LabView control system. The hologram exposures are varied to change the efficiency of the gratings within the hologram. In the experiments,  $\Delta\theta$  was set at  $\sim 1^\circ$  to avoid crosstalk during the reconstruction process.

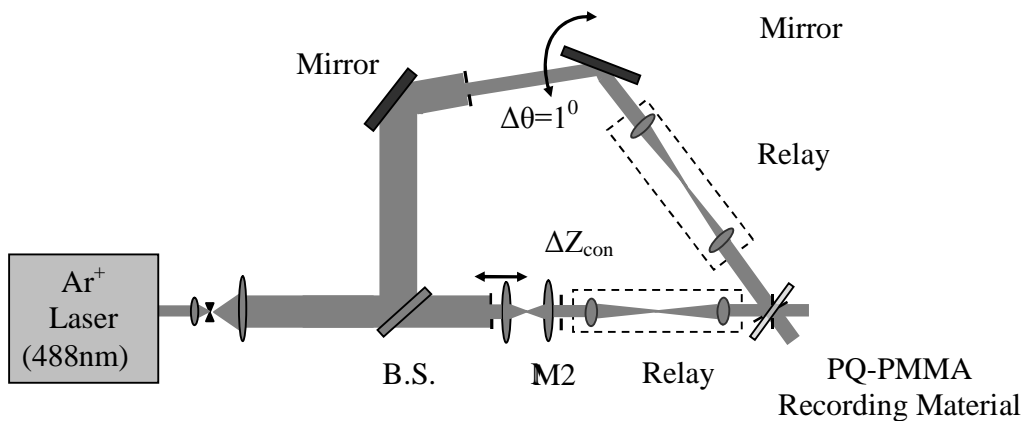


Figure 5.4. Construction setup of the angle multiplexed holographic filters.

### 5.5.2. Selectivity and Depth Separation Measurements

To quantitatively analyze the characteristics of curved gratings multiplexed within a hologram, two different wavelengths of 488nm and 633nm with TE polarized light were used for reconstruction in experiments to compare with the simulation results. A schematic diagram of the experimental setup is shown in Figure 5.5. The arrangement is able to measure depth separation, angular selectivity, diffraction efficiency, and depth selectivity. The intensities of diffracted beams were obtained by moving the first microscope objective lens (M1) by  $\Delta Z_{\text{recon}}$ . The diffraction efficiency was determined by using the relation:

$$\eta(\%) = [P_{diff} / (P_{inc} - P_{ref})] \times 100\% , \quad \text{Eq. 5.12}$$

where  $P_{inc}$  is the power of the incident beam, and  $P_{ref}$  is the power of the reflection beam from the hologram.  $P_{diff}$  represents the power of the diffracted beam. In Figure 5.5, the NAs of M1 and M2 are 0.65 and 0.55, respectively.

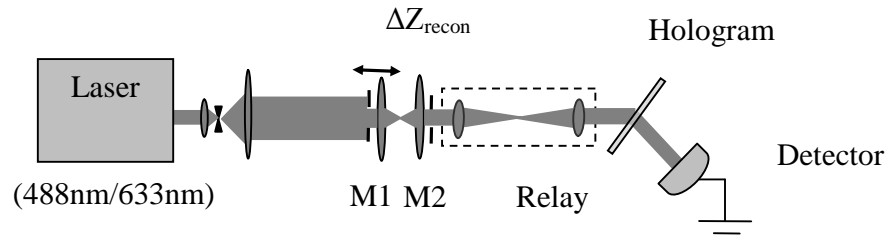
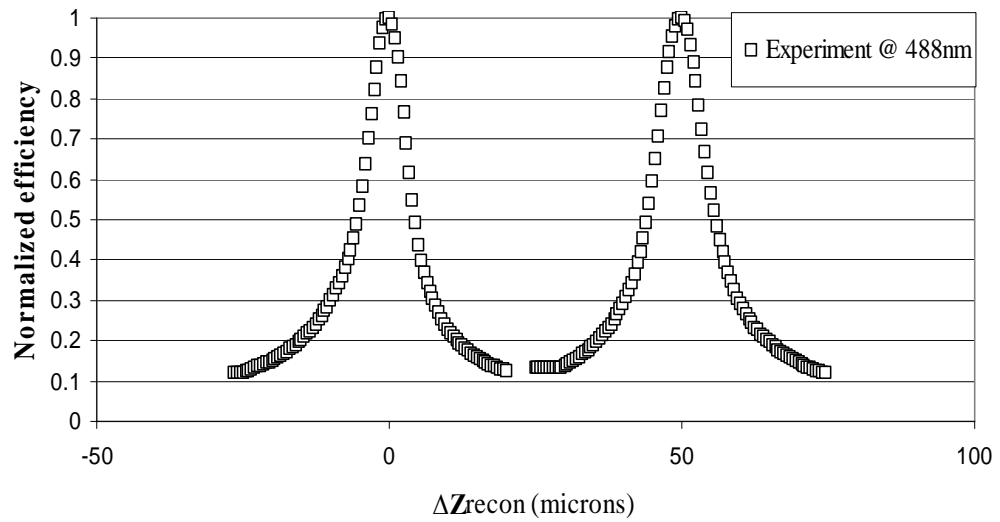


Figure 5.5. Experimental setup for depth separation, diffraction efficiency, and selectivity measurements.

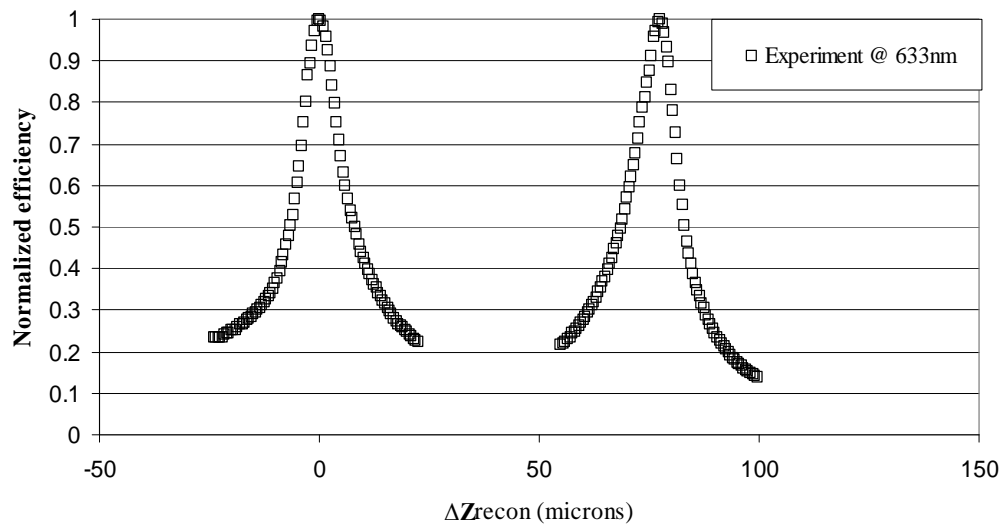
Measurements of the depth selectivity were made, and are plotted in Figure 5.6. Figure 5.6(a) shows experimental results of the point spread function in depth ( $PSF_z$ ) at reconstruction wavelength of 488nm. Figure 5.6(b) shows experimental results of the  $PSF_z$  at the reconstruction wavelength of 633nm. Experimental results for the relationship between  $\Delta Z_{con}$  and  $\Delta Z_{recon}$  are plotted in Figure 5.7. In addition, the experimental data of peak diffraction efficiency ( $\eta$ ) and angular selectivity ( $\Delta\theta_s$ ) of a hologram with two multiplexed gratings are listed in Table 5.1

Table 5.1. Max.  $\eta$  and angular selectivity ( $\Delta\theta_s$ ) of a hologram with two multiplexed gratings.

		1 <sup>st</sup> grating	2 <sup>nd</sup> grating
488nm	$\eta_{\max}$	39%	32%
	$\Delta\theta_s$	0.03°	0.03°
633nm	$\eta_{\max}$	19%	17%
	$\Delta\theta_s$	0.037°	0.045°

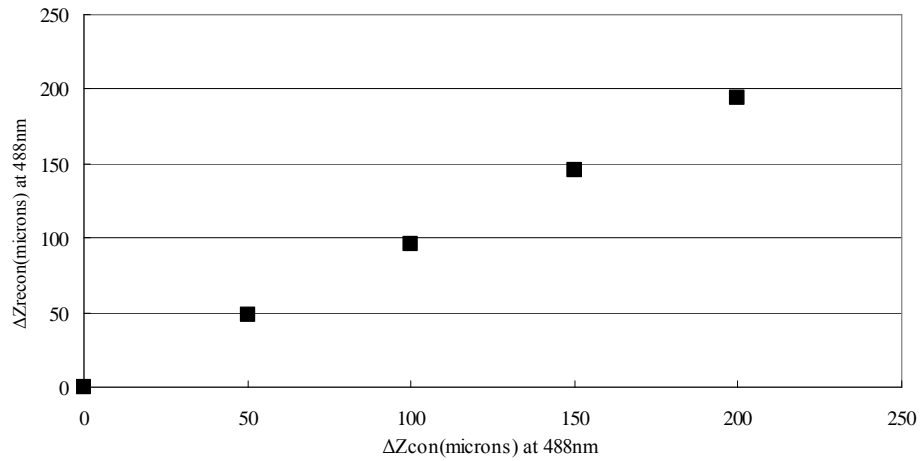


(a)

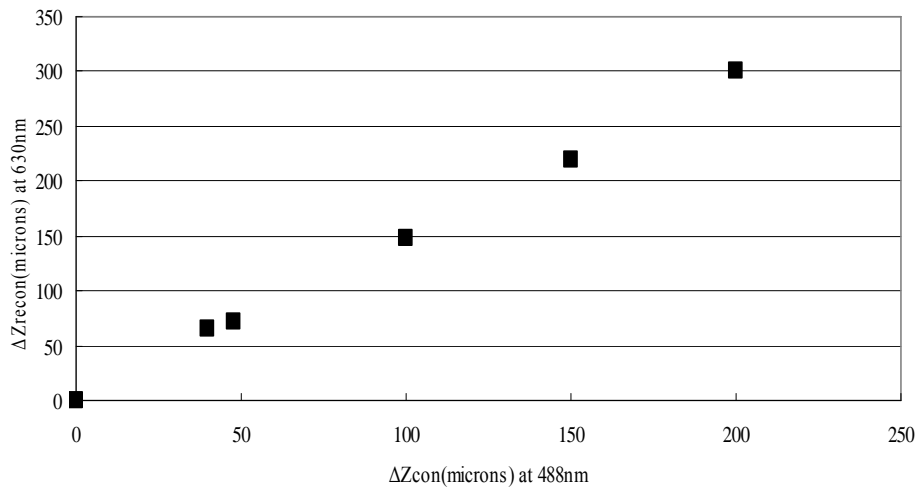


(b)

Figure 5.6.(a) Experimental results of the depth selectivity for the hologram of two gratings at 488nm. (b) Experimental results of the depth selectivity for the hologram of two gratings at 633nm.



(a)



(b)

Figure 5.7. Experimental results of the relationship between  $\Delta Z_{con}$  and  $\Delta Z_{recon}$  (a) at the same wavelength of 488nm for both construction and reconstruction. (b) at the wavelength of 488nm for construction and 633nm for reconstruction.

## 5.6. Simulation Results

To compare with the experimental results, the sample thickness was set to be 1.5mm ( $d=1.5\text{mm}$ ) in the numerical analysis. According to the method outlined in Section 5.4, a point source in the signal was set at the front focal point of the lens to form the first grating in the simulation. The second grating was formed by moving the point source away from the lens by  $50\mu\text{m}$ ,  $\Delta Z_{\text{con}}=50\mu\text{m}$ . Across the hologram plane along the  $y$  axis, sampling points were 1000 points to have a convergence result for the diffraction efficiency. For other simulation parameters, the polarization angle was  $90^\circ$  (TE polarization), the absorption coefficient was  $0.045(1/\text{mm})$  at  $488\text{nm}$  and  $0.039(1/\text{mm})$  at  $633\text{nm}$ , the index modulation was  $0.00008$  for the first grating and  $0.00007$  for the second grating, the refractive index was  $1.49$ , and the focal length of the objective lens was  $3.6\text{mm}$ . The nominal angle between two beams was  $68^\circ$  and was changed by  $1^\circ$  ( $\Delta\theta=1^\circ$ ) with each exposure to record a hologram with a different reference beam angle.

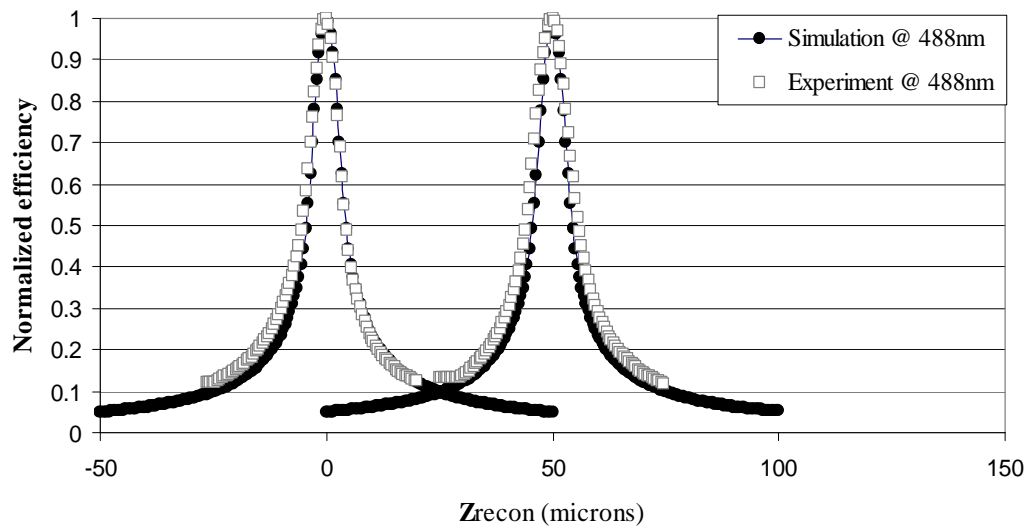
To simulate the angular selectivity of the curved gratings, the angular step of the reconstruction beam was set at  $0.0002^\circ$  which must be much smaller than the FWHM of angular selectivity in order to provide enough data and compare with the measurements. The simulation results are listed in Table 5.2. For the depth selectivity of the grating, the depth step for moving the reconstruction point source was made  $0.5\mu\text{m}$  along the  $z$  axis. Figure 5.8(a) shows the simulation results of the point spread function in depth ( $\text{PSF}_z$ ) at the reconstruction wavelength of  $488\text{nm}$ , and the average full width of half maximum (FWHM) is  $\sim 9\mu\text{m}$ . Figure 5.8(b) shows the results of the  $\text{PSF}_z$  at the reconstruction

wavelength of 633nm, and the average FWHM is  $\sim 12\mu\text{m}$ . According to Table 5.2, the peak diffraction efficiency between simulation and measurements at 633nm is slight different. This causes the increase of mismatch close to the tail of the curves between the simulation and experimental results shown in Figure 5.8(b) after the diffraction efficiency is normalized.

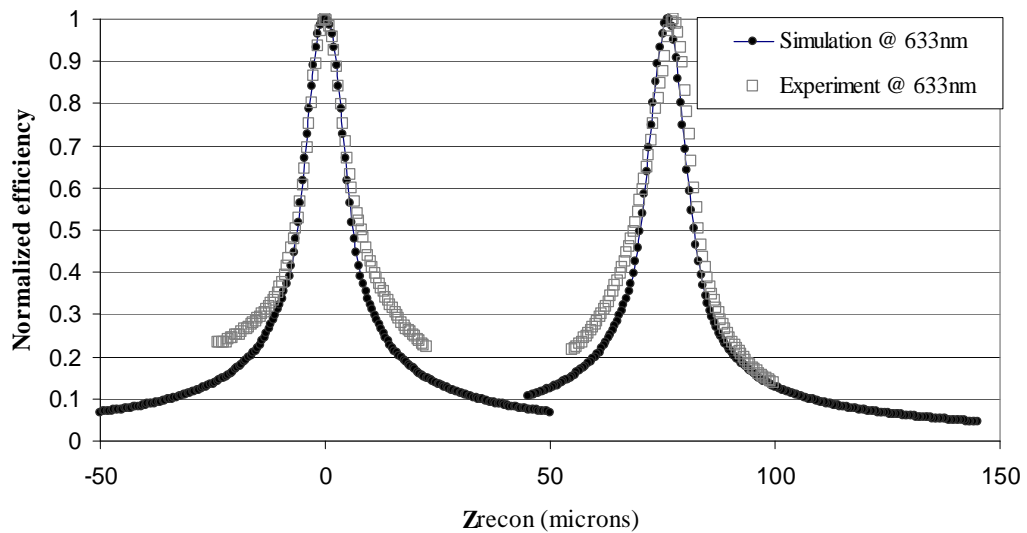
Figure 5.9(a) shows the simulation numerical analysis results for the relationship between  $\Delta Z_{\text{con}}$  and  $\Delta Z_{\text{recon}}$  with the same wavelength of 488nm. Figure 5.9 (b) shows the numerical analysis for the relationship between  $\Delta Z_{\text{con}}$  and  $\Delta Z_{\text{recon}}$  with the different wavelengths of 488nm and 633nm for construction and reconstruction, respectively. It shows that  $\Delta Z_{\text{recon}}$  at the wavelength of 488nm varies from 0 to  $250\mu\text{m}$ , and 0 to  $400\mu\text{m}$  at the wavelength of 633nm, indicating that the holographic filter formed at 488nm is capable of obtaining deeper information within a 3D object at longer wavelength. The modeling results are in good agreement with the measurements and indicate that our model is suitable for analyzing multiplexed gratings made by spherical waves.

Table 5.2. Max.  $\eta$  and angular selectivity ( $\Delta\theta_s$ ) of a hologram with two multiplexed gratings.

		1 <sup>st</sup> grating		2 <sup>nd</sup> grating	
		Simulation	Experiment	Simulation	Experiment
488nm	$\eta_{\max}$	40%	39%	32%	32%
	$\Delta\theta_s$	0.028°	0.03°	0.028°	0.03°
633nm	$\eta_{\max}$	21%	19%	18%	17%
	$\Delta\theta_s$	0.034°	0.037°	0.035°	0.045°



(a)



(b)

Figure 5.8.(a) Numerical and experimental results of the depth selectivity for the hologram of two gratings at 488nm. (b) Numerical and experimental results of the depth selectivity for the hologram of two gratings at 633nm.

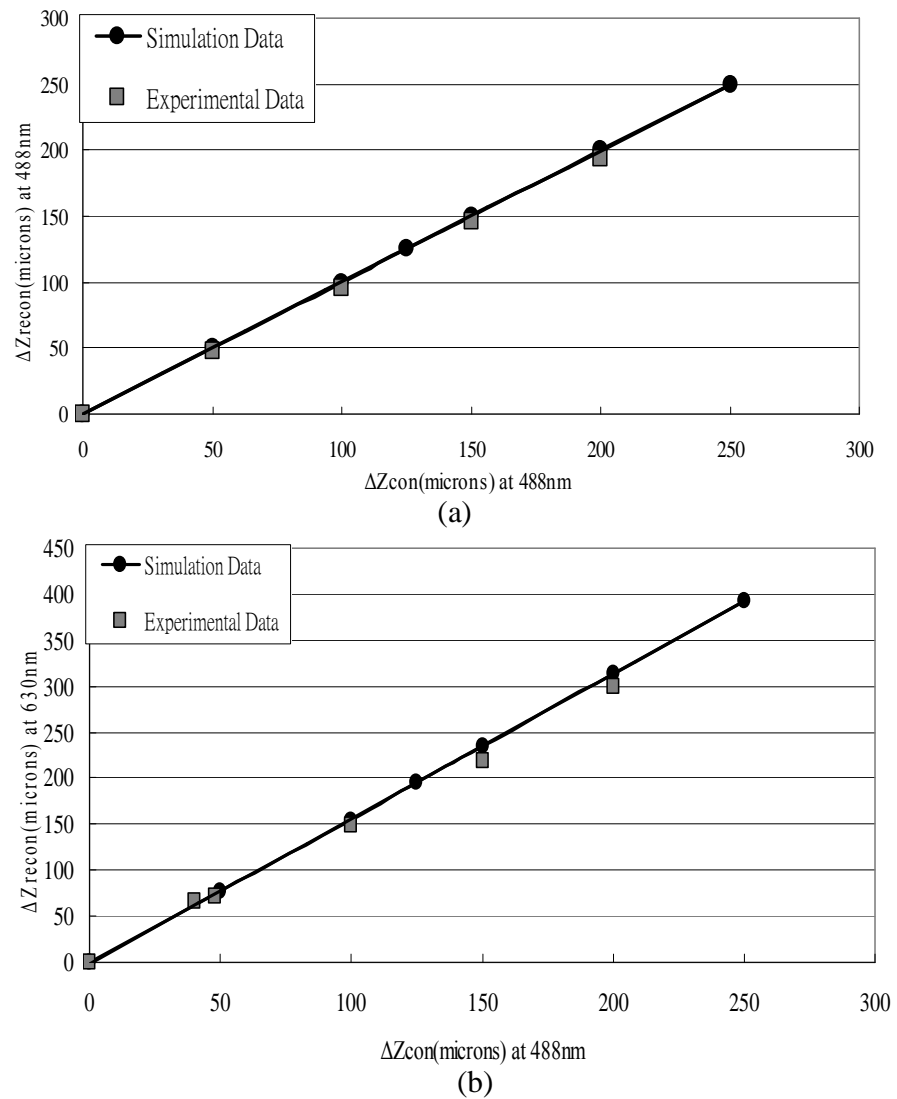


Figure 5.9. Experimental results and numerical analysis for the relationship between  $\Delta Z_{con}$  and  $\Delta Z_{recon}$  (a) at the same wavelength of 488nm for both construction and reconstruction. (b) at the wavelength of 488nm for construction and 633nm for reconstruction.

## Chapter 6. PQ-doped PMMA for Holographic Recording

### 6.1. Introduction

Phenanthrenequinone (PQ)-doped poly(methyl methacrylate) (PMMA) provides several advantages as a holographic recording material, such as low light absorption over a broad spectral band, low shrinkage, and low scattering [53]. The fabrication of PQ-doped PMMA holographic recording material is relatively inexpensive and the material can be prepared in a variety of forms and thickness.

This chapter focuses on the fabrication of the photopolymer and the formation of the grating.

### 6.2. History

PQ-doped PMMA material was first used as a holographic recording material by Veniaminov et. al., who developed it in 1991 [54] for narrow spectral filtering applications. The recording media doped with PQ used as a photosensitive additive can produce a phase holographic material. The molecular structure of the macromolecule (MMA) changes and produces a refractive index modulation. In 2000, Popov [55] demonstrated that the holographic recording material could be highly stable for years at moderate temperatures with a spectral selectivity of a few nanometers. Both characteristics are highly desirable in telecommunication [53][54] and imaging filters [48][49].

PQ-doped PMMA storage material [47][56] has been demonstrated to have a dynamic range of 14. The dynamic range  $M\#$  and normalized  $M\#$  is defined as

$$M\# = \sum_{i=1}^N \sqrt{\eta_i}, \text{ Eq. 6.1}$$

and

$$\text{normalized } M\# = \frac{\sum_{i=1}^N \sqrt{\eta_i}}{\text{SampleThickness}}, \text{ Eq. 6.2}$$

where  $\eta$  is the diffraction efficiency of the grating, and  $N$  represents the largest number of holograms that can be multiplexed in the material before the material is exhausted. Index modulations of  $3 \times 10^{-4}$  with up to 50 holograms multiplexed have been demonstrated in a 3mm thick sample [47][53][56].

### 6.3. Fabrication Process

The holographic recording material is formed by using solutions of methylmethacrylate (MMA), 2,2 -Azobis(2-methylpropionitrile) (AIBN) and (phenanthrenquinone) (PQ) that are mixed at a respective weight ratio of 100:0.5:0.7. The PQ-doped PMMA is an attractive material for making holographic Bragg filters since the material can be formed with minimal shrinkage and refractive index change after processing [57][58].

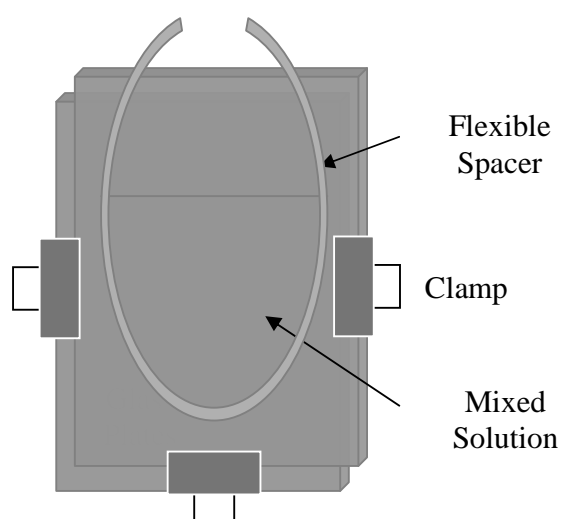


Figure 6.1. Mold for the sample mixture preparation.

The mixture is poured into a mold similar to that shown in Figure 6.1, consisting of two glass plates separated by a flexible spacer. The mixed solution solidifies after curing at 50°C for 120hrs. Both the curing time and temperature were optimized by Maeda and Kostuk in [57].

After the thermal polymerization process is complete, the solid sample is approximately 1.8mm thick. For our experimental system configuration, the resultant material is cut into 5cm×5cm squares and fitted on a sample holder for holographic exposure. Then the sample is left in the dark container to allow localized polymerization and diffusion enhancement. After twenty-four hours of dark polymerization, the sample

is fixed using incoherent light to terminate the photoreaction [57]. The fabrication process is summarized in Figure 6.2.

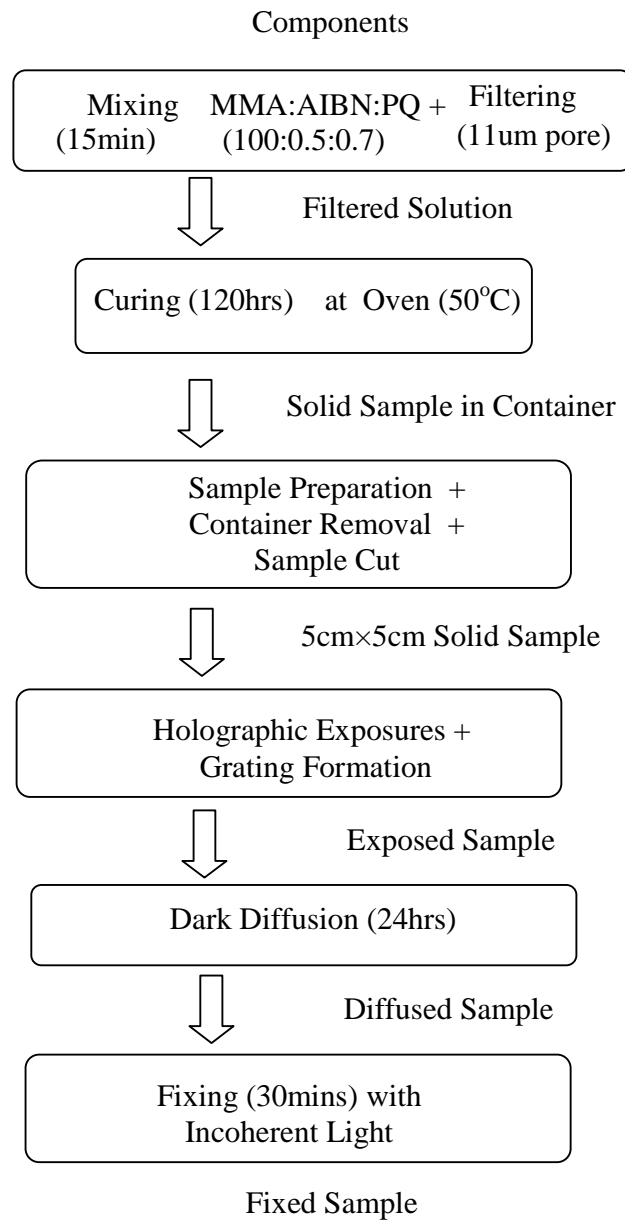


Figure 6.2. Fabrication process and holographic recording flow diagram.

#### 6.4. Grating Formation in PQ-doped PMMA

In the presence of an interference pattern consisting of alternating bright and dark areas in regions of constructive interference, the PQ molecule undergoes the following reaction to produce radicals and form a stable PQ-labeled macromolecule (*HPQR*):



where  ${}^3PQ$  is a triplet-excited PQ molecule, *RH* is the hydrogen-donor polymer macromolecules, *HPQ\** is a semi-quinone radical, and *R\** is the resulting polymer radical.

This process changes the molecular structure of the macromolecules, resulting in an index modulation that grows in the course of the reaction, increasing the strength of the grating [59].

The resulting grating can be visualized as two out-of-phase subgratings. The first subgrating consists of unreacted PQ molecules; the second is formed by PQ photoproduct molecules.

After exposure, the material is placed in a dark container for approximately 24 hours to allow the unreacted PQ molecules slowly to diffuse throughout the sample. During the diffusion process, the first subgrating, comprised of the unreacted PQ molecules,

degrades while the second subgrating, comprised of the PQ photoproduct, strengthens significantly. Thus, the index modulation increases and the diffraction efficiency of the remaining grating increases until the photoreaction is terminated by illumination with incoherent light [57] in the fixing process. The unreacted PQ is activated with incoherent light to ensure that no pattern is recorded [59].

### 6.5. Optimization Method for a Single Grating

A Hamamatsu S1226-44BK silicon detector with an area of  $A_{det} = 0.137 \text{ cm}^2$  and responsivity ( $R$ ) of 0.2383 A/W was used to measure the power of both beams. The detector sensitivity ( $S$ ) is calculated to be  $S = 30.64 \text{ W/A-cm}^2$  at 488 nm using the following expression:

$$S = \frac{1}{R \cdot A_{det}}. \quad \text{Eq. 6.6}$$

The exposure time is calculated using the total irradiance at the recording material and the exposure energy per unit area for PQ-doped PMMA. The irradiance ( $E$ ) at the recording material is calculated:

$$\begin{aligned} E_1 &= I_1 \cdot S \cdot \cos(\theta) \\ E_2 &= I_2 \cdot S \cdot \cos(-\theta), \end{aligned} \quad \text{Eq. 6.7}$$

where  $E_1$  and  $E_2$  are the irradiance of each incident beam and  $I_1$  and  $I_2$  are the electric current reading from the detector (in amperes) for incident beams 1 and 2, respectively.  $\theta$

represents the construction angle. Using the optimized single exposure for PQ-doped PMMA of  $1000 \text{ mJ/cm}^2$  [57]-[59], the exposure time ( $t_E$ ) is calculated:

$$t_E = \frac{1000(\text{mJ/cm}^2)}{E_1 + E_2}. \quad \text{Eq. 6.8}$$

The light regulation mode of the Coherent Innova Model 305 was used to supply a constant ( $\pm 0.5\%$ ) [59] total irradiance of  $E = 30.48 \text{ mW/cm}^2$  ( $I = 0.6 \mu\text{A}$ ) to the sample. Using the expressions above the exposure time can be calculated as  $\tau = 32.8$  seconds when the construction angle  $\theta$  is equal to  $\sim 34^\circ$ .

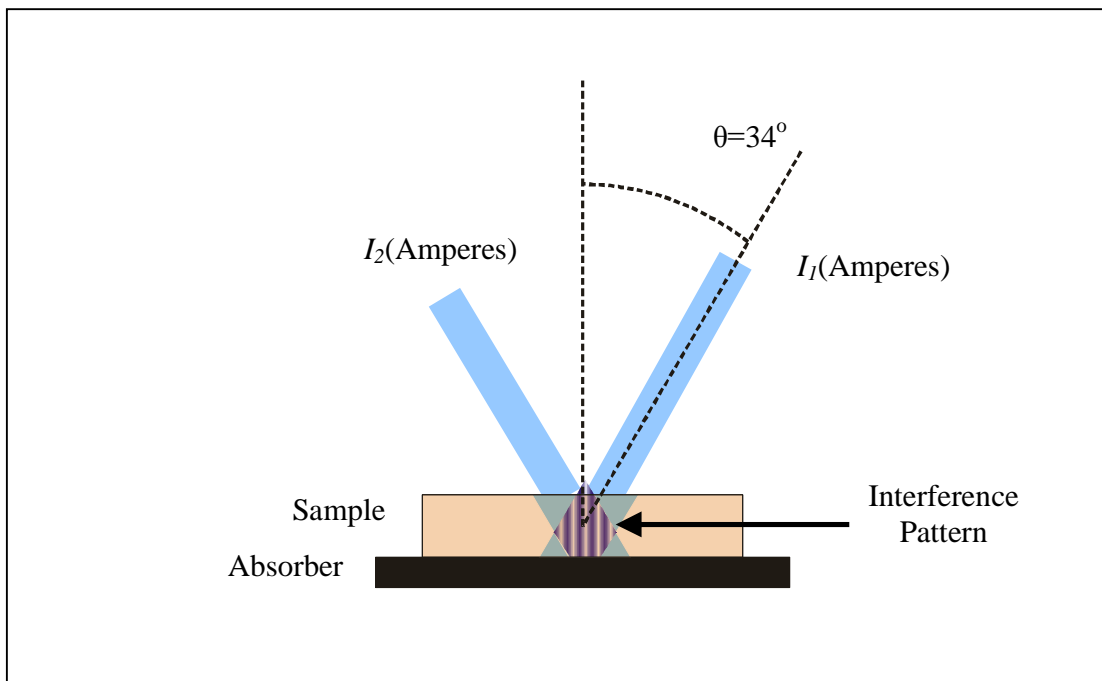


Figure 6.3. Holographic recording setup.

## 6.6. Optimization of Multiplexed Gratings

The multiplexed holographic gratings are recorded with the setup shown in Figure 6.4, using an Argon Ion Laser operating at a wavelength of 488nm. This is the same method described in Section 4.3. The reference beam is a collimated wave and the signal beam is a spherical wave originating from a point corresponding to the depth position within the sample. A different Z position is recorded for each depth that will be imaged within the sample. The positions of the point source in the signal arm are controlled by moving a microscope objective lens with numerical aperture (NA) of 0.65 along the axial direction. A second microscope objective lens with a 0.55NA remains in a fixed position in the signal arm, forming the point source. A relay system is used in the signal arm to maintain constant irradiance at the hologram plane as the 0.65NA microscope object is moved. The nominal angle between two arms is  $\sim 68^\circ$ ; this is changed by  $\Delta\theta$  with each exposure to record a hologram with a different reference beam angle and point source location. The angle settings, point source locations, and exposure time settings are automated using a LabView control system. The hologram exposures are varied to increase the efficiency of gratings that select positions deeper within the tissue sample.

According to Table 5.2 in Section 5.5, the FWHM of angular selectivity ( $\Delta\theta_s$ ) of a hologram is  $\sim 0.03^\circ$ . This implies that, to avoid crosstalk between multiplexed gratings, the angular difference ( $\Delta\theta$ ) between reference beam angles should be greater than  $0.03^\circ$ . In the experiments,  $\Delta\theta$  was set at  $\sim 1^\circ$  to avoid image overlap during reconstruction.

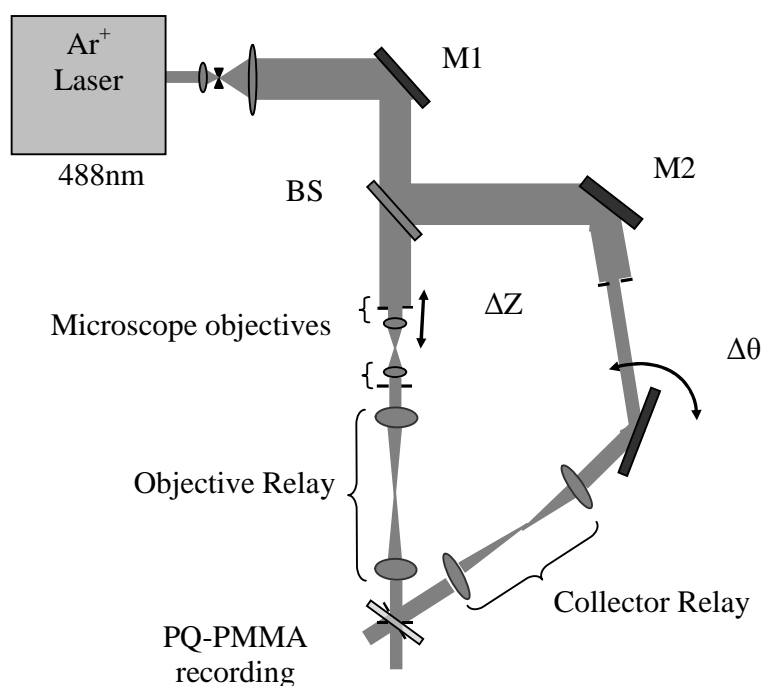
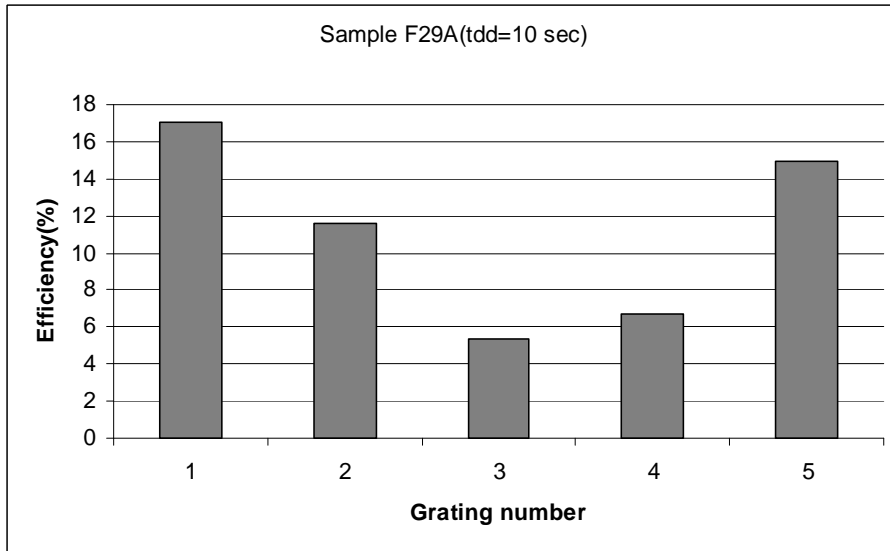


Figure 6.4. Construction setup of the multiplexed holographic gratings.

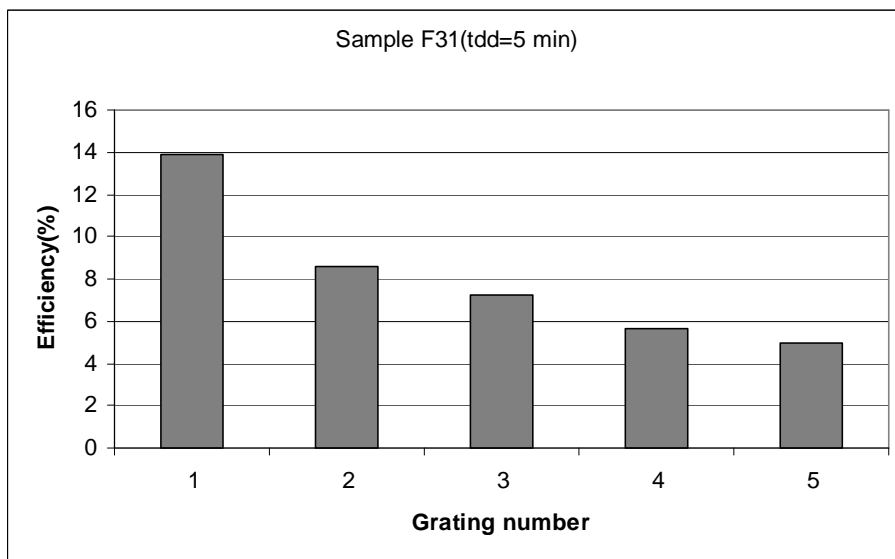
### 6.7. Dark Delay Time and Pre-illumination Exposure

The dark delay time ( $t_{dd}$ ) between each exposure affects the diffraction efficiency ( $\eta$ ) of multiplexed gratings formed in optical polymers [60]. To quantify this effect in PQ-PMMA holograms, five multiplexed gratings were made with two collimated waves ( $\Delta z=0$ , and  $\Delta\theta=1^\circ$ ). These multiplexed gratings were made with dark delay times varying from 10sec to 5min with constant exposure energy ( $\sim 760\text{mJ}/\text{cm}^2$ ) per grating and no pre-exposure energy. Figure 6.5 shows  $\eta$  for the two different values of the dark delay time. The  $t_{dd}$  was 10sec for sample F29A, and 5min for sample F31. Number 1 indicates the

first grating formed in the sequence and number 5 is the last grating. The results show that with a longer delay time the cumulative grating strength ( $M\#$ ) is lower. Therefore, the overall efficiency is lower with a longer delay time and the efficiency of the first grating formed in the sequence is enhanced at the expense of gratings formed with later exposures. When  $t_{dd}$  is shorter (10sec), the efficiency of the last grating formed in the sequence and the average efficiency of all gratings increases.



(a)



(b)

Figure 6.5. Measured multiplexed grating diffraction efficiency with different dark delay times between exposures.

It is important to note that the photoinitiator participates only once in the chemical reaction. The photoinitiator may react with some chemical inhibitors, such as oxygen, during the polymerization process. Thus the reaction of polymerization cannot take place if the inhibitor concentration is too high [60], i.e.,



Pre-illumination exposure (PIE) provides sufficient energy to reduce the concentration of the inhibitor that initially suppresses the creation of free radicals during the polymerization process [60][61][62]. Therefore, PIE also has an important influence on the multiplexed grating efficiency.

Table 6.1. Single gratings with constant exposure of 610mJ/cm<sup>2</sup>

Pre-illumination (mJ/cm <sup>2</sup> )	$\eta$ (%)
0	20
120	38
360	44
460	40
760	48

To simplify the measurement of the PIE effect, holograms were made with constant  $t_{dd}$  and exposure energy ( $\sim 610 \text{ mJ/cm}^2$ ) and with different values of PIE, ranging from 0 to  $\sim 760 \text{ mJ/cm}^2$ . The resulting  $\eta$  performances with different values of PIE are shown in Table 6.1. Two multiplexed gratings were also made with different values of PIE and constant  $t_{dd}$  and exposure energy ( $\sim 610 \text{ mJ/cm}^2$ ). The resultant cumulative grating strengths are shown in Table 6.2. The results indicate that a significant increase in the diffraction efficiency of single and multiple gratings formed in PQ-PMMA is possible with PIE values of a few hundred  $\text{mJ/cm}^2$ .

Table 6.2. Two multiplexed gratings with constant exposure of  $610 \text{ mJ/cm}^2$

Pre-illumination ( $\text{mJ/cm}^2$ )	Cumulative grating strength ( $\sum_{i=1}^{M=2} \sqrt{\eta_i}$ )
0	0.78
220	1.06
290	1.04
360	1.31

After adjusting the exposure energy as shown in Table 3 and adding a pre-exposure of  $360 \text{ mJ/cm}^2$  with constant  $t_{dd}=10 \text{ sec}$ , the efficiencies are significantly improved. The

gratings shown in Table 6.3 and Figure 6.6 were formed with spherical and planar waves with the point source moved by increments of  $\Delta z=50\mu\text{m}$  and separation angle between reference waves of  $\Delta\theta=1^\circ$ . The PQ-PMMA five multiplexed grating sample with the maximum  $\eta$  (46%) and a thickness of  $\sim 1.8\text{mm}$  has an  $M/\#$  of 2.81. The normalized  $M/\#$  ( $M/\#$  divided by sample thickness) is 1.6. close to the reported values in Ref [47] and [56], which have normalized  $M/\#$  1.6 and 1.75 respectively. The diffraction efficiency of grating number 5 was made higher since it is used to image at a deeper point within the sample.

Table 6.3. Five multiplexed gratings with  $t_{\text{dd}}=10\text{sec}$  and a pre-illumination of  $360\text{mJ}/\text{cm}^2$

Grating order	Exposure energy ( $\text{mJ}/\text{cm}^2$ )	$\eta$ (%)
1	579	17
2	670	26
3	762	33
4	853	40
5	944	46

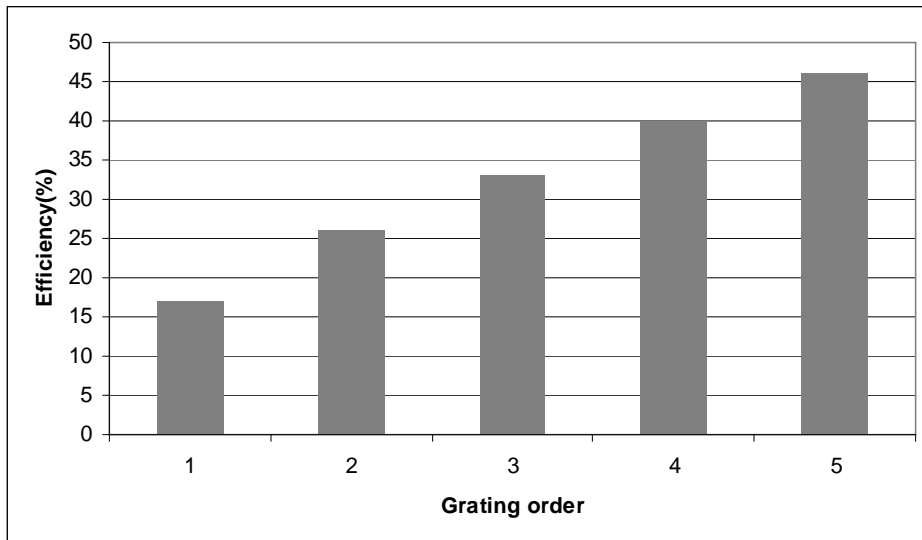


Figure 6.6. Measured multiplexed grating diffraction efficiency of five multiplexed gratings with  $t_{dd}=10\text{sec}$  and a pre-illumination of  $360\text{mJ}/\text{cm}^2$ .

## Chapter 7. Imaging Quality Improvements

### 7.1. Background Subtraction

To enhance features of the simultaneously displayed images, a rapid background subtraction technique was investigated. The primary source of the background is due to the near planar region of the wavefronts close to the center of the hologram aperture. It is expected that images obtained at the same lateral location, but strongly defocused, will consist primarily of background. To perform the background subtraction, the following procedure was applied:

- (1) The original image of interest is recorded along with the background.
- (2) A defocused image is obtained immediately before or after the image of interest.
- (3) Then the out-of-focus image is subtracted from the in-focus image.

Figure 7.1 shows an image of an onion skin using VHIS with 5 multiplexed gratings. The image on the left side in Figure 7.1 is with the obscuring background and the image on the right is with the background subtracted. Figure 7.2 and Figure 7.3 show the resultant images of mouse fat and colon respectively before and after background subtraction. In these fluorescence images, very small features such as colon crypts ( $\sim 20\mu\text{m}$ ) can be seen. With the post imaging technique of background subtraction, the system can provide quick contrast enhanced imaging in approximately two frame collection periods. To quantify the performance of the VHI system for detecting structure in tissue samples, visibility and signal-to-noise ration (SNR) are calculated by

$$Visibility = \frac{I_{\max} - I_{\min}}{I_{\max} + I_{\min}}, \quad \text{Eq. 7.1}$$

and

$$SNR = \frac{\langle I_{\text{signal}} \rangle - \langle I_{\text{background\_noise}} \rangle}{\sigma_{\text{noise}}}, \quad \text{Eq. 7.2}$$

where  $\sigma_{\text{noise}}$  is the variance in noise level. The visibility impacts the contrast ratio of the images and the SNR determines the image quality. In Figure 7.4, a single row of an onion skin image is used to assess the performance of the background subtraction technique for VHIS detecting tissue structures. In this case, visibility is  $\sim(200-100)/(200+100) = 0.33$  for the in-focus image and  $\sim(80-0)/(80+0) = 1$  for the filtered image. SNR is  $\sim 80/2.96=27.03$  for both in-focused and filtered images. The results indicate that simple post-processing can be used to enhance the image of interest.

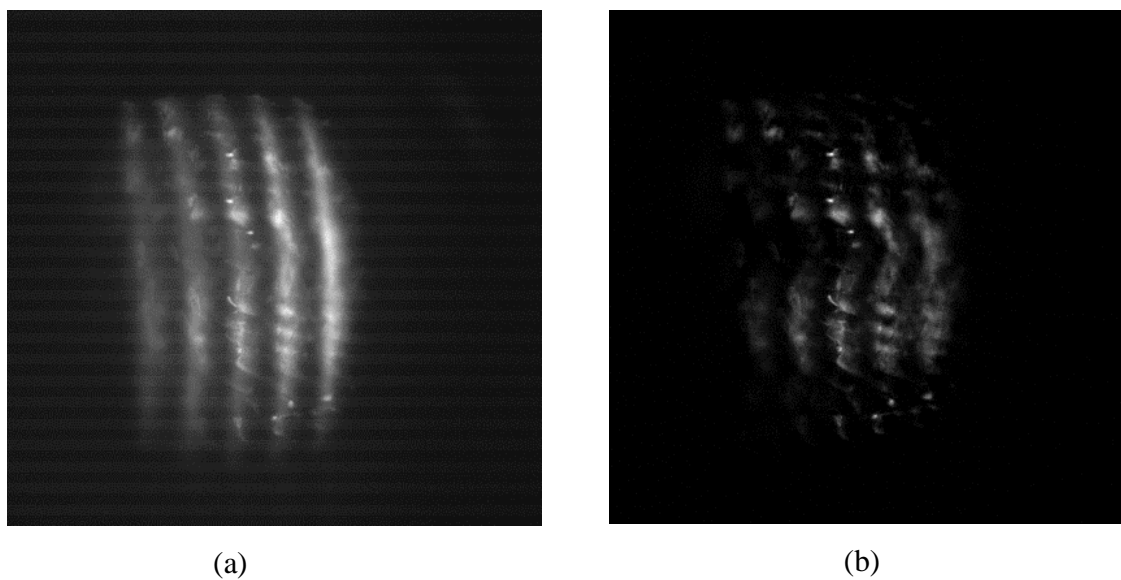


Figure 7.1. Image enhancement with background subtraction applied simultaneously to five images from different depths within an onion peel sample. Left image is the structure of interest plus the background. Right image is the structure of interest after the background is subtracted.

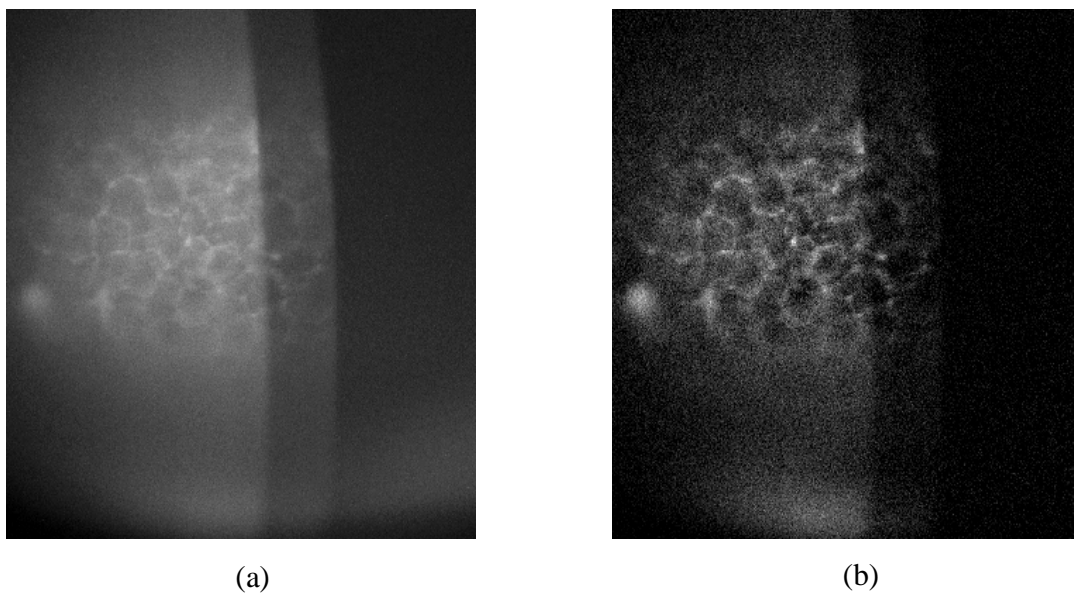


Figure 7.2. Fluorescence imaging with the volume holographic imaging system of mouse fat. (a) Image of mouse fat with background noise. (b) Filtered image with background subtraction applied simultaneously to the two sections in (a).

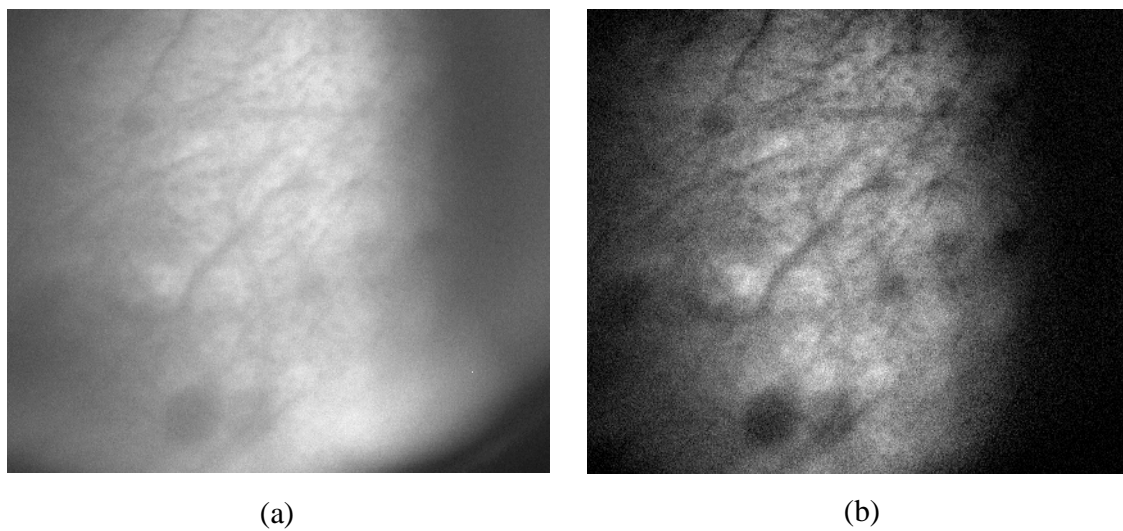


Figure 7.3. Fluorescence imaging with the volume holographic imaging system of mouse colon (a) Image of mouse colon with background noise and (b) Filtered image with background subtraction applied simultaneously to the two sections in (a).

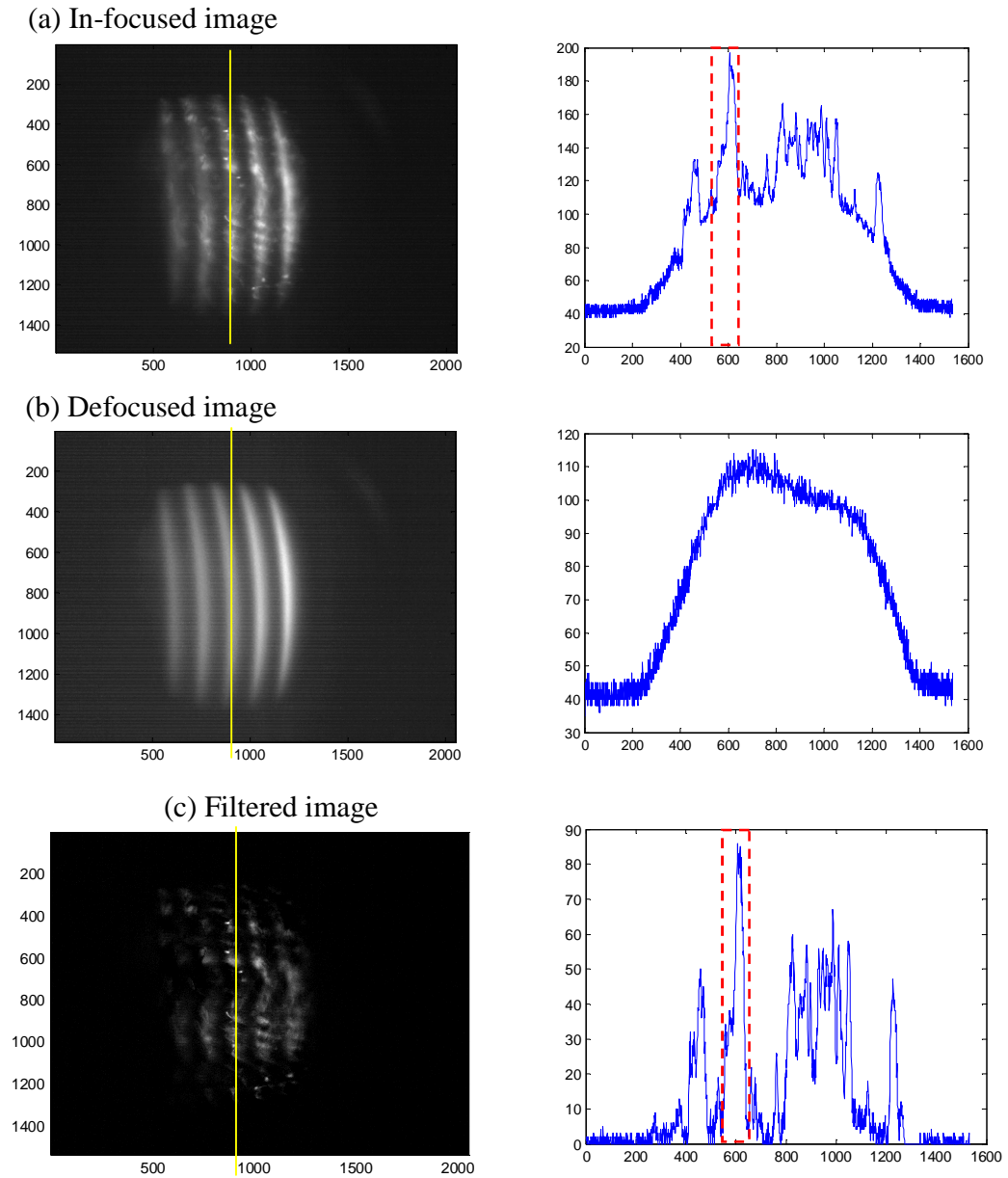


Figure 7.4. A single column of (a) in-focused, (b) out-of-focused, (c) filtered images obtained for the use of contrast and SNR measurements.

## 7.2. Non-overlapping Fluorescence Images with Larger Angular Separation

In Figure 7.2 and Figure 7.3, the bandwidth of the fluorophore emission spectra is very wide ( $\sim 100\text{nm}$ ) and causes overlap between projections from different depths. However, this condition can be corrected by designing the holograms to have larger angular separation ( $\Delta\theta_{ref}$ ) between each exposure.

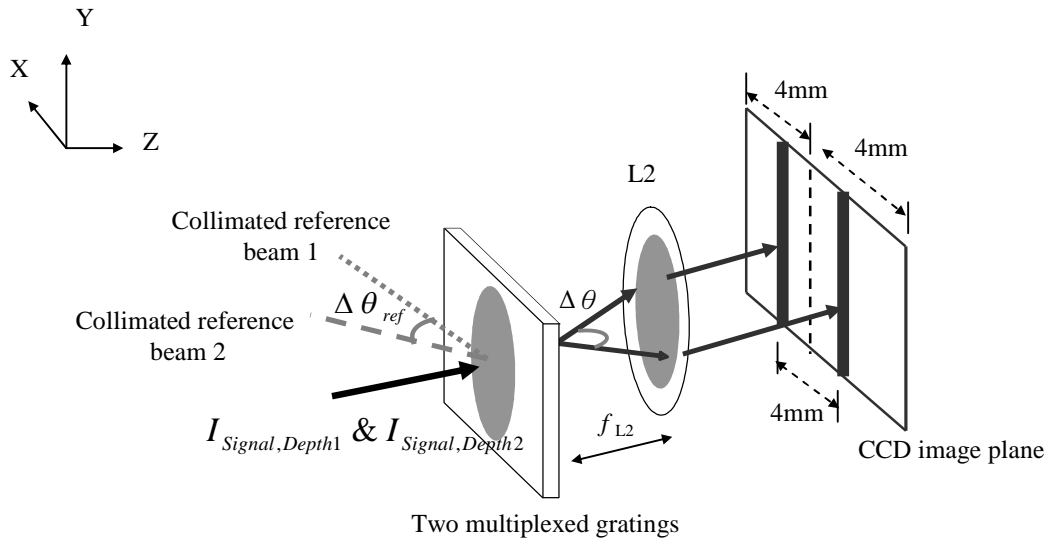


Figure 7.5. Reconstruction setup for non-overlapping images on CCD plane.

The width of the Andor iXon CCD array is  $\sim 8\text{mm}$ , and the focal length ( $f_{L2}$ ) of the L2 is  $20\text{mm}$ . In Figure 7.5, the distance of two reconstructed images on the CCD plane is designed to be  $4\text{mm}$  to avoid overlap and thus  $\Delta\theta = 4\text{mm}/f_{L2} \sim 11^\circ$ . According to the K-vector closure relation as described in Eq. 7.3 and Eq. 4.3,  $\Delta\theta_{red}$  is  $\sim 8^\circ$ , and an algorithm for employing this calculation is developed by Matlab in Appendix.

Figure 7.6 shows two depth-resolved images simultaneously displayed using this system. The field of view of the image is  $\sim 1.46\text{mm} \times 1.46\text{mm}$ . The image of mouse fat is reconstructed by a hologram of two multiplexed gratings with diffraction efficiencies of  $\sim 60\%$  and  $40\%$  that simultaneously image planes just below the tissue surface and  $\sim 65\mu\text{m}$  deep in the tissue. The sample was stained with Acridine Orange and illuminated using a tripled Nd:YAG laser ( $355\text{nm}$ ).

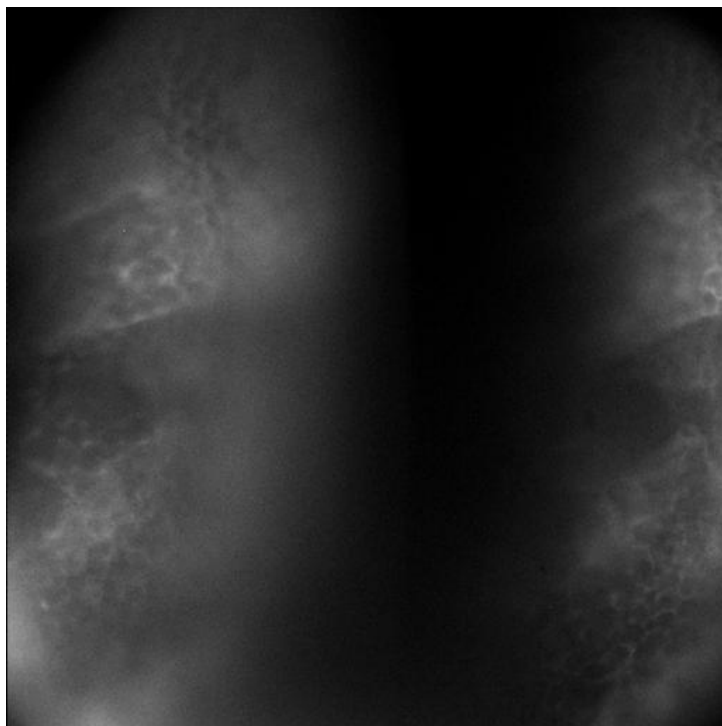


Figure 7.6. Fluorescence images of mouse fat stained with Acridine Orange. The figure was obtained with the VHIS system using a two grating hologram with an  $8^\circ$  angle between the reference beams. Two simultaneous depth-resolved images are projected and the depth separation is  $\sim 65\mu\text{m}$ .

Figure 7.7 and Figure 7.8 show the resultant images of mouse fat and colon respectively after background subtraction. In these fluorescence images, very small features such as colon crypts ( $\sim 20\mu\text{m}$ ) can be seen. With the post imaging technique of background subtraction, the system can provide quick contrast enhanced imaging in approximately two frame collection periods.

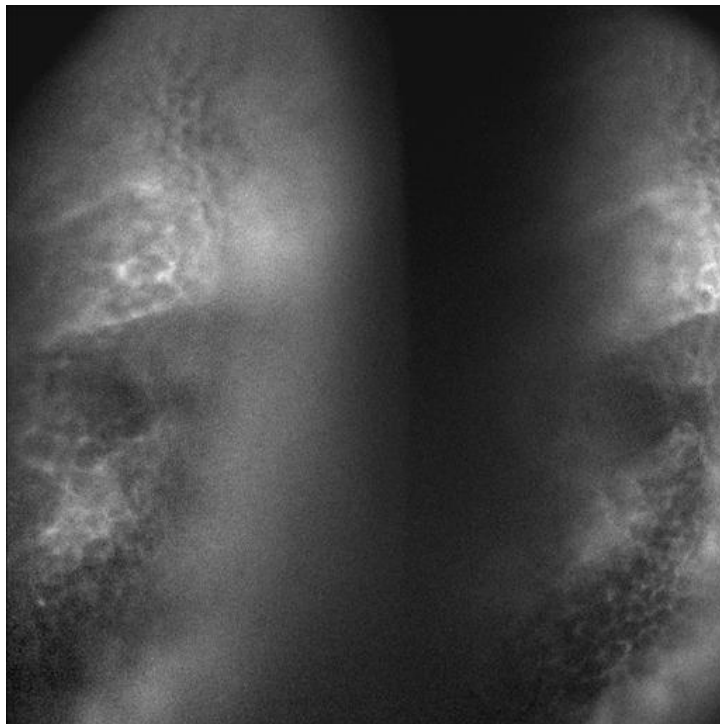


Figure 7.7. Image enhancement with background subtraction applied simultaneously to two depth-resolved images in Figure 7.6.

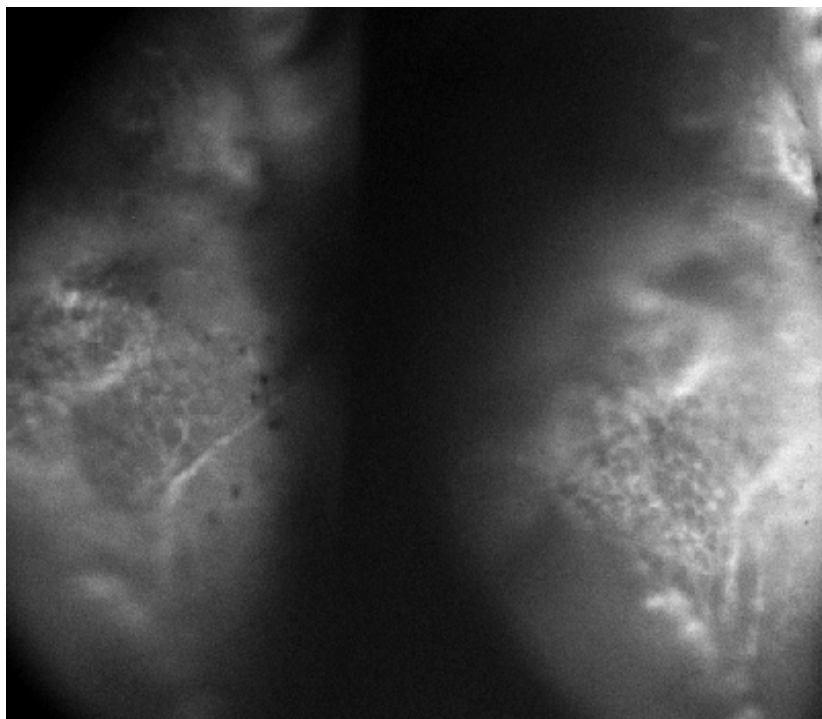


Figure 7.8. Fluorescence images of mouse colon stained with Acridine Orange, obtained with the VHIS system. Image enhancement with background subtraction has been applied. Colonic crypts ( $\sim 20 \mu\text{m}$  cross-section) can be visualized.

## Chapter 8. Conclusion

### 8.1. POCT

The system design and experimental results of a POCT system that is capable of acquiring an image without the need for mechanical scanning in the lateral dimension were demonstrated. The probe tip consists of a linear fiber array with 15 $\mu$ m diameter SMFs, and an imaging GRIN-rod lens with the fractional pitch of 0.48 and 1:1 magnification. When packaged, the probe tip can fit in an assembled endoscope with a diameter less than 2mm, providing a system transverse image resolution of 15 $\mu$ m at a wavelength of 1.31 $\mu$ m. Other contributions on this research include: are listed in the following:

- (1) A Monte Carlo analysis of the backscattered signal crosstalk for different types of SMF and MMF fibers was conducted. The results suggest that fibers with large NA and small fiber cores will provide good scattered signal detection in array configurations.
- (2) In the backscattered measurements, the reduced diameter fiber array was immersed into an Intralipid tissue phantom solution to evaluate the levels of backscattered signal and crosstalk. The backscattered measurements are in good agreement with the Monte Carlo simulation results and indicate that this model is suitable for analyzing reduced diameter fiber arrays.

- (3) A lens-less proximity sensor utilizing a reduced diameter fiber array has also been demonstrated. It shows that high-contrast interference patterns can be obtained with light reflected from a mirror positioned out to  $250\mu\text{m}$  that is considerably further away from the tip of the fiber than the Rayleigh range corresponding to the beam emitted from the fiber.

Future work will involve expanding the number of fibers to 100, which will provide a larger transverse imaging field. By careful arrangement of the non-etched and tapered portion of the fibers, the width of a 100 fiber array will be less than 2mm in diameter and suitable for use in a standard diameter endoscope system. An array of CMOS photoreceiver and demodulation circuits that can be scaled to 100 channels has recently been developed [63]. In addition, integrated 3dB couplers in an ion-exchanged technique [64][65] have been designed for the 100-channel POCT system. These developments will enable a compact POCT system with integrated electronic scanning capability.

## **8.2. VHIS**

The successful system design and experimental results of a VHIS that is capable of obtaining multiple depth-resolved images simultaneously without scanning were presented. VHIS is a three-dimensional imaging system incorporating multiplexed holographic gratings to visualize tissue structures. This system has demonstrated a lateral resolution of  $4.5\mu\text{m}$  using a high density CCD array (Lumenera 6 Mpixel camera) with  $2.8\times$  system magnification, and a resolution of  $7.8\mu\text{m}$  using a highly sensitive CCD array

(Andor iXon camera) with 5.6× system magnification. Experimental results in Chapter 4 and Chapter 7 have shown that the system is able to obtain an imaging depth of 200μm with field of view of 1.46mm×1.46mm.

Holographic gratings formed in volume PQ-PMMA photopolymer have narrowband angular and spectral transmittance filtering properties which enable VHIS to extract simultaneous spatial and spectral information from biological tissue samples. The optimization of multiplexed holographic filters formed in PQ-PMMA at 488nm has been presented in Chapter 6. The dark delay time between exposure and the pre-illumination exposure of the polymer are varied to optimize the diffraction efficiency of multiplexed holographic filters. The resultant holographic filters can enhance the performance of the VHIS.

In addition, numerical analyses for the curved gratings have been developed in Chapter 5. This model can be extended for multiplexed curved gratings, and each multiplexed grating is considered independent if the crosstalk between gratings can be ignored. The simulations predict that the curved gratings have strong selectivity with  $\sim 0.035^\circ$  in angle and  $\sim 12\mu\text{m}$  in depth using a longer reconstruction wavelength of 633nm. Simulations demonstrate that the depth separation ( $\Delta Z_{\text{recon}}$ ) varies from 0 to 400μm at the reconstruction wavelength of 633nm while the value of  $\Delta Z_{\text{recon}}$  changes from 0 to 250μm using 488nm for reconstruction. The results indicate that the volume curved gratings can be used as holographic angle-depth filters to provide spatial-spectral information from an object. The simulations also indicate that the gratings formed at 488nm are capable of

obtaining deeper information from an object using a longer reconstruction wavelength. The simulation results are in good agreement with the experimental measurements, demonstrating that the model is suitable for analyzing curved gratings of the VHIS.

Finally, a rapid background subtraction technique has been applied to enhance features of the simultaneously displayed images. The primary source of the background is due to the near planar region of the wavefronts being close to the center of the hologram aperture. Thus, the images obtained at the same lateral location, but strongly defocused, consist primarily of background. With the post imaging technique of background subtraction, the system can provide quick contrast enhanced imaging in near real time of approximately two frame collection periods.

Future work on this project may include the following:

- (1) The development of a mold which can be used to make a thicker hologram and provide better surface quality.
- (2) The improvement of wavefront aberration correction and spatial-spectral selectivity of multiplexed gratings which reduce the width of PSF and background noise level.
- (3) The development of the numerical analysis for curve gratings incorporating Zemax, which will be helpful to employ in post-imaging applications.

- (4) The improvement of background subtraction techniques and other fast post-imaging process to enhance image quality.

## APPENDIX A

The Monte Carlo simulator [27][37] in Matlab to evaluate the levels of backscattered signal and crosstalk with the reduced diameter fiber array immersed into an Intralipid tissue phantom solution.

```

n_silica=1.4675;    % index for silica ;
Num_layers=1;     % 1 layer is tissue;
mua=[0.001];      % 1/cm ; mua=[0.0001]
mus=[85];         % 1/cm ; mus=[85]
n=[1.338,1];      % index for tissue & layers ;n=[1.37,1];
g=[0.4];          % anisotropy value;g=[0.7]

z_d=[0 1];        % z position of boundaries(cm);

Nz=200;           % # of dz;
%Nr=50;           % # of dr;
%Na=1;            % # of da;

dr=0.02e-3;      % cm;
Nr=5000;         % # of dr;

dz=0.005;        % cm;
NA=0.1192;       % fiber as detector;
da=asin(NA);
Na=fix(pi/2/da); % # of da;

```

```
COSZERO=1.0-1e-12;
COS90D=1e-6;

wth=1e-6;                % wth=threshold value;

%cos_crit=sqrt(1.0 - n1*n1/(n2*n2));
CHANCE=0.1;              %CHANCE=1/m; m=10;
photons=1.0e6;
% albedo=mus/(mus+mua);

cos_crit0=zeros(1,Num_layers);
cos_crit1=zeros(1,Num_layers);

r1=zeros(1,photons);
Rd_ra=zeros(Nr,Na);
Tt_ra=zeros(Nr,Na);
A_rz=zeros(Nr,Nz);
w=zeros(1,photons);
Rd_r=zeros(Nr);
Rd_a=zeros(Na);
Tt_r=zeros(Nr);
Tt_a=zeros(Na);
A_z=zeros(Nz);
A_l=zeros(Num_layers);

lambda=1.310e-4;
```

```

if n(1) >= n_silica                % CriticalAngle---cos_crit0(1)----(begin)
    cos_crit0(1)=sqrt(1.0-(n_silica/n(1))^2);
else
    cos_crit0(1)=0;
end                                % CriticalAngle---cos_crit0(1)----(end)

if n(1) >= n(2)                    % CriticalAngle---cos_crit1(1)----(begin)
    cos_crit1(1)=sqrt(1.0-n(2)^2/n(1)^2);
else
    cos_crit1(1)=0;
end                                % CriticalAngle---cos_crit1(1)----(end)

if n(2) >=n(1)                    % CriticalAngle---cos_crit0(2)---(begin)
    cos_crit0(2)=sqrt(1.0-(n(1)/n(2))^2);
else
    cos_crit0(2)=0;
end                                % CriticalAngle---cos_crit0(2)----(end)

for i=1:photons

    %n1=n(1);n2=n(2);n3=n(3);mua1=mua(1);mus1=mus(1);
    r1(i)=Rsp(n(1),n(2),mua(1),mus(1));        % launch photon(start);
    w(i)=1-r1(i);                            % w=weight;
    w_tissue=0.42e-3;                        % beam radius on tissue(cm); fiber core diameter is 8.4 um;
    %w_eff=1.1*w_tissue;                    % effective beam radius =1.1*w_tissue;

```

```

wst=w_tissue; % since no lens, so w_tissue=wst % wst= beam waist of
Gaussian beam (cm);

w0=wst;

z0=pi*n(1)*w0^2/lambda;

thetamax=asin(NA/n(1)); % divergence angle of Gaussian beam;

d=50*wst; % d=10*wst; % we just need a distance d,and it's not a specific d.

w_d=w0*(1+(d/z0)^2)^0.5; % for simplicity,just choose d=10*wst;

% x=wst*sqrt(-log(1-rand)/2);
% uz=cos(x*thetamax/w_d); uy=0;ux=sin(x*thetamax/w_d);
% x=x*wst/w_d; y=0; z=z_d(1);

x=w0*sqrt(-log(1-rand)/2);
uz=cos(x*thetamax/w0); uy=0;ux=sin(x*thetamax/w0);
x=x; y=0; z=z_d(1);

dead=0;
layer=1;
s=0;sleft=0; % s = step size; sleft = step size left;

while ( dead == 0 )
    %%HopDropSpin in Tissue(begin);

    mua_layer = mua(layer);

    mus_layer = mus(layer);

    if (sleft==0.0) % step size in tissue;

```

```

rnd=rand;                % rnd=rand;
s=-log(rnd)/(mua_layer+mus_layer);
else
s=sleft/(mua_layer+mus_layer);
sleft=0;
end
z0_layer=z_d(layer);      % top position of current layer
z1_layer=z_d(layer+1);    % bottom position of current layer
[hit,s,sleft]=HitBoundary(z,z0_layer,z1_layer,uz,s,sleft,mua_layer,mus_layer);
%% hit
%% s
%% sleft
if (hit == 1)            %%% Hit Boundary;
[x,y,z] = Hop(s,ux,uy,uz,x,y,z); %Hop ;

if (uz < 0)             %% CrossUpOrNot (begin);
if (layer==1)          % make sure after layer-1 >= 1;
ni=n(layer);
nt=n_silica;
else                    % ni=n(layer); nt=n(layer-1);
ni=n(layer);
nt=n(layer-1);
end
if (-uz <= cos_crit0(layer)) % TIR(total internal reflection) ;
r=1;
else

```

```

[r,uz1]=RFresnel(ni,nt,-uz);
end

if (rand > r)          %%%%% rand > r;
                       %%%%% where r=R(alpha) in paper;
                       %%%%% if (rand > r), then the photon transmit;
                       %%%%% if (rand <= r), then the photon internal reflected;

if(layer==1)
    uz=-uz1;
    ir=fix(sqrt(x*x+y*y)/dr)+1;    % RecordR (for Up action);
    if (ir > Nr)
        ir=Nr;
    end

    ia=fix(acos(-uz)/da)+1;

    if (ia > Na)
        ia=Na;
    end

    Rd_ra(ir,ia)=Rd_ra(ir,ia)+w(i)*(1-0); % r= RFresnel=0 if layer= 1st==> transmit to air;
    w(i)=0; dead=1;          % break; % Photon dead;

else
    layer=layer-1;
    ux=ux*ni/nt;
    uy=uy*ni/nt;
    uz=-uz1;

```

```

end
else
    uz=-uz;
end          %% CrossUpOrNot (end);
else          %% CrossDnOrNot (begin);
    if (layer==Num_layers) % make sure after layer+1 <= Num_layers;
        ni=n(layer);
        nt=n_silica;
    else
        ni=n(layer);
        nt=n(layer+1);
    end
    if (uz <= cos_crit1(layer)) % TIR(total internal reflection) ;
        r=1;
    else
        [r,uz1]=RFresnel(ni,nt,uz);
    end

    if (rand > r)    %%%%%%%%% rand > r;
        if (layer==Num_layers)
            uz=uz1;
            ir=fix(sqrt(x*x+y*y)/dr)+1;    % RecordT (for Down action);
            if (ir > Nr)
                ir=Nr;
            end
        end
    end

```

```

        ia=fix(acos(uz)/da)+1;

        if (ia > Na)
            ia=Na;
        end

        Tt_ra(ir,ia)=Tt_ra(ir,ia)+w(i)*(1-0); % r= RFresnel=0 if layer= 1st==> transmit to top
layer;

        w(i)=0; dead=1;          %break;% Photon dead;

        else

            layer=layer+1;

            ux=ux*ni/nt;

            uy=uy*ni/nt;

            uz=uz1;

        end

        else

            uz=-uz;

        end          %% CrossDnOrNot (end);

    end

elseif (hit == 0)    %%% Not Hit Boundary;

    [x,y,z] = Hop(s,ux,uy,uz,x,y,z); %Hop;

    iz=fix(z/dz)+1; % Drop ;

    if (iz > Nz)

```

```

    iz=Nz;

end

ir=fix(sqrt(x*x+y*y)/dr)+1;

if (ir > Nr)

    ir=Nr;

end

mua_layer=mua(layer);

mus_layer=mus(layer);

dwa=w(i)*mua_layer/(mua_layer+mus_layer);

w(i)=w(i)-dwa;

A_rz(ir,iz)=A_rz(ir,iz)+dwa;

g_layer=g(layer);

cost=SpinTheta(g_layer); %%%%% SpinTheta has rand,too ; % Spin;

sint=sqrt(1-cost*cost); %%%%% spin : choose a new direction for photon propagation;

%%%%%%%% by polar deflection angle theta and azimuthal angle psi;

%%%%%%%% and azimuthal angle psi;

psi=2*pi*rand; %%%%% psi=2*pi*rand; %spin psi 0~2pi;

cosp=cos(psi);

if (psi < pi)

    sinp=sqrt(1-cosp*cosp);

else

    sinp=-sqrt(1-cosp*cosp);

end

```

```

if (abs(uz) >COSZERO)
    ux=sint*cosp;
    uy=sint*sinp;
    uz=cost*sign(uz);
else
    ux_1=ux;
    uy_1=uy;
    uz_1=uz;
    temp=sqrt(1.0-uz*uz);
    ux=(sint*(ux_1*uz_1*cosp-uy_1*sinp)/temp)+(ux_1*cost);
    uy=(sint*(uy_1*uz_1*cosp+ux_1*sinp)/temp)+(uy_1*cost);
    uz=-sint*cosp*temp+uz_1*cost;
end

end                                %%HopDropSpin in Tissue(end);
end

if ((w(i) < wth) & (dead ==0))
    if (w(i)==0)                    % Roulette;
        dead=1;
    elseif (rand < CHANCE)          %%% rand < CHANCE;
        w(i)=w(i)/CHANCE;
    else
        dead=1;
    end
end
end

```

```
end

Rd_a=sum(Rd_ra);                % scale begin;
if (Na==1)
    Rd_r=Rd_ra';
else
    Rd_r=sum((Rd_ra)');
end
Rd=sum(Rd_a');

Tt_a=sum(Tt_ra);
if (Na==1)
    Tt_r=Tt_ra';
else
    Tt_r=sum((Tt_ra)');
end
Tt=sum(Tt_a');

scale_1=4*pi*pi*dr*sin(da/2)*dr*photons;
for ir=1:Nr
    for ia=1:Na
        scale_2=1/((ir-0.5)*sin(2.0*(ia-0.5)*da)*scale_1);
        Rd_ra1(ir,ia)=Rd_ra(ir,ia).*scale_2;
        Tt_ra1(ir,ia)=Tt_ra(ir,ia).*scale_2;
```

```

    end

end

scale_1=2*pi*dr^2*photons;

for ir=1:Nr

    scale_2=1/((ir-0.5)*scale_1);

    Rd_r1(ir)=Rd_r(ir).*scale_2;

    Tt_r1(ir)=Tt_r(ir).*scale_2;

end

scale_1=2*pi*da*photons;

for ia=1:Na

    scale_2=1/(sin((ia-0.5)*da)*scale_1);

    Rd_a1(ia)=Rd_a(ia).*scale_2;

    Tt_a1(ia)=Tt_a(ia).*scale_2;

end

scale_2=1/photons;

Rd=Rd*scale_2;

Tt=Tt*scale_2;

scale_1=2*pi*dr*dr*dz*photons;

for iz=1:Nz

    for ir=1:Nr

        A_rz1(ir,iz)=A_rz(ir,iz)/((ir-0.5)*scale_1);

    end

end

end

```

```

A_z=sum(A_rz);

A=sum(A_z');

scale_1=1/(dz*photons);

for iz=1:Nz

    A_z(iz)=A_z(iz)*scale_1;

end

A=A/photons; % scale end;

%%%%%%%%%%%%%%%%%%%%%%%%%%%%%%%%%%%%%%%%%%%%%%%%%%%%%%%%%%%%%%%%%%%%%%%% calculate detector (begin) RR=0.70e-3 rr=w_tissue=0.42e-3 ;

RR=0.70e-3;% fiber radius (um);

rr=w_tissue; % core radius (um);

DD=2*RR-rr;

laucn_fiber=sum(Rd_ra1(1:round(rr/dr),1)); %%% how much go back to the launched fiber; the
launched fiber is at 1st ring;

Area_fiber=pi*rr^2; %%% fiber core diameter=8.4 um=0.84e-3 (cm); so radius=0.42e-
3(cm);

signal_lauch=laucn_fiber*Area_fiber/Area_fiber;

Rd_ring=[];

Area_ring=[];

for i=0:9 %%% 10 channel fiber array;

    start_num=(DD+dr)/dr+i*(DD+rr)/dr;

    end_num=start_num+(2*round(rr/dr)-1);

```

```

Rd_ring=[Rd_ring,sum(Rd_ra1(start_num:end_num,1))];

Area_det=pi*rr^2;

Area_ring=[Area_ring,pi*((end_num)*dr)^2-pi*((start_num-1)*dr)^2];

end

crosstalk=Rd_ring*Area_det./Area_ring;

db=10*log10(crosstalk/signal_lauch);      %%% dB value;

%db_13=10*log10(sum(Rd_ra1(90:171,1))*pi*rr^2/(pi*(1.71e-3)^2-pi*(0.89e-3)^2)/signal_lauch); % 13
um center spacing away;

%%%%%%%%%%%%%%%%%%%%%%%%%%%%%%%%%%%%%%%%%%%%%%%%%%%%%%%%%%%%%%%%%%%%%%%% calculate detector (end);

%%%%%%%%%%%%%%%%%%%%%%%%%%%%%%%%%%%%%%%%%%%%%%%%%%%%%%%%%%%%%%%%%%%%%%%% calculate detector (begin) RR=0.70e-3 rr=w_tissue=0.42e-3 ;

RR=0.64e-3;% fiber radius (um);

rr=w_tissue; % core radius (um);

DD=2*RR-rr;

laucn_fiber=sum(Rd_ra1(1:round(rr/dr),1));      %%% how much go back to the launched fiber; the
launched fiber is at 1st ring;

Area_fiber=pi*rr^2;      %%% fiber core diameter=8.4 um=0.84e-3 (cm); so radius=0.42e-
3(cm);

signal_lauch=laucn_fiber*Area_fiber/Area_fiber;

Rd_ring=[];

Area_ring=[];

for i=0:9      %%% 10 channel fiber array;

    start_num=(DD+dr)/dr+i*(DD+rr)/dr;

```

```

end_num=start_num+(2*round(rr/dr)-1);

Rd_ring=[Rd_ring,sum(Rd_ra1(start_num:end_num,1))];

Area_det=pi*rr^2;

Area_ring=[Area_ring,pi*((end_num)*dr)^2-pi*((start_num-1)*dr)^2];

end

crosstalk=Rd_ring*Area_det./Area_ring;

db13=10*log10(crosstalk/signal_lauch);      %%% dB value;

%%db_13=10*log10(sum(Rd_ra1(90:171,1))*pi*rr^2/(pi*(1.71e-3)^2-pi*(0.89e-3)^2)/signal_lauch); % 13
um center spacing away;

%%%%%%%%%%%% calculate detector (end);

function [Hit, s, sleft] = HitBoundary(z,z0,z1,uz,s,sleft,mua,mus)

% z0=0.0;      % (cm), the top of the 1st layer;

% z1=0.4;      % (cm), the bottom of the 1st layer;

if (uz > 0)      %%% hit the boundary:

    dl_b=(z1-z)/uz; % dl_b>0;

elseif (uz < 0)

    dl_b=(z0-z)/uz; % dl_b>0;

end

if ((uz ~=0) & (s > dl_b)) % not horizontal && crossing boundary;

    mut=mua+mus;

    sleft=(s-dl_b)*mut;

```

```
s=dl_b;

Hit=1;
else
Hit=0;
end

function [x,y,z] = Hop(s,ux,uy,uz,x,y,z)

x=x+s*ux;
y=y+s*uy;
z=z+s*uz;

function [r, ca2] = RFresnel(n1,n2,ca1)

COSZERO=1.0-1e-12;
COS90D=1e-6;

if (n1==n2)      % match boundary;
ca2=ca1;
r=0;
elseif(ca1 > COSZERO) % normal incident;
ca2=ca1;
r=(n2-n1)/(n1+n2);
r=r^2;
elseif (ca1 < COS90D) % very slant;
ca2=0.0;
r=1;
```

```

else          % general;

    sa1=sqrt(1-ca1*ca1);

    sa2=n1*sa1/n2;

    if (sa2 >= 1.0) % double check for total internal reflection;

        ca2=0.0;

        r=1.0;

    else

        ca2=sqrt(1-sa2*sa2);

        cap=ca1*ca2-sa1*sa2; % c+=cc-ss;

        cam=ca1*ca2+sa1*sa2; % c-=cc+ss;

        sap=sa1*ca2+ca1*sa2; % c+=sc+cs;

        sam=sa1*ca2-ca1*sa2; % c-=sc-cs;

        r=0.5*sam*sam*(cam*cam+cap*cap)/(sap*sap*cam*cam);

    end

end

function r1 = Rsp(n1,n2,mua1,mus1)

n_silica=1.4675;

temp=(n_silica-n1)/(n_silica+n1);

r1=temp*temp;

if((mua1==0) & (mus1==0))

    temp=(n1-n2)/(n1+n2);

    r2=temp*temp;

    r1=r1+(1-r1)^2*r2/(1-r1*r2);

end

```

```
function cost = SpinTheta(g)

if (g==0.0)
    cost=2*rand-1; %%%%% cost=2*rand-1;
else
    temp=(1-g^2)/(1-g+2*g*rand); %%%%% temp=(1-g^2)/(1-g+2*g*rand);
    cost=(1+g^2-temp^2)/(2*g);
    if (cost < -1)
        cost=-1;
    elseif (cost > 1)
        cost=1;
    end
end
end
```

## APPENDIX B

Kogelnik program [39] in Matlab code to redesign the hologram for VHIS system with larger angular separation for each exposure.

```

clear;

lambda0=488; % wavelength (unit: nm) in free space;
d_lambda=112; % wavelength shift (unit: nm) in free space;
theta_sig=34; % signal beam angle in air (unit: degree);
theta_ref=-42.5;% reference beam angle in air (unit: degree);
n_film=1.49;

sf = pi/180; % factor for transferring degree to radian

pi2 = 2*pi;

prop=pi2/lambda0;

prop_recon=pi2/(lambda0+d_lambda);

theta_sig=theta_sig*sf; % signal beam angle in air (unit: radian);
theta_ref=theta_ref*sf; % reference beam angle in air (unit: radian);

theta_sig_film=asin(sin(theta_sig)*1/n_film); % signal beam angle in film (unit: radian);
theta_ref_film=asin(sin(theta_ref)*1/n_film); % reference beam angle in film (unit: radian);

kv_sig=prop*n_film*[sin(theta_sig_film) 0 cos(theta_sig_film)]; % k-vector for signal beam in film;
kv_ref=prop*n_film*[sin(theta_ref_film) 0 cos(theta_ref_film)]; % k-vector for signal beam in film;

K=kv_sig-kv_ref; % grating K-vector

period=pi2/norm(K); % grating period

```

```

alpha=atan(K(1)/K(3));          % K-vector slant angle

%periodz = pi2/abs(K(3));      % period in z-direction

psi=(theta_sig_film+theta_ref_film)/2;    % grating angle

%periodx = abs(period/cos(psi));        % period in x-direction

d_theta=norm(K)*d_lambda/(4*pi*n_film*sin(alpha-theta_sig_film)); % d_theta (unit: radian) in the film;

d_theta_air=asin(sin(theta_sig_film+d_theta)*n_film/1)...
            -asin(sin(theta_sig_film)*n_film/1);      % d_theta (unit: radian) in the air;

%%%%%%%%%%%%%%
%%%%%%%%%%%%%%

%%%%% Reconstruction Part;

theta_recon=theta_sig+d_theta_air;    % reconstruction beam at right angle for wavelength shift in air (unit:
radian);

theta_recon_film=asin(sin(theta_recon)*1/n_film); % reconstruction beam angle in film (unit: radian);

kv_recon=prop_recon*n_film*[sin(theta_recon_film)  0  cos(theta_recon_film)]; % k-vector for
reconstruction beam in film;

kv_diff=kv_recon-K;                  % k-vector for diffraction beam in film;

phi=atan(kv_diff(1)/kv_diff(3));     % diffraction beam angle in film (unit: radian);

phi_air=asin(sin(phi)*n_film/1);     % diffraction beam angle in air (unit: radian);

phi_air=phi_air/sf                   % diffraction beam angle in air (unit: degree);

```

## APPENDIX C

Rigorous coupled wave analysis [50][51] in Matlab to simulate the performance of the multiplexed gratings using different wavelength for reconstruction.

```
function
[DEt1,DEt_1]=rcwa(d_film,delta_d,n_film,mod_n,film_aborp,theta1_con,theta2_con,lambda0_con,theta_
recon,theta_range,lambda0_recon)

%%%%%%%%%%%%%%%%%%%%%%%%%%%%%%%%%%%%%%%%%%%%%%%%%%%%%%%%%%%%%%%%%%%%%%%%
%%%%%%%%%%%%%%%%%%%%%%%%%%%%%%%%%%%%%%%%%%%%%%%%%%%%%%%%%%%%%%%%%%%%%%%%

% output parameter in function rcwa:                %

% DEt1 is the diffracted efficiency of the 1st order in rcwa;      %
% DEt_1 is the diffracted efficiency of the -1st order in rcwa;    %

%                                                    %

% input parameter in function rcwa:                %

% parameter 1 in function rcwa: thickness of film (microns);      %
% parameter 2 in function rcwa: sample angle in air (degrees);    %
% parameter 3 in function rcwa: reference angle in air (degrees);  %
% parameter 4 in function rcwa: constructed wavelength in air (microns);  %
% parameter 5 in function rcwa: reconstructed angle in air (degrees);  %
% parameter 6 in function rcwa: total angular range of analysis (degrees);  %
% parameter 7 in function rcwa: constructed wavelength in air (microns);  %

%%%%%%%%%%%%%%%%%%%%%%%%%%%%%%%%%%%%%%%%%%%%%%%%%%%%%%%%%%%%%%%%%%%%%%%%
%%%%%%%%%%%%%%%%%%%%%%%%%%%%%%%%%%%%%%%%%%%%%%%%%%%%%%%%%%%%%%%%%%%%%%%%

%%clear;

warning off;

t0=clock;          % set clock
```

```

%%lambda_0 = 0.488;      % wavelength in air (microns)

lambda_0 = lambda0_con;

%%d=1800;                % thickness of film (microns)

d=d_film;

n1 = 1.0;                % cover index

n2 = n_film;              % film index

n3 = 1.0;                % substrate index

%delta_n = 0.00034;      % peak index modulation

delta_n = mod_n;

%alpha =0.00034;        % absorption coeff. (microns^-1)

alpha=film_absorp;

%alpha=0.0000625;

%a = -0.0048;           % thicknesss chng. factor (fraction), - for shrinkage

a=delta_d;

apsi = 90;              % polarization angle (deg.) 90 for TE

delta = 0;              % rotation angle of construction plane (deg.)

points = 600;           % number of points to plot

ord = 2;                % number of orders

%theta1 = -4.80894;     % Bragg angle (degrees) in air

%theta2 = 4.80895;

theta1 = theta1_con;    % Bragg angle (degrees) in air

theta2 = theta2_con;    % theta1_con=sample beam; theta2_con=reference beam;

%ang_range = 0.05;

%ang_range = 1.0;       % total angular range of analysis (degrees)

ang_range =theta_range;

%ang_center = theta1;   % center of angular range (degrees)

```

```

ang_center = theta_recon; % changing the angle of sample beam;

% Calculate some universal parameters
%=====
sf = pi/180;
pi2 = 2*pi;
halfpi = pi/2;
prop=pi2/lambda_0;      % freespace propogation const.
prop1=prop*n1;          % prop. const. in region 1
prop2=prop*n2;          % prop. const. on region 2
prop3=prop*n3;          % prop. const. in region 3
theta1 = theta1*sf;     % convert to radians
theta2 = theta2*sf;     % convert to radians
delta=delta*sf;         % convert to radians
apsi = apsi*sf;         % convert to radians
ang_center = ang_center*sf; % convert to radians
ang_range = ang_range*sf; % convert to radians
erflag=0;                % flag for # of errors
inc = ang_range/points;  % increment for angle
lambda_f = lambda_0/n2;  % wavelength in film
d_=d+(a*d);              % thickness after shrinkage/swelling
ordt=(2*ord)+1;          % total # of orders including + and -
ofst=ord+1;              % offset so that all indices are pos.

% Convert theta1 and theta2 to angles inside film
%=====

```

```

theta1f = asin((n1/n2)*...
    sin(theta1));          % find theta1 inside film
theta2f = asin((n1/n2)*...
    sin(theta2));          % find theta2 inside film
if theta1>(pi/2),          % check whether theta1 is in 2nd quad.
    theta1f=pi-theta1f;
end
if theta2>(pi/2),          % check whether theta2 is in 2nd quad.
    theta2f=pi-theta2f;
end
if theta1<-(pi/2),          % check whether theta1 is in 3rd quad.
    theta1f=-pi-theta1f;
end
if theta2<-(pi/2),          % check whether theta2 is in 3rd quad.
    theta2f=-pi-theta2f;
end

% Calculate submatrix centers for matrices and
% vectors (to be used later).
%=====
for m=1:10,
    smc(m)=ofst+(m-1)*ordt;
end

% Determine index modulation to be used for all gratings
%=====

```

```

ep0 = n2^2-(i*alpha*n2*lambda_0/pi); % base permittivity of film

ep1 = 2*n2*delta_n; % permittivity modulation

q=ep1/ep0; % ratio of permittivity const's

% determine Fourier expansion terms of permittivity f'n
%-----

if ord==0,
    perm=[ep0];
else,
    perm=zeros(1,(4*ord)+1); % create vector for expansion of perm.
    perm(1,2*ord:(2*ord)+2)=[ep1/2 ep0 ep1/2]; % expansion coeff's for sinusoidal perm.
end

for h=-(2*ord):(2*ord), % expansion coeff's of inverse permittivity
    iperm(h+(2*ord)+1)=(1/(ep0*sqrt(1-q^2)))*((sqrt(1-q^2)-1)/q)^abs(h);
end

% determine effect of absorption as a f'n of angle
%=====

for m=1:points;
    % Convert loop index m to reconstruction angle theta in region 1
    %-----

    theta_r=ang_center-(ang_range/2)+(m*inc);

    % Convert theta_r to angle in film
    %-----

    theta_f=asin((n1/n2)*sin(theta_r));

```

```

% Subtract absorption from transmission

%-----

costheta=cos(theta_f);

if costheta==0,
    trans(m)=0;
else
    trans(m) = exp(-alpha*d_/costheta);
end

% Also, create vectors with angle points
%-----

x_r(m)=theta_r;

end

% grating parameters before shrinkage

%=====

kv1=prop2*[sin(theta1f) 0 cos(theta1f)];    % k-vector for beam 1
kv2=prop2*[sin(theta2f) 0 cos(theta2f)];    % k-vector for beam 2
K=kv1-kv2;                                % grating K-vector
period=pi2/norm(K);                        % grating period
phi=atan(K(1)/K(3));                        % K-vector slant angle
%periodz = pi2/abs(K(3));                  % period in z-direction
psi=(theta1f+theta2f)/2;                   % grating angle
periodx = abs(period/cos(psi));             % period in x-direction

% parameters after shrinkage

%=====

```

```

psi_ = atan((d/d_)*tan(psi));           % grating angle after shrinkage

period_ = abs(cos(psi_)*periodx);

K_ = (pi/period_)*[(abs(K(1))/K(1))*cos(psi_)...
    0 (abs(K(3))/K(3))*abs(sin(psi_))];

phi_ = atan(K_(1)/K_(3));

Kmag = norm(K_);                       % magnitude of new k-vector

Kz = K_(3);

%% sampled different lambda to calculate the corresponding efficiency
%% that means max_DEt1[] v.s. lambda[]
%% start -----
%% -----

%% max_DEt1=[]; lambda=[];

%% for delta_lambda=0.000:0.0005:0.300

    %% erflag=0;                       % flag for # of errors

    %% prop=pi/lambda_0;                % freespace propagation const.

    %% prop1=prop*n1;                   % prop. const. in region 1

    %% prop2=prop*n2;                   % prop. const. on region 2

    %% prop3=prop*n3;                   % prop. const. in region 3

    %% with different wavelength for reconstruction beam

    %% start-----
    %% -----

    %% delta_lambda=0.300;               %% wavelength difference between construction & recons. in air
(microns)

    new_lambda=lambda_0_recon;           %% new_lambda=lambda_0_recon

    prop=prop*lambda_0/new_lambda;       %% prop=prop*lambda_0/new_lambda

```

```

prop1= prop1*lambda_0/new_lambda;    %% prop1= prop1*lambda_0/new_lambda
prop3= prop3*lambda_0/new_lambda;    %% prop3= prop3*lambda_0/new_lambda
%% end-----

% calculate diffraction efficiency for each angle for grating zz
%=====
for m=1:points,
    theta_r=x_r(m);    % reconstruction angle

% polarization unit vector for reconstruction beam
%% theta_r is equivalent to alpha in M&G eq. 5
%-----
puv=[cos(apsi)*cos(theta_r)*cos(delta)-sin(apsi)*sin(delta) ...
     cos(apsi)*cos(theta_r)*sin(delta)+sin(apsi)*cos(delta) ...
     -cos(apsi)*sin(theta_r)];

% k-vectors for diffracted orders
% M&G, eq's 8-11
%-----
kx=zeros(1,ordt);    % x-components
kz1=zeros(1,ordt);    % z-components, reflected
kz3=zeros(1,ordt);    % z-components, transmitted

ky=prop1*sin(theta_r)*sin(delta);    % y-component (same for all) 2nd term in M&G eq. 4
term1=prop1*sin(theta_r)*cos(delta);    % 1st term in M&G eq. 9

```

```

term2=Kmag*sin(phi_);          % 2nd term in M&G eq. 9

for hm=-ord:ord,              %% hm is equivalent to i in M&G eq. 9
    kx(hm+ofst)=term1-(hm*term2);    %% M&G eq. 9
    kz1(hm+ofst)=sqrt(prop1^2-(kx(hm+ofst))^2-ky^2);
    kz3(hm+ofst)=sqrt(prop3^2-(kx(hm+ofst))^2-ky^2);
    if real(kz1(hm+ofst))>0,
        kz1(hm+ofst)=-kz1(hm+ofst);
    end
    if imag(kz3(hm+ofst))>0,
        kz3(hm+ofst)=-kz3(hm+ofst);
    end
end

% determine terms of S & U matrix
%-----
su=zeros(4*ordt);            % matrix for coupled wave eq's
for hm=-ord:ord,            % "hm" is short for harmonic
    su(hm+smc(1),hm+smc(1))=-i*hm*Kz;        % submatrix a (M&G eq. 20)
    su(hm+smc(1),hm+smc(4))=-i*prop;        % part of submatrix d
    su(hm+smc(2),hm+smc(2))=-i*hm*Kz;        % submatrix f
    su(hm+smc(2),hm+smc(3))=i*prop;        % part of submatrix g
    su(hm+smc(3),hm+smc(1))=i*kx(hm+ofst)*ky/prop;    % submatrix i
    su(hm+smc(3),hm+smc(2))=-i*(kx(hm+ofst))^2/prop;    % part of submatrix j
    su(hm+smc(3),hm+smc(3))=-i*hm*Kz;        % submatrix k
    su(hm+smc(4),hm+smc(1))=i*ky^2/prop;    % part of submatrix m

```

```

su(hm+smc(4),hm+smc(2))=-i*ky*kx(hm+ofst)/prop; % submatrix n
su(hm+smc(4),hm+smc(4))=-i*hm*Kz; % submatrix p
for p=-ord:ord, % for summation terms
    ofperm=hm-p+(2*ord)+1; % offset for permittivity
    su(hm+smc(1),p+smc(3))=-i*(kx(hm+ofst)/prop)*ky*iperm(ofperm); % submatrix c
    su(hm+smc(1),p+smc(4))=su(hm+smc(1),p+smc(4))+...
        i*(kx(hm+ofst)/prop)*iperm(ofperm)*kx(p+ofst); % rest of submatrix d
    su(hm+smc(2),p+smc(3))=su(hm+smc(2),p+smc(3))-...
        i*(ky^2/prop)*iperm(ofperm); % rest of submatrix g
    su(hm+smc(2),p+smc(4))=i*(ky/prop)*iperm(ofperm)*kx(p+ofst); % submatrix h
    su(hm+smc(3),p+smc(2))=su(hm+smc(3),p+smc(2))+...
        i*prop*perm(ofperm); % rest of submatrix j
    su(hm+smc(4),p+smc(1))=su(hm+smc(4),p+smc(1))-...
        i*prop*perm(ofperm); % rest of submatrix m
end

% This vector is for later (next loop)
% It contains exponential terms for BC's at z=d
expk(hm+ofst)=exp(i*hm*Kz*d_);
end

% Determine eigenvalues & eigenvectors
% vec contains eigenvectors
% lam contains eigenvalues along its diagonal
%-----
[vec,lam]=eig(su);

```

```

lam=diag(lam);

% Use eigenvectors and eigenvalues to calculator R's and T's
% We'll use a matrix solution. The terms will be in the order:
% C(m), m=eigenvalue#; Rx(i); Ry(i); Rz(i); Tx(i); Ty(i); Tz(i)
%=====

af=zeros(10*ordt);      % matrix of zeros
sp=zeros(10*ordt,1);    % column vector

% fill in sp, vector containing constant terms in matrix eq.
%-----

sp(smc(1))=puv(1);
sp(smc(2))=puv(2);
sp(smc(3))=ky*puv(3)-prop1*cos(theta_r)*puv(2);
sp(smc(4))=prop1*cos(theta_r)*puv(1)-kx(ord+1)*puv(3);

% fill in af, vector containing coeff. terms in matrix eq.
%-----

% Ri and Ti coeff. terms
for hm=-ord:ord,
    af(hm+smc(1),hm+smc(5))=1;          % from M&G eq 31
    af(hm+smc(2),hm+smc(6))=1;          % from M&G eq 32
    af(hm+smc(3),hm+smc(6))=-kz1(hm+ofst); % from M&G eq 33
    af(hm+smc(3),hm+smc(7))=ky;         % from M&G eq 33
    af(hm+smc(4),hm+smc(5))=kz1(hm+ofst); % from M&G eq 34
    af(hm+smc(4),hm+smc(7))=-kx(hm+ofst); % from M&G eq 34

```

```

af(hm+smc(5),hm+smc(8))=1;           % from M&G eq 35
af(hm+smc(6),hm+smc(9))=1;           % from M&G eq 36
af(hm+smc(7),hm+smc(9))=-kz3(hm+ofst); % from M&G eq 37
af(hm+smc(7),hm+smc(10))=ky;         % from M&G eq 37
af(hm+smc(8),hm+smc(8))=kz3(hm+ofst); % from M&G eq 38
af(hm+smc(8),hm+smc(10))=-kx(hm+ofst); % from M&G eq 38
af(hm+smc(9),hm+smc(5))=kx(hm+ofst); % from M&G eq 39
af(hm+smc(9),hm+smc(6))=ky;         % from M&G eq 39
af(hm+smc(9),hm+smc(7))=kz1(hm+ofst); % from M&G eq 39
af(hm+smc(10),hm+smc(8))=kx(hm+ofst); % from M&G eq 40
af(hm+smc(10),hm+smc(9))=ky;         % from M&G eq 40
af(hm+smc(10),hm+smc(10))=kz3(hm+ofst); % from M&G eq 40

end

% Cm coeff. terms (coefficients with eigenvector terms)
%=====
for mm=1:4*ordt,
    expod=exp(lam(mm)*d_);           % exponential terms in M&G eq's 27-30
    % Check for infinities, and if it's a problem set equal to
    % really big (for +Inf) or really small (for -Inf) number.
    if isinf(expod)==1,
        expod=(400*(sign(real(expod))+i*sign(imag(expod))));
    end
for hm=-ord:ord,
    af(hm+smc(1),mm)=-vec(hm+smc(1),mm);           % from M&G eq 31
    af(hm+smc(2),mm)=-vec(hm+smc(2),mm);           % from M&G eq. 32

```

```

af(hm+smc(3),mm)=-prop*vec(hm+smc(3),mm);          % from M&G eq. 33
af(hm+smc(4),mm)=-prop*vec(hm+smc(4),mm);          % from M&G eq. 34
af(hm+smc(5),mm)=-vec(hm+smc(1),mm)*expod*expk(hm+ofst); % from M&G eq. 35
af(hm+smc(6),mm)=-vec(hm+smc(2),mm)*expod*expk(hm+ofst); % from M&G eq. 36
af(hm+smc(7),mm)=-prop*vec(hm+smc(3),mm)*expod*expk(hm+ofst); % from M&G eq. 37
af(hm+smc(8),mm)=-prop*vec(hm+smc(4),mm)*expod*expk(hm+ofst); % from M&G eq. 38

end

end

% Solve system of eq's using left matrix divide
%-----
x1=af\sp;

% Calculate DE from R and T values
%-----
for hm=-ord:ord,

    R=[x1(hm+smc(5)) x1(hm+smc(6)) x1(hm+smc(7))];
    T=[x1(hm+smc(8)) x1(hm+smc(9)) x1(hm+smc(10))];

    DE_r(hm+ofst)=-real(kz1(hm+ofst)/(prop1*cos(theta_r)))*(norm(R))^2;
    DE_t(hm+ofst)=-real(kz3(hm+ofst)/(prop1*cos(theta_r)))*(norm(T))^2;

end

total=sum(DE_r)+sum(DE_t); % Sum of all light. Should = 1 for alpha=0
diff=total-DE_r(ofst)-DE_t(ofst); % Total of diffracted (nonzero) orders
if isnan(diff)==0, % Check for NaN's and inf's
    trans(m) = trans(m)*(1-diff); % Subtract diff. light transmitted
else

```

```

    erflag=erflag+1;

end

if ord>1,

    DEr_2(m)= DE_r(ofst-2);    % -2 refl. order
    DEr_1(m)= DE_r(ofst-1);    % -1 refl. order
    DEr0(m)= DE_r(ofst);       % 0 refl. order
    DEr1(m)= DE_r(ofst+1);     % 1 refl. order
    DEr2(m)= DE_r(ofst+2);     % 2 refl. order

    DEt_2(m)= DE_t(ofst-2);    % -2 trans. order
    DEt_1(m)= DE_t(ofst-1);    % -1 trans. order
    DEt0(m)= DE_t(ofst);       % 0 trans. order
    DEt1(m)= DE_t(ofst+1);     % 1 trans. order
    DEt2(m)= DE_t(ofst+2);     % 2 order DE

elseif ord==1,

    DEr_1(m)= DE_r(ofst-1);    % -1 refl. order
    DEr0(m)= DE_r(ofst);       % 0 refl. order
    DEr1(m)= DE_r(ofst+1);     % 1 refl. order

    DEt_1(m)= DE_t(ofst-1);    % -1 trans. order
    DEt0(m)= DE_t(ofst);       % 0 trans. order
    DEt1(m)= DE_t(ofst+1);     % 1 trans. order

elseif ord==0,

    DEr0(m)= DE_r(ofst);       % 0 refl. order
    DEt0(m)= DE_t(ofst);       % 0 trans. order

```

```
end  
  
end  
  
DEt1=DEt1(points/2);%max(DEt1);%DEt1(points/2);  
DEt_1=DEt_1(points/2);%max(DEt_1);%DEt_1(points/2);  
  
%save yuan_all_data.mat;
```

**REFERENCES**

- [1]. D. Huang, E. A. Swanson, C. P. Lin, J. S. Schuman, W. G. Stinson, W. Chang, M. R. Hee, T. Flotte, K. Gregory, C. A. Puliafito, and J. G. Fujimoto, "Optical coherence tomography," *Science* 254, pp.1178-1181, 1991.
- [2]. S. Bourquin, P. Seitz, and R. P. Salathe, "Optical coherence topography based on a two-dimensional smart detector array," *Opt. Lett.* 26, 512–514, 2001.
- [3]. T. Xie, D. Mukai, S. Guo, M. Brenner, and Z. Chen, "Fiberoptic- bundle-based optical coherence tomography," *Opt. Lett.* 30, 1803–1805, 2005.
- [4]. Y. Chen, H. Chen, D. Dilworth, E. N. Leith, J. Lopez, M. Shih, P. C. Sun, and G. Vossler, "Evaluation of holographic methods for imaging through biological tissue," *Appl. Opt.* 32, pp. 4330-4336, 1993.
- [5]. E. N. Leith, C. Chen, H. Chen, Y. Chen, D. Dilworth, J. Lopez, J. Rudd, Sun P-C. Sun, J. Valdmanis, and G. Vossler, "Imaging through scattering media with holography," *J. Opt. Am. A* 9, pp. 1148-1153, 1992.
- [6]. T-C. Poon, K. Doh, B. Schilling, M. Wu, K. Shinoda, and Y. Suzuki, "Three-dimensional microscopy by optical scanning holography," *Opt. Eng.* 34, pp. 1338-1344, 1995.
- [7]. G. Indebetouw, and Klysubun, "Space-time digital holography: A three-dimensional microscopic imaging scheme with an arbitrary degree of spatial coherence," *App. Phys. Lett.* 75, pp. 2017-2019, 1999.
- [8]. M. K. Kim, "Tomographic three-dimensional imaging of a biological specimen using wavelength-scanning digital interference holography," *Opt. Express* 7, pp. 305-310,

2000.

- [9]. E. N. Leith, W.-C. Chien, K. D. Mills, B. D. Athey, and D. S. Dilworth, "Optical sectioning by volume holographic coherence imaging: a generalized analysis," *J. Opt. Soc. Am. A* 20, pp. 380-387, 2003.
- [10]. M. P. Shih, H. S. Chen, and E. N. Leith, "Spectral holography for coherence-gated imaging," *Opt. Lett.* 24, 52-54, 1999.
- [11]. W. Liu, D. Psaltis, and G. Barbastathis, "Real-time spectral imaging in three spatial dimensions," *Opt. Lett.* 27, pp. 854-856, 2002.
- [12]. T. J. Pfefer, K. T. Schomacker, M. N. Ediger, and N. S. Nishioka, "Multiple fiber probe design for fluorescence spectroscopy in tissue," *Appl. Opt.* 41, 4712-4721, 2002.
- [13]. H. N. Paulsen, K. M. Hilligse, J. Thgersen, S. R. Keiding, and J. J. Larsen, "Coherent anti-Stokes Raman scattering microscopy with a photonic crystal fiber based light source," *Opt. Lett.* 28, 1123-1125, 2003.
- [14]. W. Gobel, J. N. D. Kerr, A. Nimmerjahn, and F. Helmchen, "Miniaturized two-photon microscope based on a flexible coherent bundle and a gradient-index lens objective," *Opt. Lett.* 29, 2521-2523, 2004.
- [15]. M. Larsson, W. Steenbergen, and T. Stromberg, "Influence of optical properties and fiber separation on laser Doppler flowmetry," *J. Biomed. Opt.* 7, 236-243, 2002.
- [16]. J. M. Schmitt, "Optical coherence tomography (OCT): a review," *IEEE J. Sel. Top. Quantum Electron.* 5, 1205-1215, 1999.
- [17]. A. F. Fercher, W. Drexler, C. K. Hitzenberger, and T. Lasser, "Optical coherence

- tomography—principles and applications,” *Rep. Prog. Phys.* 66, 239–303, 2003.
- [18]. X. Liu, M. J. Cobb, Y. Chen, M. B. Kinney, and X. Li, “Rapid-scanning forward-imaging miniature endoscope for real-time optical coherence tomography,” *Opt. Lett.* 29, 1763–1765, 2004.
- [19]. P. R. Bargo, S. A. Pahl, and S. L. Jacques, “Collection efficiency of a single optical fiber in turbid media,” *Appl. Opt.* 42, 3187–3197, 2003.
- [20]. T. Papaioannou, N. W. Preyer, Q. Fang, A. Brightwell, M. Carnohan, G. Cottone, R. Ross, L. R. Jones, and L. Marcu, “Effects of fiber-optic probe design and probe-to-target distance on diffuse reflectance measurements of turbid media: an experimental and computational study at 337nm” *Appl. Opt.* 43, 2846–2860, 2004.
- [21]. T. Xie, H. Xie, G. K. Fedder, and Y. Pan, “Endoscopic optical coherence tomography with new MEMS mirror,” *Electron. Lett.* 39, 1535–1536, 2003.
- [22]. T. Xie, D. Mukai, S. Guo, M. Brenner, and Z. Chen, “Fiber-optic-bundle-based optical coherence tomography,” *Opt. Lett.* 30, 1803–1805, 2005.
- [23]. H. Rao, R. Scarmozzino, and R. M. Osgood, Jr., “A bidirectional beam propagation method for multiple dielectric interfaces,” *Photon. Technol. Lett.* 11, 830–832, 1999.
- [24]. W. P. Huang, C. L. Xu, S. T. Chu, and S. K. Chaudhuri, “The finite difference vector beam propagation method: analysis and assessment,” *J. Lightwave Technol.* 10, 295–305, 1992.
- [25]. C. L. Xu, W. P. Huang, J. Chrostowski, and S. K. Chaudhuri, “A full vectorial beam propagation method for anisotropic waveguides,” *J. Lightwave Technol.* 12, 1926–1931, 1994.

- [26].RSOFT Design Group, BeamPROP V. 6.01, [www.rsoftdesign.com](http://www.rsoftdesign.com).
- [27].L. Wang, S. L. Jacques, and L. Zheng, "MCML—Monte Carlo modeling of light transport in multi-layered tissue," *Comput. Methods Programs Biomed.* 47, 131–146, 1995.
- [28].H. J. van Staveren, C. J. M. Moes, J. van Marle, S. A. Prahl, and M. J. C. van Gemert, "Light scattering in Intralipid-10% in the wavelength range of 400–1100 nm," *Appl. Opt.* 30, 4507–4514, 1991.
- [29].H. Ding, J. Q. Lu, K. M. Jacobs, and X.-H. Hu, "Determination of refractive indices of porcine skin tissues and Intralipid at eight wavelengths between 325 and 1557 nm," *J. Opt. Soc. Am. A*, 22, 1–7, 2005.
- [30].L. Wang and S. L. Jacques, *Monte Carlo Modeling of Light Transport in Multi-layered Tissues in Standard C* (University of Texas, M.D. Anderson Cancer Center, 1992).
- [31].Corning SMF-28 Optical Fiber product information (Corning, Inc., N.Y., 2001).
- [32].Stocker Yale BIF-RC-1310-L2 product information, Stocker Yale, Inc., New Hampshire, 2005, <http://www.stockeryale.com/o/fiber/products/bif-rc-1310-12.htm>.
- [33].M. Scepanovic, J. Castillo, "Design and processing of high-density single-mode fiber arrays for imaging and parallel interferometer applications", *Appl. Opt.*, vol. 43, No. 21, 2004.
- [34].L. J. Arauz Crespo, "Fabrication and assembly of fiber array for an endoscopic parallel optical coherence tomography system," The University of Arizona, Electrical and Computing Engineering Department, Thesis, 2007.

- [35]. Y. Luo , L. J. Arauz, J. E. Castillo, J. K. Barton, and R. K. Kostuk, "Parallel optical coherence tomography system," *Applied Optics*, vol. 46, pp. 8291-8297, Dec. 2007.
- [36]. T. L. Troy and S. N. Thennadil, "Optical properties of human skin in the near infrared wavelength range of 1000 to 2200 nm," *J. Biomed. Opt.* 6, pp. 167–176, 2001.
- [37]. Y. Luo , J. E. Castillo, L. J. Arauz, J. K. Barton, and R. K. Kostuk, " Coupling and crosstalk effects in 12-15um diameter single-mode fiber arrays for simultaneous transmission and photon collection from scattering media," *Applied Optics*, vol. 46, pp. 253-261, Jan. 2007.
- [38]. A. R. Tumlinson, J. K. Barton, B. Povazay, H. Sattman, A. Unterhuber, R. A. Leitgeb, and W. Drexler, "Endoscope-tip interferometer for ultrahigh resolution frequency domain optical coherence tomography in mouse colon," *Opt. Express* 14, 1878–1887, 2006.
- [39]. H. Kogelnik, "Coupled wave theory for thick hologram grating," *Bell Syst. Tech. J.* Vol. 48, pp. 2909–2946, 1969.
- [40]. H. Coufal, L. Hesselink, and D. Psaltis, "Holographic data storage," Springer-Verlag, 2002.
- [41]. J. D. Pawley, "Handbook of biological confocal microscope," 3<sup>rd</sup> Edition, Springer-Verlag, 2006.
- [42]. A. Sinha, and G. Barbastathis, "Broadband volume holographic imaging," *Appl. Opt.* 43, pp. 5214-5221, 2004.
- [43]. A. Sinha, W. Sun, T. Shih, and G. Barbastathis, "Volume holographic imaging in

- transmission geometry,” *Appl. Opt.* 43, pp. 1533-1551, 2004.
- [44].P. J. Gelsinger-Austin, “Optical Design for a Spatial-Spectral Volume Holographic Imaging System,” The University of Arizona, College of Optical Sciences, Thesis, 2008.
- [45].B. C. Wilson and S. L. Jacques, "Optical reflectance and transmittance of tissues: Principles and applications." *IEEE J. Quantum Electron.* 26, pp. 2186-2199, 1990.
- [46].L. Wang and S. L. Jacques, *Monte Carlo Modeling of Light Transport in Multi-layered Tissues in Standard C* (University of Texas, M.D. Anderson Cancer Center, 1992).
- [47].S. H. Lin, K Y. Hsu, W. Chen, and W. T. Whang, “Phenanthrenequinone-doped poly(methyl methacrylate) photopolymer bulk for volume holographic data storage”, *Opt. Lett.* 25, pp. 451-453, 2000.
- [48].G. Barbastathis and D. J. Brady, “Multidimensional tomographic imaging using volume holography,” *Proc. of the IEEE* 87, 2098-2120, 1999.
- [49].Y. Luo, P. J. Gelsinger, G. Barbastathis, J. K. Barton, & R. K. Kostuk, “Optimization of multiplexed holographic gratings in PQ-PMMA for spectral-spatial filters”, *Opt. Lett.* 33, pp566-568, 2008.
- [50].G. Moharam and T. K. Gaylord, “Three-dimensional vector coupled-wave analysis of planar-grating diffraction,” *J. Opt. Soc. Am.* 73, 1105–1112, 1983.
- [51].J. A. Frantz, R. K. Kostuk and D. A. Waldman, “Model of noise-grating selectivity in volume holographic recording materials by use of Monte Carol simulations,” *J. Opt. Soc. Am. A* 21, pp. 378-387, 2004.

- [52].R. R. A. Syms and L. Solymar, "Localized one-dimensional theory for volume holograms," *Optical and Quantum Electronics* 13, 415–419, 1981.
- [53].W. K. Maeda, "Edge-Illuminated Gratings in PQ-doped PMMA for OCDMA Applications," The University of Arizona, Electrical and Computing Engineering Department, Thesis, 2005.
- [54].A. V. Veniaminov, V. G. Goncharov, and A. P. Popov, "Hologram amplification by diffusion destruction of out-ofphase periodic structures," *Opt. and Spectros.* 70(4), 505-508, 1991.
- [55].A. P. Popov, I. Novikov, K. Lapushka, Y. Ponosov, Y. Ashcheulov, and A. V. Veniaminov, "Spectrally selective holographic optical elements based on a thick polymer medium with diffusional amplification," *J. of Opt. A: Pure and Appl. Opt.* 2(5), 494-499, 2000.
- [56].G. J. Steckman, I. Solomatine, G. Zhou, and Psaltis, "Characterization of phenanthrenequinone-doped poly(methyl methacrylate) for holographic memory," *Opt. Lett.* 23(16), 1310-1312, 1998.
- [57].R. K. Kostuk, W Maeda, C-H Chen, I. Djordjevic, and B. Vasic, "Cascaded Holographic Polymer Reflection Grating Filters for Optical-code-division-multiple-access Applications," *Appl. Opt.* Vol. 44, pp. 7581-7586, 2005.
- [58].A. Sato, and R. K. Kostuk, "Holographic Edge-Illuminated Polymer Bragg Gratings for Dense Wavelength Division Optical Filters at 1550 nm," *Appl. Opt.* Vol. 42, pp. 778-784, 2003.
- [59].J. M. Russo Miranda, "Temperature dependence of holographic filters in

- Phenanthrenequinone-doped poly (methyl methacrylate),” The University of Arizona, Electrical and Computing Engineering Department, Thesis, 2007.
- [60]. J. V. Kelly, M. R. Glesson, C. E. Close, F. T. O. Neil, and J. T. Sheridan, “Temporal analysis of grating formation in photopolymer using the nonlocal polymerization-driven diffusion model”, *Opt. Express* 13, pp. 6990-7004, 2005.
- [61]. A. V. Galstyan, R. S. Hakobyan, S. Harbour, and T. Galstian, “Study of the inhibition period to the holographic grating formation liquid crystal photopolymerization materials,” *Electronic-Liquid Crystal Communications*, 2004. ([http://www.e-lc.org/docs/2004\\_05\\_05\\_11\\_13\\_17](http://www.e-lc.org/docs/2004_05_05_11_13_17))
- [62]. M. R. Glesson, J. V. Kelly, C. E. Close, F. T. O. Neil, and J. T. Sheridan, “The impact of inhibition processes during grating formation in photopolymer materials”, *Proc. SPIE* 5827, pp. 232-243, 2005.
- [63]. W. Xu, D. L. Mathine, and J. K. Barton, “Analog CMOS design for optical coherence tomography signal detection and processing,” *IEEE Trans. Biomed. Eng.* 55, pp. 485-489. 2008.
- [64]. J. A. Frantz, J. T. A. Carriere, and R. K. Kostuk, “Measurement of ion-exchanged waveguide burial depth with a camera,” *Opt. Eng.* 43, 3149–3154, 2004.
- [65]. J. T. A. Carriere, J. A. Frantz, B. R. West, S. Honkanen, and R. K. Kostuk, “Bend loss effects in diffused, buried waveguides,” *Appl. Opt.* 44, 1698–1703, 2005.